Modeling and simulation
of carbon nanotube growth

by

Brittan Alan Farmer

A dissertation submitted in partial fulfillment
of the requirements for the degree of
Doctor of Philosophy
(Applied and Interdisciplinary Mathematics)
in The University of Michigan
2015

Doctoral Committee:

Professor Selim Esedoḡlu, Co-Chair
Associate Professor A. John Hart, Massachusetts Institute of Technology,
Co-Chair
Associate Professor Silas D. Alben
Professor Robert Krasny
Professor Peter S. Smereka

To my wife, Susanna

ACKNOWLEDGEMENTS

Praise God, from whom all blessing flow.

TABLE OF CONTENTS

LIST OF FIGURES

LIST OF TABLES

ABSTRACT

Modeling and simulation of carbon nanotube growth

by

Brittan Alan Farmer

Co-Chair: Professor Selim Esedoḡlu

Co-Chair: Associate Professor A. John Hart

Carbon nanotubes (CNTs) have exceptional mechanical, electronic, and thermal properties, which make them ideal for a variety of applications. Forests of CNTs have additional applications beyond individual CNTs, such as thermal interface layers and filtration membranes. In this dissertation, we present mathematical models that allow for greater understanding and control of the CNT synthesis process.

We first describe an atomistic model of CNT growth, which focuses on carbon-carbon interactions and approximates the interaction of carbon atoms with the substrate and catalyst. We also describe a simplified one-dimensional atomistic model that preserves some features of the full model of CNT growth. This simple model has one global energy minimum and many competing local minima. We simulate this system and compare the non-equilibrium probability distributions with the equilibrium distribution. We calculate transition rates between the basins of different local minima, and use these in a master equation to calculate non-equilibrium distributions. To allow for further analysis, we approximate the rate matrix by a matrix with two parameters – a slow rate and a fast rate. We present the equilibrium distribu-

tion, hitting times, and eigenvalues of this matrix and describe how they depend on the rate parameters and the number of atoms in the chain. Finally, we describe the insights this simplified model provides regarding CNT growth.

We also present a mathematical model for collective chemical effects in arrays of CNT pillars, which lead to non-uniformities in pillar height. This model involves coupling a kinetic model of CNT growth with a diffusion equation for the transport of a gaseous active species. We assume this species is produced during decomposition of the feedstock gas on the catalyst and enhances the CNT growth rate by lowering the activation energy of feedstock decomposition. We simulate the effect of catalyst spacing on pillar heights and compare with experiments. We introduce a threshold on active species concentration for pillar liftoff, with which the model is able to reproduce the absence of pillars seen in widely spaced arrays in experiments. We also present strategies for creating patterns that yield more uniform pillars.

CHAPTER I

Introduction and background

In this dissertation, we develop models for the synthesis (or growth) of individual carbon nanotubes (CNTs) and arrays of carbon nanotube pillars. We use two different approaches to study these phenomena. The growth of individual carbon nanotubes is described by atomistic modeling. Such models can be used as a framework to study various aspects of growth, including dependence of the growth rate on mechanical forces. We describe two atomistic models: one for CNT growth by catalytic chemical vapor deposition and one for a simple system which preserves some features of CNT growth but is more conducive to analysis. To model the synthesis of CNT pillar arrays, we use a kinetic model of CNT growth coupled to a gas transport model. In particular, this model is able to describe the spatial variations of CNT pillar height observed in experiments by including the effect of a spatially varying chemical environment across the array.

The main contribution of this dissertation regarding individual CNT growth is to provide a simplified model which is analogous to CNT growth, yet is amenable to analysis. In particular, *all* minima, saddle points, probabilities, and transition rates can be identified. The time-dependent probability of different configurations can be studied via a master equation, and the dependence on temperature, addition rate, and chain length can be determined.

The main contribution regarding CNT pillar growth is to define a mathematical model that describes spatially varying pillar height via a spatially varying concentration of active species. This model is capable of describing the dependence of uniformity on the spacing of the catalyst patches. With a threshold chemical concentration for pillar lift-off, it is also in agreement with the absence of pillar growth at the edge of the arrays. This shows that production and transport of active species is a reasonable hypothesis for the source of non-uniformities in pillar heights. The model can also be used as a predictive tool. For instance, it can be used to design catalyst patterns that produce pillar arrays with more uniform heights.

1.1 Outline

The outline of this dissertation is as follows. In Chapter I, we summarize the dissertation, give some background on carbon nanotubes, and describe the literature on the simulation and analysis of atomistic and kinetic models of CNT growth.

In Chapter II, we describe a model of CNT growth based on empirical potentials. This is similar to other models in the literature, except that it models the catalyst as a continuum rather than as individual atoms, similar to the approach in the article by Schebarchov et al. [72]. We discuss the difficulties in simulating and analyzing this model. Then, we describe a simple one-dimensional model, which maintains some features of the three-dimensional model but allows for a deeper analysis. Molecular dynamics (MD) simulations of this model are presented, both for a fixed number of atoms and for a non-equilibrium system in which atoms are added at the left end of the chain. Transition rates are calculated and used with a master equation approach to determine the non-equilibrium probability distribution of the system. We then perform an analysis of the master equation, both for the rate matrix calculated directly from the energy landscape, and for a two-parameter approximation of this matrix. In particular, the equilibrium distribution, hitting times, and eigenvalues and

eigenvectors are calculated, and the initial value problem is solved for several initial conditions. The growth efficiency is defined, and its dependence on temperature, addition rate, and chain length is described.

In Chapter III, the growth of arrays of CNT pillars and the observed non-uniformities in height are described. This research was done in collaboration with Mostafa Bedewy. A mathematical model of chemical coupling is given. Simulations of this model are performed and compared to experimental results. The spatially varying active species concentration, the resulting spatially varying CNT growth kinetics, and inclusion of a threshold for pillar liftoff are all discussed. The model is also used to create catalyst patterns that should give more uniform pillar growth.

In Chapter IV, we present the conclusions of the dissertation and outline future research.

1.2   Review of carbon nanotube structure and synthesis

Carbon nanotubes are carbon molecules with the structure of a honeycomb lattice rolled into a cylinder, typically with hemispherical caps at each end [30]. See Figure 1.1. The angle between the zigzag line in this lattice and the circumference of the nanotube is called the chiral angle. Non-hexagonal rings in the lattice, such as pentagons or heptagons, represent defects. If the structure consists of a single cylinder, it is called a single-walled nanotube (SWNT); if it consists of several coaxial cylinders, it is called a multi-walled nanotube (MWNT). Nanotubes can also be synthesized in close proximity so that the van der Waals force causes them to align and grow upward into a "forest" of CNTs. Related to carbon nanotubes is graphene, which is a single flat sheet of carbon atoms, arranged in a honeycomb lattice.

Carbon nanotubes can be synthesized by high temperature methods ($\geq 3000°$C), such as arc discharge or laser ablation, as well as medium temperature methods ($\leq 1000°$C), such as chemical vapor deposition (CVD) [30]. All three methods pro-
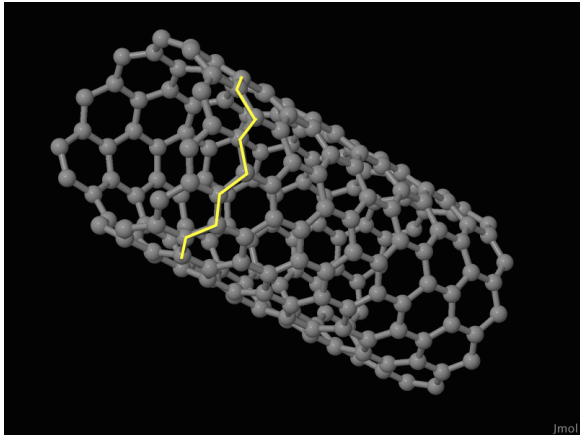
Figure 1.1: Ball and stick model of a single-walled carbon nanotube, with the zigzag line highlighted in yellow.

duce similar structures, so they probably involve similar atomic growth mechanisms. In arc discharge, carbon atoms are evaporated by a plasma of helium gas formed by a high current passing between carbon anodes and cathodes. This technique produces MWNTs, but if metal catalyst is present in the carbon anode, it can produce SWNTs. In laser ablation, an intense laser pulse is used to ablate, i.e. evaporate, a carbon target containing small amounts of Ni and Co. The carbon target is in a tube furnace, and an inert gas is used to collect the nanotubes. Both of these methods involve evaporation of carbon, which requires temperatures in excess of $3000°C$.

CVD methods do not require such high temperatures, and are therefore more scaleable and hold the greatest promise for mass production of CNTs. In CVD, hydro-carbon feedstock gases flow through a furnace containing metal catalyst nanoparticles, which may be supported on a substrate or floating in the gas. Typical feedstock gases are ethylene or acetylene (or methane for SWNTs), the catalyst is usually transition-metal (Fe, Ni, Co) nanoparticles on alumina support, and growth temperatures vary between $550°C$ and $750°C$ ($850°C$–$1000°C$ for SWNTs). The gas decomposes and dissolves on the catalyst particles. These dissolved carbon atoms bond together, eventually forming a graphenic network on the catalyst surface. This structure lifts

off from the catalyst to form a cap, but remains bonded to the catalyst along the edge. If a substrate is present, the nanotube may alternatively undergo tip growth. In this growth mode, no cap is formed. The catalyst detaches from the substrate and remains at the tip of the growing nanotube. In either case, carbon atoms continue to incorporate into the structure at the catalyst-nanotube interface, and the nanotube grows longer. This technique involves many process parameters: feedstock composition, catalyst composition, choice of substrate, the presence of impurities such as water, pressure, and temperature. The resulting CNTs can be characterized by their diameter, chiral angle, length, and quality (high quality nanotubes have low defect concentrations). A major goal of current research is to design growth conditions that produce CNTs with specific chiralities.

In addition to individual CNTs, it is also possible to manufacture vertically-aligned arrays (or "forests") of CNTs. A film of catalyst material is deposited onto a growth substrate. It is annealed to create many individual catalyst nanoparticles. When these nanoparticles are exposed to the feedstock gas in the furnace tube, CNTs nucleate and grow from many of the catalyst nanoparticles. If the density of the CNTs is high enough, the van der Waals forces between different nanotubes cause them to align and grow upward into a forest of CNTs [14]. The CNTs within the forest will come in contact with other nanotubes at several points, but there is separation between the CNTs along most of their length. If the catalyst film is deposited in a pattern, such as a grid of squares, an array of CNT forest pillars will grow. These CNT pillars have desirable mechanical and thermal properties for use in thermal interfaces or dry adhesives.

1.3   Review of early models of CNT growth

Two early hypotheses about the CNT growth mechanism were the "scooter" model and the vapor-liquid-solid (VLS) model [30, 44]. In the scooter model [78, 47], a

single metal catalyst atom attaches to the open end of the carbon nanotube and prevents pentagonal defects from forming as carbon atoms incorporate to the edge. This is more relevant to arc discharge and laser ablation methods, since the catalyst in CVD is a metal nanoparticle consisting of tens or hundreds of atoms. In this case, the VLS model is more relevant. In this model, originally devised for silicon whiskers [83] and carbon fibers [79, 9], the carbon-containing vapor decomposes on the catalyst particles, the carbon dissolves into the super-saturated liquid catalyst, and then precipitates into the solid carbon nanotube. This model is still thought to be generally correct, although much work has been done to understand the atomic mechanisms. The growth conditions may also be such that the catalyst particle is solid, so that a vapor-solid-solid model should be considered.

1.4   Review of CNT growth simulations via atomistic modeling

Many atomistic models of CNT growth exist in the literature, using different descriptions of interatomic interactions via empirical, semi-empirical, and first principles formulations. Moving from empirical to semi-empirical to first principles methods, the accuracy increases, but so do the computational demands. As such, first principles simulations are limited to small systems of atoms over short time scales, whereas semi-empirical and empirical methods are able to simulate larger systems over longer periods of time. The dynamics of such models can be studied by MD, Monte Carlo (MC) methods, or hybrids of these two. For reviews of atomistic models of CNT growth, see [42, 31]. In the following, we summarize the work of several influential research groups utilizing different approaches to model the interatomic interactions. We begin with empirical methods, then describe semi-empirical methods, and finally we treat first principles methods. Although first principles methods use more accurate

interatomic interactions, the limitations imposed by their computational demands require addition rates much faster than for empirical methods, which are already unrealistically short compared to those in experiments. Therefore, the results of first principles simulations are not necessarily more realistic than those of empirical simulations.

1.4.1 Empirical potentials

1.4.1.1 Shibuta and Maruyama

Carbon nanotube growth. In [73], Shibuta and Maruyama study carbon nanotube growth using classical molecular dynamics. Their simulation setup corresponds to the catalytic chemical vapor deposition technique. They consider different sized catalyst clusters – Ni_{32}, Ni_{108}, and Ni_{256}, with diameters 0.8, 1.3, and 1.6 nm, respectively – in a periodic box with 500 carbon source atoms. They model carbon-carbon interactions with a simplified Brenner potential [20, 87], and the carbon-metal and metal-metal interaction with a potential used in earlier work by one of the authors [88]. Carbon-source molecules repel each other with a Lennard-Jones potential until they come in contact with the metal catalyst and transform into carbon atoms. The growth temperature is 2500 K. For the Ni_{108} cluster, they observe the following growth mechanisms:

1. Carbon atoms attached to the cluster absorb into the cluster.

2. After about 2 ns, the cluster saturates with carbon, and hexagonal carbon networks form inside the cluster.

3. After about 4 ns, the carbon networks separate from the surface of the particle and some cap structures appear.

4. Carbon incorporation continues, and a graphitic protrusion forms.

7

5. The carbon shell surrounding the catalyst eventually lifts off the surface to form a cap structure with a stem.

They observe that if the density of carbon-source molecules is too high, the catalyst surface becomes coated with carbon atoms. They also note that for the smaller catalyst cluster (Ni_{32}), the catalyst surface is covered with a graphitic structure, and growth terminates due to lack of carbon supply. For the larger catalyst cluster (Ni_{256}), the cap structure conforms to the metal humps on the catalyst surface rather than the entire metal-carbon cluster. Their simulations suggest a strong interaction between the hexagonal carbon network and the structure of the catalyst, wherein the carbon atoms occupy the hollow sites of the catalyst lattice. Their simulations also demonstrate the formation of hexagonal networks of carbon atoms *inside* the catalyst cluster, which is not seen in the work of other groups.

The melting point of nickel and nickel-carbide clusters and the effect of substrate-catalyst interaction. In [74], Shibuta and Maruyama incorporate the effect of the substrate into their molecular dynamics simulations. Carbon-carbon, carbon-metal, and metal-metal interactions are described with the same potentials as in [73]. Metal-substrate interactions are described with a one-dimensional averaged Lennard-Jones potential. The authors study the melting point of nickel clusters and nickel-carbide clusters with substrate-metal interaction strengths ranging from 0.5 eV to 1.25 eV. The nickel clusters demonstrate a transition from crystal structure to disorder as the temperature increases past the melting point. For example, the melting point of the Ni_{256} cluster with a binding energy of 0.25 eV is calculated to be 2571 K.[1] Below the melting temperature (at 2000 K), the clusters maintain their crystal structure and have a faceted structure. Increasing the catalyst-substrate interaction causes the structure to form layers. At 3000 K, the nickel clusters have

---

[1]This demonstrates that their potential is not quantitatively accurate, as the melting point of nickel in bulk is 1726 K. Nickel nanoparticles will have an even lower melting point because of the high surface-area-to-volume ratio, but the adhesion to the substrate could mitigate this effect. The qualitative predictions of the model, however, are still valid.

changed to liquid droplets, and the clusters wet to the substrate more strongly with increasing catalyst-substrate interaction. The nickel-carbide clusters, on the other hand, show no transition from order to disorder and do not have a crystal structure at 2000 K. At 3000 K, the nickel-carbide clusters wet to the substrate more strongly with increasing catalyst-substrate interaction.

CNT nucleation was studied for substrate-metal binding energies of 0.25 eV, 0.5 eV, and 1.0 eV, with the growth temperature set to 2500 K. When the binding energy is large, the catalyst cluster has a layered structure, and graphene forms parallel to this layer. There is a geometrical match between the Ni atoms and the graphene. The number of hexagonal rings in the carbon structure grows quickly; however, this arrangement makes it difficult for the graphitic islands to lift off from the catalyst. For a weaker catalyst-substrate binding, graphene separates from the cluster in a direction independent of the direction of the substrate.

1.4.1.2 Ding, Bolton, and Rosén

MD simulations of CNT growth including temperature dependence. In [27], Ding, Bolton, and Rosén perform molecular dynamics simulations to study the nucleation and growth of single-walled carbon nanotubes. The carbon atoms are divided into dissolved and precipitated carbon atoms based on the number of neighboring Fe atoms. The interaction of dissolved carbon atoms with other dissolved carbon atoms and with precipitated carbon atoms is given by Lennard-Jones potentials, while their interaction with iron atoms is given by a Johnson potential. Precipitated carbon atoms interact with other precipitated carbon atoms via a Brenner potential and with iron atoms via a Johnson potential with a well depth that depends on the carbon bond saturation. Metal atoms interact with other metal atoms via a Born-Mayer potential. Carbon atoms are inserted at the center of a catalyst particle at fixed time intervals. Growth proceeds in the following steps: C dissolves into the cat-

alyst particle; after supersaturation, C precipitates on the surface, eventually forming polygons and graphitic islands; as carbon continues to incorporate, a graphene sheet, SWNT, or soot-like structure is grown, depending on temperature. If growth occurs between 800 K and 1400 K, the authors observe that a graphitic island containing about 5 to 7 polygons lifts off from the catalyst surface, forming a cap. The cap diameter increases until it is the same as the catalyst diameter. At 600 K, a graphene layer encapsulates the catalyst cluster, and at 1600 K, a soot-like structure encapsulates the cluster. Encapsulation can also occur at growth temperatures of 800 K if the carbon addition rate is increased, say from 1 atom per 40 ps to 1 atom per 2 ps. The authors observe that all SWNTs contain defects; in general, new C atoms do not append to the SWNT to form hexagons. However, they find that slower C atom addition yields fewer defects. Although the rate of carbon addition is orders of magnitude faster than in experiments, this is necessary to achieve CNT growth in a reasonable simulation time.

Effect of nanotube-catalyst interaction strength. In [29], Ding et al. consider different SWNT fragments attached to catalyst clusters composed of Fe, Co, Ni, Cu, Pd, or Au. Using static density functional theory (DFT) calculations, the authors find that the SWNT-catalyst adhesion energies span from about 1 to 3 eV/bond. The commonly used catalysts (Fe, Ni, and Co) interact more strongly with the SWNT open end than the less efficient catalysts (Pd, Cu, and Au). The authors conclude that adhesion between SWNTs and catalyst particles needs to be strong to support nanotube growth. They also consider the enthalpies for the SWNT to detach from the catalyst and close into a cap at the growing end. Fe, Co, Ni have large positive reaction enthalpies, which means cap formation is very unlikely. The enthalpies for Au and Cu are negative, so cap formation is almost certain. The enthalpy for Pd is weakly positive, making cap formation unlikely, but possible. Finally, they perform MD simulations of CNT nucleation and growth using the same model as in their

previous work [27], except that here the nanotube-metal interaction strength is varied. If the carbon-metal bond strength is 2.5-3.0 eV, adding one carbon atom to a SWNT cap will cause the SWNT to grow longer, maintaining the same diameter. If the carbon-metal bond strength is decreased to 1.5-2.0 eV, adding carbon atoms to a SWNT atoms to the cap causes the diameter of the SWNT to decrease, beginning to close off.

1.4.1.3 Balbuena et al.

Growth mechanisms in MD simulations and the effect of temperature and substrate-catalyst interaction. In [93], Zhao, Martinez-Limia and Balbuena simulate the growth of carbon nanotubes using classical molecular dynamics with a reactive force field. For carbon-carbon interactions, they use a second-generation reactive empirical bond order (REBO) potential developed by Brenner et al. [21]. A weighting factor has been added to describe weaker C-C interactions inside the metal cluster. This factor varies with the number of Ni atoms bonded to the C atoms. Carbon-metal interactions are given by a many-body Morse-type potential, including dependence on the coordination number of C and Ni atoms. For the metal-metal interactions, a Morse-type potential is also used. Carbon atoms are added by including gaseous precursor atoms in the simulation. Once they reach the proximity of the catalyst surface, they are instantaneously transformed into carbon atoms, and a new precursor atom is added randomly. The authors observe that growth proceeds as follows: carbon atoms dissolve in the metal cluster, precipitate on the surface, form carbon structures (first chains, then graphene-like structures), and form a cap, which becomes a nanotube. They observe that the carbon solubility of the catalyst particle increases as temperature increases and decreases as the strength of the substrate-catalyst interaction increases. Once the carbon atoms on the surface have formed sp^2-bonded structures, they interact weakly with the catalyst and lift off the surface.

The authors observe that the caps are not very stable; they form, break, and re-form. More stable caps are observed at higher temperatures (1150-1200K). When the cap diameter matches the diameter of the catalyst nanoparticle, there is less stress on the cap.

Effect of substrate-catalyst interactions. In [10], Balbuena et al. specifically study the role of the catalyst in CNT growth. They perform MD simulations using the same potentials as in [93]. They simulate the Langevin equations rather than Newton's equations, which include random fluctuations and a friction force to sample the canonical ensemble. This supplies the energy needed to cross activation barriers and improve the sampling of configurations. A substrate is included in the simulations via a honeycomb lattice of atoms which interact with the metal and carbon atoms via a Lennard-Jones potential. These simulations show the same growth mechanisms as in [93]. Additionally, it is observed that a strong substrate-catalyst interaction constrains the cluster surface, increasing the cluster melting point and reducing the C solubility. This is similar to the effect of substrate-catalyst interactions in [74]. Separate molecular dynamics simulation are used to determine the melting point of small clusters of Pt atoms using a Sutton-Chen potential. The simulations show that the melting temperature of metal nanoclusters decreases as the cluster size decreases, with small dependencies on the cluster shape for larger clusters. The melting temperatures are in the range 850 K to 1125 K.

1.4.1.4   Maiti et al.

Energetics of catalyst-free, high-temperature growth of open CNTs. In [55], Maiti, Brabec, Roland, and Bernholc simulate the growth of CNTs by arc discharge, which involve high-temperature, catalyst-free conditions. They show that the electric field alone cannot stabilize the growth of open metallic tubes. To consider other reasons for the stability of an open edge, the authors study the addition of car-

bon atoms, dimers, and trimers to the open end of an achiral tube, i.e. one with a kink edge. The energy is described by a Brenner potential [20]. For monomer deposits, the only low-energy structure is an isolated pentagon at a step edge. For dimer deposits, there are two low-energy structures: a hexagon and a 5-5 pair at a step edge. The 5-5 pair is energetically favored for narrow, highly curved tubes, whereas the hexagon is favored for less curved, large diameter tubes. For trimer deposits, the lowest energy structures are: 5-5-5, 5-6, and 6-5. The 5-5-5 structure is the most stable energetically for very narrow tubes, but becomes unfavorable for larger tube diameters, where 5-6 and 6-5 structures are preferred. The 5-5 and 5-5-5 structures lead to highly curved tips that result in tube closure after more carbon atoms incorporate. Thus the narrow tubes, which energetically prefer these structures, will eventually close. Kinetic effects are studied by performing MD simulations at 3000 K. Annealing produces the low-energy structures identified above. MD simulations for carbon insertion in closed tubes result in disordered structures, showing that closed tubes are not able to grow.

Kinetics of catalyst-free, high-temperature growth of open CNTs. In [19], Brabec, Maiti, Roland, and Bernholc study the growth of carbon nanotubes using a classical MD method. They describe carbon-carbon interactions with a Brenner potential [20]. They initialize their simulations with open, all-hexagon nanotubes with various diameters and helicities. The bottom two atomic layers are held at 0 K, the tip is at 3000 K, and there is a constant temperature gradient between the two. They add single carbon atoms at random positions on the tip at a rate of 1 atom per 0.3 ns per unit nanometer length of the tube edge. This is much faster than experimental rates of one atom per $10^3 - 10^4$ ns, but such fast rates are needed to perform simulations in a reasonable amount of computer time. However, these rates still allow enough time for the system to anneal. The simulations reveal specific mechanisms of adatom addition and motion. Defect structures anneal on timescales of 10 to 100 ps. Heptagonal and pentagonal rings migrate along the edge via bond

switches and anneal into hexagonal rings by one of several mechanisms. Deposition on a wide 6 nm diameter tube maintains an all-hexagon structure. For a narrow 1.5 nm diameter tube, hexagons at step edges degenerate into pentagon pairs upon annealing. This introduces curvature at the tip, and the tubes close as more atoms are deposited.

1.4.1.5 Neyts et al.

Coupled MD-MC technique. In [62], Neyts, Shibuta, van Duin, and Bogaerts use a ReaxFF potential with a coupled Monte Carlo-MD method. The ReaxFF force field uses a similar bond order/bond distance relationship as the one used by the Brenner potential [20]. The energy also includes contributions from lone pairs, undercoordination, overcoordination, valence and torsion angles, conjugation, and hydrogen bonding, as well as van der Waals and Coulomb interactions. The authors' coupled Monte Carlo-MD method alternates between an MD stage and a uniform-acceptance force-biased Monte Carlo (UFMC) stage. The simulation temperature is 1200 K. The simulations are initialized with a prethermalized Ni_{32} cluster. One C atom is added at a random location in the simulation box every 2 ps. A repulsive Lennard-Jones potential prevents this atom from bonding with the CNT until the atom has been "catalyzed" by coming into contact with the Ni cluster. The Monte Carlo stage allows for defects to relax, and a CNT with definable chirality is obtained. The diameter is 11.45 Å and the chiral angle is 14 degrees, i.e. a (12,4) CNT. The authors observe growth occur in an 8-stage process:

1. **Alloying.** Carbon atoms adsorb on the cluster surface and dissolve, occupying subsurface sites. Carbon atoms do not bond together.

2. **Saturation and supersaturation.** As more carbon dissolves, carbon atoms begin to form dimers, and then trimers, which exist both on the surface and in the subsurface.

3. **Initial ring formation.** As carbon continues to absorb, rings begin to form after rearrangement of single chains, to which additional atoms may be added.

4. **Second generation ring formation.** Longer chains form, and eventually join to form rings. The fraction of single carbon atoms drops to about 5%.

5. **Graphitic island formation.** The addition of monomers, dimers, and trimers to rings form surface tails which later become rings.

6. **Coalescence of graphitic islands.** Graphitic islands are connected by chains. Addition of new atoms leads to bond rearrangement, causing the graphitic islands to coalesce. The graphitic islands conform to the shape of the catalyst. Some Ni atoms are separated from the larger Ni cluster.

7. **Cap and tube formation by root growth.** Graphitic islands grow from their edges, and eventually lift off from the surface. Initially, the cap is not spherical, but becomes more so as additional carbon atoms are incorporated.

8. **Tube formation by tip growth.** The lone Ni atoms may catalyze gas phase carbon to incorporate into the CNT. This results in the formation of a (defective) curved graphene sheet, which eventually curves into a tube. The metal atoms remain near the tip.

The authors also observe apparently metal-mediated defect healing mechanisms which transform pentagons and heptagons of carbon atoms into hexagons.

1.4.2   Semi-empirical potentials

1.4.2.1   Irle, Morokuma et al.

Dependence on catalyst composition, catalyst size, reaction temperature, and C addition rate. In [64], Page, Ohta, Irle, and Morokuma describe a

variety of previous work related to modeling CNT growth using quantum mechanical molecular dynamics. In particular, they use a self-consistent charge density-functional tight-binding methodology. They study Fe_{38}-catalyzed SWNT nucleation, Fe_{38}-catalyzed "cap-to-tube" transformation, and Fe_{38}-catalyzed continued SWNT growth. They also study the dependence on catalyst composition, catalyst size, reaction temperature, and C addition rate. All simulations except those exploring temperature dependence are performed at 1500 K.

In their study of SWNT nucleation, they observe that C_2 units bind to the Fe catalyst particle, diffuse, and fuse to form polyyne chains, i.e. chains of carbon atoms with alternating single and triple bonds. This process takes more than 100 ps. Then, polyyne chains condense into rings, beginning with a 5-membered ring. Carbon clusters retain branched polyyne chains throughout the simulation. The role of the catalyst is to localize the carbon precursor species, impede polyyne diffusion, and prevent the one end of the structure from closing. In particular, growth occurs even though a transition-metal carbide particle did not form, suggesting that such a particle is not a prerequisite for growth.

In the study of "cap-to-tube" transformation, they observe that when carbon atoms are added to the system, this causes the addition of 5-, 6-, and 7-membered rings at the cap-catalyst boundary, demonstrating nanotube sidewall construction.

In their study of continued SWNT growth, they observe that new carbon atoms insert into an existing C-Fe bond to form a C-C-Fe bridging structure. These bridging structures interact to form 5-, 6-, or other-membered rings. They find that catalyst composition affects the growth. Using Ni instead of Fe increases the growth rate, and longer chains (three or more) of carbon connecting the cap to the catalyst particle are observed compared with Fe. An increase in catalyst size corresponds to a decrease in SWNT growth rate, since the C atom is able to diffuse for a longer time before incorporating into the SWNT. The growth rate at 1500 K is greater than at 1000 K

or 2000 K. Adjustments to the carbon supply rate show that slower carbon supply rates (1 C every 10 or 20 ps) yield structures with fewer defects (5- and 7-membered rings) compared with faster rates (1 C every 0.5 ps). Other simulations show that adatoms, monovacancy, and 5-/7- membered ring defects heal on time scales of 1 – 25 ps.

Low-temperature, catalyst-free growth from nanoring precursors. In [49], Li, Page, Irle, and Morokuma perform quantum mechanical MD simulations of low-temperature catalyst-free SWNT growth from various chiral carbon nanoring precursors. These simulations use the same self-consistent charge density-functional tight-binding method used in [64]. Ethynyl radical (C_2H) is added to various nanoring precursors which serve as templates for (4,3), (6,5), (6,1), (10,1), and (8,0) SWNTs. There is no catalyst present, and the temperature is low (500 K). Armchair edge carbon atoms in the precursor serve as docking points for incoming radicals. This is also where new hexagon formation occurs. Near-zigzag precursors have only one such bonding site, and growth proceeds by sequential hexagon addition. Armchair and near-armchair precursors exhibit random hexagon formation. Zigzag SWNTs do not have these armchair docking locations, so their growth proceeds differently. As radicals are added, a 6-3 ring structure (benzocyclopropene) forms at the edge of the precursor. Hexagons add repeatedly to this armchair structure. However, the 6-3 ring structure prevents a complete row of hexagons from forming. A 6-3 to 6-6 ring isomerization does not occur in the 325 ps period simulated. DFT shows this isomerization to have a barrier of 12.1 kcal/mol (0.525 eV/atom) and to be exothermic by 33.1 kcal/mol (1.43 eV/atom). Thus there is a barrier to ring completion, in contrast with a barrier to ring initiation, which was identified in an article by Ding et al. [28]. Overall, Li et al. find that hexagon formation is more favored during the growth of near-armchair SWNTs compared to near-zigzag SWNTs, since growth rate is proportional to the number of armchair sites. This agrees with the findings in [28]

regarding the chirality dependence of catalytic CNT growth. The authors find that for C_2H addition, SWNT growth rate is independent of diameter. On the other hand, the barrier height for C_2H_2 addition decreases as diameter increases, so the growth rate would depend on diameter in this case. Although the barrier for C_2H_2 addition is about one order of magnitude greater than for C_2H addition, C_2H_2 addition may play a role in CNT growth since this molecule is much more plentiful in the growth atmosphere.

1.4.2.2 Andriotis et al.

The catalytic effect of a single Ni atom. In [6], Andriotis, Menon, and Froudakis apply a self-consistent tight-binding molecular-dynamics method [5] to the study of the catalytic effect of Ni atoms on carbon nanotubes, also employing static DFT calculations. They consider a graphene fragment and two armchair SWNT fragments of different sizes. They consider the substitution of a carbon atom in these structures with a single Ni atom, as may happen for a defective structure in the presence of a catalyst. For a substitutional Ni atom in a graphene sheet, the Ni atom moves slightly out-of-plane with minimal distortion to the graphene lattice. When there is an additional C atom present, the C atom and the Ni atom exchange places. For a substitutional Ni atom in a SWNT, the Ni atom moves into the interior of the nanotube, stabilizing the C vacancy. When Ni atom is added near the tube end, it prefers to remain in the tube end. If an additional C atom is present, the C atom replaces the Ni atom, and the Ni atom breaks free of the nanotube. Thus, the authors propose a two step growth process:

1. A Ni atom first creates and stabilizes defects in nanotubes.

2. Then, newly added carbon anneals these defects and the Ni atom is free to continue the process.

This is contrasted with the scooter mechanism proposed in [78], in which a single Ni atom diffuses around the open end of the CNT and heals defects as carbon atoms are added.

1.4.2.3 Amara et al.

Carbon nanostructures on a Ni slab, including the effect of carbon chemical potential and temperature. In [2], Amara, Bichara and Ducastelle simulate the formation of carbon nanostructures using tight-binding potentials. These potentials include a band structure term and an empirical repulsive term. A Monte Carlo scheme is used to simulate the dynamics. Carbon atoms are added and removed from the system by calculating acceptance probabilities consistent with a grand canonical ensemble, and they are only inserted on the top half of the catalyst. The system is initialized with a Ni slab with 6 atomic layers and a (111) surface. The chemical potential μ_C varies from -6.5 to -4.5 eV/atom, and the temperatures 500 K, 1000 K, and 1500 K are considered. In the simulations, the authors observe that carbon atoms are deposited on the surface or in interstitial sites. As more atoms are added, chains of carbon form on the surface and eventually demonstrate sp^2 hybridization. Once a graphene-like structure forms, it shows very weak bonding with the substrate. The authors observe that for large values of μ_C, a 3-D amorphous C phase forms. At 1500 K, a disordered carbide phase forms.

Tight-binding simulations of CNT growth on catalyst nanoparticles, including effect of catalyst size and carbon chemical potential. In [3], Amara, Bichara and Ducastelle use the same interaction potentials and dynamics as in [2] to simulate the catalytic growth of carbon nanotubes. Nickel catalyst clusters with various structure and size are used in the simulations. Some are crystalline, with an fcc (face-centered cubic) equilibrium Wulff shape, and others are disordered. Carbon atoms are inserted in a region between 3 Å below and 3 Å above the Ni surface. The

presence of a substrate is mimicked by making only the top 40% to 60% of the cluster active. Simulations are carried out with the carbon chemical potential of -6.00, -5.25, or -4.50 eV/atom and temperatures of 1000 K. For small chemical potential, carbide formation dominates as atoms are added, although crystalline catalyst clusters are not able to dissolve as much carbon as disordered clusters. For intermediate chemical potential, carbon atoms deposit on the surface, first forming chains, and then graphene-like structures. These graphene-like structures bond weakly with the catalyst and eventually dissociate. This is essentially the same mechanism observed by Zhao, Martinez-Limia, and Balbuena in their simulations using classical potentials [93]. For large chemical potentials, the carbon encapsulates the catalyst with a soot-like structure. The cap diameter is determined by the catalyst shape at the time of formation. The nanotubes exhibit a large number of defects.

Effect of catalyst structure. In [4], Amara, Bichara and Ducastelle use the same interaction potentials, dynamics, and addition scheme as in [3]. They consider crystalline and disordered nickel catalyst particles. The carbon chemical potential varies from -8.5 eV/atom to -5.25 eV/atom, and the temperature is 1000 K. They study how carbon solubility changes as the chemical potential is increased. When μ_C is above -6.50 or -6.00 eV/atom, the surface and bulk carbon atoms reach equilibrium values. The disordered catalyst accommodates more bulk C atoms than the crystalline catalyst. Once μ_C exceeds a threshold value μ_C^*, carbon atoms on the surface begin to bond together to form chains and graphene-like clusters. μ_C^* is between -6.50 and -6.00 eV/atom for the crystalline cluster and -6.00 and -5.75 eV/atom for the disordered one. When the chemical potential μ_C exceeds about -5.00 eV/atom, the catalyst cluster becomes encapsulated by carbon atoms. The authors suggest that one role of the metal catalyst is to confine C atoms near the surface until a critical concentration is reached.

Effect of carbon chemical potential and temperature, as well as catalyst

size and structure. In [26], Diarra, Amara, Ducastelle, and Bichara use the same potentials and dynamics as in [3]. Carbon atoms are added in the active zone between 2.5 Å below and 2.5 Å above the surface of the Ni cluster. The carbon chemical potential varies between -8.80 and -5.40 eV/atom. They consider temperatures between 800 K and 1400 K. Icosahedral and Wulff (fcc) Ni clusters of varying sizes are used as the catalyst. The authors observe that at high temperatures or at high chemical potential, the Ni clusters are molten. At low temperatures, carbon absorbs on the fcc cluster at a lower μ_C value than on the icosahedral cluster. Increasing μ_C causes a larger number of C atoms to absorb into the catalyst, until the carbon solubility limit of about 25% is reached. The catalyst cluster size also has an effect on carbon solubility. For fixed μ_C, the carbon solubility is larger for smaller clusters. The threshold μ_C value for carbon incorporation is temperature dependent for the smaller nanoparticles, but not for the largest one. The largest particle (805 Ni atoms) has a solid core/molten shell structure. The carbon is dissolved near the surface of the catalyst cluster. Temperature also affects the carbon solubility. At a given μ_C, higher temperatures display larger carbon content. The threshold pressure for carbon absorption increases with temperature. At low temperatures (800 K), the catalyst particle is encapsulated by carbon, but at higher temperatures (1000 K or 1200 K), a carbon cap forms on the catalyst particle.

1.4.3 First principles methods

1.4.3.1 Charlier et al.

Catalyst-free growth of open CNTs. In [24], Charlier, De Vita, Blase, and Car use *ab initio* molecular dynamics to study the growth mechanisms in carbon nanotubes. They use DFT in the local density approximation (LDA). They consider a zigzag nanotube, an armchair nanotube, and a zigzag double-walled nanotube (DWNT), all open at one end and H-terminated at the other end. No catalyst is

present. They consider growth temperatures of 3000 K to 3500 K to simulate arc discharge conditions. The authors observe that the open end of SWNTs close spontaneously into a graphitic dome. The open end of the zigzag nanotube closes into a structure with no two-coordinated atoms, which is about 18 eV more stable than the initial structure and 4.6 eV less stable than the C_{60}-hemisphere cap. The open end of the armchair SWNT closes into a hemi-C_{60}, with about 15 eV less energy than the initial configuration. Tip closure reduces the localized density of electronic states (LDOS), indicating reduced chemical activity. New C atoms are not able to incorporate into the closed tip. The situation is different for DWNTs. "Lip-lip" interactions in DWNTs prevent dome closure, but maintain high chemical activity, allowing for further carbon incorporation. The open end is trapped in a metastable energy minimum by the formation of bridging bonds between the adjacent tubes. The energy lowering due to these bridging bonds is about 1 eV per initial two-coordinated C atom. These edge structures display a large LDOS at the Fermi level, i.e. they have high chemical reactivity. If C atoms or dimers are projected toward the SWNT edge, they incorporate into the structure. These results agree with experiments that suggest that transition metal catalysts are necessary to produce SWNTs, but not MWNTs [30].[2]

Root-growth mechanism. In [33], Gavillet et al. perform *ab initio* molecular dynamics simulations to study the root-growth mechanism of SWNT growth. The first simulation considers a mixed Co-C cluster, with two-thirds carbon atoms, initially in an hcp (hexagonal close-packed) arrangement. The cluster is cooled from 2000 K to 1500 K. During cooling, about 80% of the C atoms segregate to the surface of the cluster, and Co atoms migrate to the center. The C atoms on the surface form

---

[2]Recent work by Chongwu Zhou and his colleagues [51, 50] has shown the possibility of catalyst-free growth of SWNTs by a vapor-phase epitaxy method. SWNT fragments undergo air annealing and water annealing to activate their open ends. When methane or ethanol are used as a feedstock, the SWNT fragments grow. The growth mechanism in these conditions is not completely understood, but it is hypothesized to be Diels-Alder addition.

linear chains and some aromatic rings, including a hexagon next to two pentagons. In a second simulation, the authors consider a C_{60} hemisphere on a double layer of hcp Co. An additional 20 C atoms are on the surface of the metal particle. The growth temperature is 1500 K. After 15 ps, 5 C atoms migrate to the tube base and incorporate into the nanotube. They identify the role of the catalyst as being to stabilize the forming tube and to provide fluctuating Co-C bonds, which allow for the incorporation of C atoms.

1.4.3.2   Raty, Gygi, and Galli

Root-growth mechanism, including effect of catalyst-carbon binding strength. In [71], Raty, Gygi, and Galli perform *ab initio* MD simulations of the growth of carbon nanotubes on metal nanoparticles. They use DFT in the generalized gradient approximation (GGA). Two different types of catalyst particles are considered – a 1 nm Fe catalyst in an fcc arrangement and a 1 nm Au catalyst. These catalysts have different binding strengths with carbon. The effect of a substrate is approximated by passivating the bottom half of the catalyst surface with hydrogen atoms. The system is initialized with some carbon atoms arranged on the catalyst surface. Additionally, C atoms are deposited near a random surface Fe atom that is not bonded to C or H at a rate of one atom every 0.3 ps. This addition rate is very high, but it is necessary to achieve reasonable simulation times. The growth temperature is 1200 K. C atoms do not move to subsurface locations, indicating that carbide formation is not necessary for growth. The C atoms on the surface of the Fe catalyst join to form dimers, chains, and eventually a sp^2-bonded graphene sheet. The threefold-coordinated carbon is loosely bound to the catalyst, and a cap lifts off the catalyst surface at its center. On the Au catalyst, however, C dimers and chains detach from the surface. The authors explain this in terms of the catalyst-carbon binding energy. The binding energy for a single C atom to a metal cluster is larger

for Fe than for Au (7.41 eV vs. 2.91 eV). Also, the binding energy for graphene is larger on Fe than Au. Thus, the graphitic structure is able to stick to the Fe surface, especially at the edges, but C atoms do not stick to the Au catalyst long enough to form a graphitic structure.

1.4.4   Comparison of CNT growth simulations

The works described here demonstrate a wide range of approaches to simulating CNT growth. Various empirical potentials are used, although carbon-carbon interactions are typically described by the first- or second-generation Brenner potential. Metal-metal and metal-carbon interactions are described by Morse, Johnson, and ReaxFF potentials, among others. Metal-substrate interactions are usually described by a Lennard-Jones potential. These potentials may have different weighting terms that depend on atomic coordination or on bond angles. The semi-empirical methods share the same tight-binding framework, although different research groups use different approximations. The first principles are all based on DFT, but this includes different approximations (LDA or GGA), as well as different pseudopotentials.

In terms of the dynamics, molecular dynamics is used in almost all simulations, except the work of Neyts et al., which includes a Monte Carlo stage, and of Amara et al., which uses a grand canonical Monte Carlo method. In most of the research discussed, carbon atoms are inserted at regular time intervals. The more realistic technique is to use a chemical potential, as done by Amara et al. The rate of carbon atom addition varies by several orders of magnitude, from one every 10^{-1} ps to one every 10^1 or 10^2 ps. This is largely dictated by the computational demands of the force calculations. In any case, these rates are much faster than the experimental rates of one every 10^6 or 10^7 ps. As a result, the system does not have enough time to relax to thermal equilibrium. Most of the work assumes that the carbon-containing precursor catalyzes instantaneously on the catalyst surface to form carbon atoms. The work

of Li, Page, Irle, and Morokuma [49] is noteworthy in that it considers the addition of ethynyl radicals instead of carbon atoms. This is a more chemically accurate description of the feedstock for CNT synthesis because carbon atoms are added two at a time, and the effect of hydrogen on the electronic structure is considered. Most of the simulations describe catalytic CVD growth of CNTs, and include a catalyst particle, although simulations of arc discharge or laser ablation methods may have a single catalyst particle, or no catalyst at all. The temperatures considered vary between 500 K for the growth of nanorings [49] to 3500 K for arc discharge conditions [24]. Common temperatures for CVD conditions is about 1500 K. Many of these studies focus on the nucleation of CNTs rather than the continued growth. Those interested in continued growth look at the incorporation of carbon atoms into a pre-existing carbon cap, nanotube fragment, or nanoring.

Despite the wide variety of atomistic models used, simulations of these models display quite similar growth mechanisms. These follow the general VLS framework. Carbon deposited on the catalyst surface by feedstock decomposition will diffuse either through the bulk or on the surface of the catalyst. As the concentration of carbon atoms on the surface increases, the carbon atoms will bond into chains and then graphene islands. As these islands grow, they coalesce to form a nanotube cap which lifts off the catalyst surface at its center. At this point, the nanotube has nucleated. The nanotube diameter is the same as or slightly smaller than the diameter of the catalyst particle. Additional carbon atoms will incorporate at the edge of the tube. The number of defects is usually quite high. This is quantified in terms of the number of hexagons vs. pentagons, heptagons, and other rings. In the simulation by Neyts et al. [62], the number of defects is low enough that the chirality of the nanotube is identifiable.

There is also good agreement regarding the dependence of the growth process on the variables. The simulations suggest that for a fixed model, slowing the addition

rate allows for defects to heal, leading to fewer defects. If the deposition rate is too high, the catalyst may become encapsulated by amorphous carbon. This can also occur if the temperature is too high or too low. The substrate composition plays a role in the growth, since increasing substrate-catalyst binding strength creates a layered catalyst structure, which produces hexagonal carbon structures on the surface, but prevents cap liftoff. The catalyst composition is also important, as decreasing the catalyst-carbon binding strength causes the carbon structures to detach from the catalyst particle before creating a cap.

There is disagreement about how much carbon dissolves into the catalyst and whether any dissolution is necessary for growth. There is also disagreement about the type and extent of carbon-carbon bonding in the subsurface. The simulations of Shibuta and Maruyama [73, 74] show hexagonal rings of carbon in the subsurface, whereas subsurface carbon atoms in other simulations are bonded to at most two other carbon atoms.

The greatest drawback of the simulation of these atomistic models is their high defect concentration. Nanotubes grown in experiments typically have less defective lattice structure on their sidewalls. The simulations described here indicate that slowing the addition rate decreases the number of defects, but none of the simulation methods are able to access the time scales necessary to produce high quality, let alone perfect, tubes. In order to understand the mechanisms of defect-free carbon incorporation, other approaches are necessary.

1.5   Review of energetic studies of CNT and graphene growth

Alternative approaches by Yakobson and his colleagues provide further insight into the CNT and graphene growth mechanisms. These studies are based on energy calculations via DFT. Combined with statistical mechanics and transition state theory, these energy calculations can yield the probabilities of defect-free and various

defected configurations and the transition rates between them. This requires identifying the local minima and saddle points of the energy surface, e.g. by using a nudged elastic band method.

1.5.1 Chirality-controlled growth

In [28], Ding, Harutyunyan, and Yakobson propose that the CNT growth rate is correlated with chiral angle. An (n, m) CNT has m kinks at the end rim, which serve as preferred locations for carbon atoms to incorporate. Achiral edges (armchair and zigzag) do not have kinks, and must nucleate a new row after one row is complete. This nucleation involves a significant energy barrier G^*. The authors calculate this energy barrier via DFT calculations for a CNT edge docked to a step edge in the catalyst surface. The energy barrier for an armchair edge on catalysts Fe, Co, and Ni is $G^*_{AC} = 0.06$, 0.12, and 0.04 eV, respectively. For a zigzag edge on catalysts Fe, Co, and Ni, G^*_Z is 1.41, 1.12, and 1.54 eV, respectively. Since a temperature of 1200 K corresponds to 0.1 eV, the re-initiation barrier for armchair tubes is negligible, but the barrier for zigzag tubes is significant. The ratio of the growth rates can be estimated as $\exp[-(G^*_{ZZ} - G^*_{AC})/kT] \sim 10^{-6} - 10^{-4}$ at $T \approx 1200$ K. A chiral nanotube with diameter d should gain atoms at the m kinks at some rate k_0, for a carbon deposition rate of $K = k_0 m$. We have $m \sim d \sin(\theta)$ for the chiral angle θ. The growth rate is thus

$$K_l \sim K/d \sim k_0 \sin(\theta) \propto \theta \tag{1.1}$$

This equation predicts greater abundance of nearly armchair compared to nearly zigzag. The distribution of chiral angles predicted by the theory agrees well with those in the experimental literature for a variety of common growth methods. A basic assumption of this model is that the attachment of carbon to the tube edge is

rate-limiting.

1.5.2   Energetic barrier to carbon atom incorporation

As has already been discussed, CNT growth consists of several steps:

1. transport of the precursor to the catalyst particle;

2. decomposition of the precursor on the catalyst;

3. diffusion of the carbon to the CNT-catalyst interface, either on the catalyst surface or in the catalyst bulk; and

4. incorporation of the C atoms into the nanotube.

Each of these steps has a rate, usually controlled by an activation barrier. In [90], Yuan, Hu, and Ding point out that if the growth rate correlates strongly with the chiral angle, then the rate-limiting step must be step 4, the carbon incorporation. They use DFT to calculate the activation energy for carbon incorporation, for both the first and second atoms added at the edge to form a six-member ring, for several choices of catalyst. The climbing-image nudged elastic band (cNEB) method is used to find transition states. Their calculations demonstrate that the barriers of incorporating two C atoms into the CNT are 1.85, 2.28, and 2.27 eV for catalysts Fe, Co, and Ni, respectively. The threshold barrier on Fe is the lowest of the three, suggesting it has the highest catalytic activity for CNT growth. For comparison, C diffusion on metal surfaces has a barrier less than 1.0 eV, and C feedstock decomposition on metal has a barrier less than 1.5 eV. Thus, C incorporation is the rate-limiting step.

Their calculations illuminate the process of carbon incorporation. On Ni, the first C incorporation proceeds as follows. The C atom is initially located at the center of four Ni atoms. It then diffuses through the subsurface to form a metal-stabilized hexagon structure. This process is exothermic with an activation barrier of 1.02 eV

and an energy decrease of 0.9 eV. The second C atom incorporation involves the removal of the Ni atom that stabilizes the hexagon structure. There is a small barrier to form a C-C bond between the second and first C atom. There is an activation barrier of 1.20 eV barrier to rotate the bond to form a hexagon and move the Ni atom away. The overall barrier of the two-atom incorporation reaction is 2.27 eV. This neglects the barriers of C feedstock decomposition, as well as C and Ni atom diffusion on the Ni(111) surface.

In experiments, C feedstock with energy higher than a CNT is used, i.e. there is a chemical potential difference $\Delta\mu$. This provides the driving force for CNT growth. Using the calculated energy barriers, the authors calculate a formula for an upper bound on the CNT growth rate. This formula indicates that growth of 0.1-1 m long CNTs in 1 h is theoretically possible.

1.5.3 Efficient defect healing

In [91], Yuan, Xu, Yakobson, and Ding study the energetics of topological defects in CNTs and their kinetic healing. A non-six-membered ring constitutes a topological defect in the CNT wall. An isolated pentagon (p) turns an otherwise defect-free SWNT into a cone; an isolated heptagon (h) turns it into a horn. A 5-7 pair and other defect clusters maintain the SWNT structure, but change the chiral index. Of these, the 5-7 defect has the lowest formation energy. In experiments, nanotubes of length 18 cm have been grown with the same chiral indices throughout. Thus, the defect concentration for such nanotubes must be less than 10^{-10}. In thermodynamic equilibrium, the number of defects is

$$(1.2) \qquad\qquad N_d = N_s \exp\left(-\frac{E_f}{k_B T}\right).$$

N_s is the number of lattice sites, k_B is the Boltzmann constant, E_f is the formation energy, and T is the temperature. For the defect concentration to be less than 10^{-10} at 800 – 1000°C, then the energy of formation must be greater than about 2.0 eV.

Using DFT calculations, the authors calculate the energy barriers E^* to defect healing on the outermost edge of a SWNT for three different catalysts:

	Fe	Co	Ni
p	0.55 eV	0.96 eV	0.91 eV
h	1.12 eV	1.36 eV	1.40 eV
5-7	1.61 eV	1.88 eV	2.00 eV

Based on the activation barriers for defect healing, p and h defects can be healed in a time period of 10^{-8} to 10^{-7} s. If a p or h survives in a CNT, and the CNT continues to grow, then they must combine to form a 5-7 pair. There is high defect healing efficiency on the outermost edge of a CNT. For the healing of a 5-7 defect, the barrier becomes higher and higher and the reactive energy becomes lower and lower when the 5-7 pair moves away from the CNT-catalyst interface. The authors calculate the defect concentration over a temperature range of 400 K to 1600 K with several different C addition rates ranging from 0.01 μm/s to 100 μm/s. For a given growth rate, the defect concentration is locally minimized at two different temperatures. For example, a growth rate of 1 μm/s results in a minimal defect concentration of about 10^{-11} at a temperature of about 700 K and a slightly greater locally minimal defect concentration at 1000 K. The defect concentration of a fast growing CNT is always higher than that of a slow growing one. MD simulations involve very fast growth rates, which explains the highly defective CNTs obtained in these simulations.

1.5.4 Equilibrium and non-equilibrium growth of graphene

In [7], Artyukhov, Liu, and Yakobson propose a "nanoreactor" mechanism which uses ideas of step-flow crystal growth augmented by detailed first-principles calcula-

tions. This analysis is for graphene, not CNTs. The edge energy of graphene as a function of chiral angle is $\gamma(\chi) = 2\gamma_A \sin(\chi) + 2\gamma_Z \cos(30° - \chi)$. γ_A and γ_Z are the edge energies for armchair and zigzag edges, respectively. The authors calculate the energy of armchair (A) and zigzag (Z) edges on different catalysts using DFT. They consider a reconstructed form of the armchair edge, denoted A5′, which has lower energy than the pure armchair edge. They find that $\gamma_{A5'} < \gamma_Z$ on Fe and Co, and the two are almost equal on Ni. On Cu, the zigzag edge has the lowest energy density. Using the Wulff construction, one can find the equilibrium island shape on different catalysts. On Ni, graphene will form a many-sided island with a combination of Z and A5′ edges. On Fe and Co, the A5′ edge dominates, producing hexagonal islands. On Cu, the Z edge dominates, again producing hexagonal islands.

For small islands or slow growth, the islands will be able to attain their equilibrium shape. Further from equilibrium, the growth rate is determined by the process of atom attachment. The authors add atoms to A5′ and Z Ni edges with non-growing edges docked to a metal step. They use DFT to calculate the energy for multiple metastable configurations, both the lowest energy state and possible defects. They observe that the catalyst substrate serves as a planar template for graphene growth. It also prevents the formation of defects at the growth front by biasing the energy toward hexagonal structures, which are sometimes less energetically favorable in vacuum.

The energy of the armchair and zigzag edges follow an up-down pattern as atoms are added at the kinks to produce additional hexagons. The growth of zigzag edges proceeds by 2 stages: (1) nucleation of a new atomic row, and (2) addition of atoms at kink sites (kink flow). Thus, for zigzag edges, the first atom addition is strongly endoergic, but subsequent zigzag additions lie below the high-energy states for armchair edges. For chiral orientations intermediate between zigzag and armchair, the concentration of kinks determines the growth rate. Let E represent the free energy barrier for carbon incorporation and N^* represent the critical Z nucleus size. Let s_K,

s_A, and s_Z denote the concentration of active sites at kink, armchair, and zigzag edge segments, respectively. The direction-dependent growth velocity is:

$$(1.3) \qquad v(\chi) \propto 2s_K(\chi)e^{-E_K/kT} + 2s_A(\chi)e^{-E_A/kT} + N^* s_Z(\chi)e^{-E_Z/kT}$$

This growth velocity is smallest for zigzag edges. The authors find that a growing island is a hexagon with only zigzag edges, since the shape is limited by the lagging zigzag edge. For nanotubes, the situation is different. The fixed chirality prescribes the edge orientation, and therefore the growth rate.

1.5.5 CNT growth on a solid metal catalyst

In [8], Artyukhov, Penev, and Yakobson combine CNT-catalyst interface thermodynamics with kinetic growth theory to show preference for near-armchair tubes. Let $N_{\chi,d}$ and $R_{\chi,d}$ represent the nucleation probability and growth rate, respectively, of a CNT with chiral angle χ and diameter d. The relative abundance of CNTs of different types is $A_{\chi,d} = N_{\chi,d} R_{\chi,d}$. The authors consider a low-temperature process with a solid catalyst, which affects the energy of the CNT nucleus and the insertion of new C atoms. The kinks at the edge of the CNT cause gaps between the catalyst and the CNT. Achiral edges (armchair and zigzag) form tight low-energy contacts. The interface energy increases roughly proportional to the number of kinks, which increases linearly with the deviation from the achiral direction. Let x denote the angular deviation from the achiral direction (either A or Z), and $\gamma + \gamma' x$ be the linearized edge energy in the neighborhood of the A and Z chiralities. Using a continuum model, the authors calculate the nucleation probability $N(\chi, d) \propto \exp[-\pi d(\gamma + \gamma' x)/(k_B T)]$. The nucleation probability is actually somewhat higher for single-kink tubes, since they are able to tilt off axis to decrease the edge energy. Let C denote the bending rigidity of graphene and E the energy barrier

for the initiation of a new atomic row on an achiral edge. The growth rate is then $R(\chi, d) \propto \pi d \exp\left(-\frac{2C}{d^2 k_B T}\right)(x + \exp(-E/(k_B T)))$. For a given diameter, this gives a dependence of the function form $A(x) = N(x)R(x) \sim xe^{-x}$. The authors then use DFT to perform atomistic calculations of the energy. For the CNT-catalyst energy, zigzag and armchair form local energy minima, with armchair tubes having lower energy than zigzag edges. Atomistic calculations for growth kinetics build on an earlier approach for graphene [7]. Energy changes and activation barriers for dimer addition are calculated using classical MD and the ReaxFF force field with a DFT-based correction scheme. The constantly changing tilt angle makes the situation different than for graphene. Armchair and zizgag edges have energy maxima for the first dimer addition and one of the later dimer additions in the ring. The energy barriers are: $\Delta G_A \approx 1.67 - 1.86$ eV and $\Delta G_Z > 3$ eV. Thus, under realistic conditions, the growth rate of achiral CNTs is negligible. This explains the predominance of near-armchair CNTs. This agrees with experiments in catalytic CNT growth, which show a strong preference towards near-armchair tubes of type $(n, n - 1)$.

1.5.6 Summary

The work of Yakobson et al. gives an energetics-based description for carbon addition to carbon nanotubes and graphene on solid and liquid catalysts, as well as the energetics of defect healing on a liquid catalyst. In [28], Ding et al. show the preference of C to incorporate at kink sites and calculate the energy of row nucleation at a metal step edge. In [90], Yuan et al. show the mechanism of the first and second C incorporation at a step edge in order to form a new hexagon. In [91], Yuan et al. show the energetics and kinetics of healing pentagonal, heptagonal, and 5-7 pair defects at or near a step edge. In [7], Artyukhov et al. calculate the edge energy and the activation energy of C incorporation on graphene edges with different chiral angles. In [8], Artyukhov et al. show the mechanism of carbon incorporation at armchair and zigzag

edge of a CNT on a solid catalyst (no step edge). These studies have precedents in the work of Maiti et al. [55] and Brabec et al. [19], which describe the energetics and kinetics of C incorporation on an open CNT edge and show that hexagons are preferred in wider tubes, whereas pentagonal defects are preferred in narrower tubes. These energetic calculations provide a path to transition rate calculations, which can be incorporated into models based on chemical kinetics.

1.6 Review of a kinetic model of CNT growth

Kinetic models of CNT growth are based on the rate constants of different chemical reactions. In [69], Puretzky et al. describe in situ measurements of CNT growth and a corresponding kinetic model. They perform experiments in which vertically aligned nanotube arrays are grown on Al/Fe/Mo multilayered catalysts on Si substrates, using acetylene (C_2H_2) feedstock at various concentrations at temperatures ranging from 535°C to 900°C (808 K to 1173 K). They measure forest height as a function of time. As temperature increases from 575°C (848 K) to 700°C (973 K), the growth rate and maximum achievable length increase. Increases in temperature above 700°C lead to a decrease in growth rate and terminal length. The maximum growth rate of about 0.2 μm/s occurs at 700°C. Changing the feedstock concentration does not have much effect on the maximum growth rate, but the terminal length can be increased by decreasing the feedstock concentration (from 19 sccm to 2 sccm).

For their kinetic model, they adopt the general VLS framework. They assume the following mechanisms. A fraction of the feedstock particles colliding with the catalyst surface decompose. Other studies show that the decomposition of acetylene on Fe leads to the formation of two CH radicals or C_2H and H radicals, which further decompose into carbon atoms and hydrogen atoms. Carbon atoms on the surface dissolve into the "molten" layer with rate k_{sb}. Carbon atoms diffuse much faster through the liquid layer than through the solid layer. They incorporate into the

nanotube with rate k_t. A fraction of the carbon atoms on the catalyst surface form a carbonaceous layer, which restricts the source flux. This occurs with rate constant k_{cl}. Another mechanism is needed to describe the growth at high temperatures – such as gas-phase pyrolysis products adding to the carbonaceous layer, or oxidation/reduction creating an effective inactive catalyst layer. The carbonaceous layer may dissolve and the inactive catalyst may reactivate. Activation barriers and pre-exponential factors are chosen such that at $T = 575°\text{C}$, $k_{cl} = 3 \times 10^{-3}$ s^{-1}, $k_{sb} = 17$ s^{-1}, and $k_t = 491$ s^{-1}. Thus we see that the formation of the carbonaceous layer is significantly slower than the other processes.

This model yields a set of differential equations (see Chapter III). The authors determine an explicit solution of these equations in a simplified case where the gas-phase pyrolysis of the feedstock, the catalyst deactivation step, and the dissolution of the carbonaceous layer are all neglected. This should be a good approximation at low temperatures. In this case, they find the termination length depends exponentially on $1/T$. Considering different versions of the full model and comparing with their experimental results, they deduce that poisoning of the catalyst nanoparticles by gas-phase pyrolysis products is not dominant at higher growth temperatures. Catalyst deactivation provides a better fit to the measured growth rates.

1.7 Connections between atomistic models and kinetic models

Atomistic models and kinetic models differ in important ways. In atomistic models, the initial atomic structure of the system, the atom addition scheme, and the interatomic interactions are specified, and then Newton's equations or the Langevin equations for the system are solved. Mechanisms can be deduced from the time-dependent behavior of the system. For kinetic models, the mechanisms are specified

based on experimental observations or theoretical considerations. The activation energy and rate of each of these mechanisms can be determined from other experiments or from atomistic modeling. The activation energies, specified in a kinetic model and intrinsic to an atomistic model, introduce temperature dependence into the growth process.

The mechanisms included in the Puretzky kinetic model are feedstock decomposition, carbon dissolution, carbon diffusion, carbon incorporation, and catalyst encapsulation. The Puretzky model does not include nanotube nucleation. We compare how these mechanisms are treated in kinetic models and atomistic models:

- **Feedstock decomposition.** Atomistic models typically do not capture decomposition of the feedstock in a detailed way, probably because the atomic mechanisms of this process are not well understood. In most simulations, carbon atoms are inserted near the surface of the catalyst particle at a specified rate, although some other mechanisms are considered. This corresponds to an instantaneous, barrier-free feedstock decomposition. In reality, this process would have an activation energy, which would slow the decomposition rate, and thereby the growth rate. This activation energy is included in the Puretzky kinetic model.

- **Carbon dissolution, carbon diffusion and carbon incorporation.** Atomistic models do capture carbon diffusion and carbon precipitation into the nanotube, mechanisms which are also included in the Puretzky kinetic model. Various atomistic models differ on whether carbon dissolution is a prerequisite for carbon diffusion, i.e. whether surface diffusion or bulk diffusion predominates.[3] The Puretzky model presupposes that the carbon atoms first dissolve into an outer liquid layer of the catalyst before diffusing to the nanotube edge. The

---

[3]This ambiguity is also present in experimental work, see e.g. the discussion in [86]. The activation energy for CNT growth may be more similar to the activation energy for bulk diffusion or surface diffusion, depending on the growth conditions.

Puretzky kinetic model does not include details of the nanotube structure or carbon incorporation. Atomistic modeling, however, is able to predict chirality dependence of the growth rate [28], as well as the kinetics of defect formation/healing [91], for the steady growth of CNTs.

- **CNT nucleation.** The process of CNT nucleation is described by atomistic models. A certain amount of carbon atoms must be deposited before they bond together and form a nanotube cap. However, the Puretzky kinetic model includes no delay between the initial decomposition of carbon on the catalyst surface and the growth of the nanotube.

- **Catalyst encapsulation and growth termination.** Atomistic models do demonstrate catalyst encapsulation for certain growth conditions, such as very low or very high temperature, high carbon addition rate, or high catalyst-carbon adhesion. In these cases, however, encapsulation by amorphous carbon affects the entire catalyst particle and no nanotube forms. In the Puretzky kinetic model, catalyst encapsulation is a gradual process that occurs simultaneously with nanotube growth, until the entire catalyst particle is encapsulated and growth terminates.

The choice between an atomistic model and a kinetic model for a process like CNT synthesis requires considering what aspects of the process one wishes to describe. If a description of atomic structure is desired, then an atomistic model is necessary. However, if this level of detail is not needed, but rather large-scale quantities such as the number of carbon atoms in the nanotube tube, then a kinetic model may be sufficient. It has the advantage of allowing for much longer time scales to be studied. The Puretzky kinetic model in particular also includes a mechanism for growth termination. Thus, this model is very helpful for describing CNT growth over the time scales of an actual CNT growth experiment. In this dissertation, we use atomistic

models when we wish to study the atomic mechanism of CNT growth, especially the formation and healing of defects (see Chapter II). We use a kinetic model when we wish to describe the growth of CNT forests to termination (see Chapter III).

CHAPTER II

Atomistic modeling of carbon nanotube growth

In this chapter, we describe an atomistic model of the growth of individual CNTs, as well as a simplified atomistic model that can be considered an analogue of CNT growth. Atomistic models can be used to explore many aspects of growth and their dependence on different growth conditions. One aspect of particular interest to our group is the effect of mechanical forces. CNTs within a pillar growing from nearby catalyst particles come in contact as they grow, i.e. they come near enough that there are van der Waals interactions between them. If these CNTs are growing at different rates, they exert forces on each other, which is hypothesized to lead to tortuous nanotubes with many defects [13]. Not only do applied forces occur naturally within the growth of CNT pillars, but they could be exerted on a pillar via an external mechanism. Recent experiments by Bedewy et al. [11] have explored the effect of applied forces on growth rate and forest height.

Our goal is to develop an atomistic model of CNT growth that includes a description of the growth rate and defect density of the CNT. In the future, external mechanical forces could be included in this model, and their effect on the growth could be studied. Even our relatively simple model of CNT growth is difficult to simulate over the long time scales needed for high quality growth, and its complicated potentials make it difficult to analyze mathematically. As a result, we give particu-

lar attention to the development and analysis of a one-dimensional analogue of this model. This one-dimensional model has a potential energy with a global minimum and multiple local minima, similar to the full CNT growth model. It does not include any topological defects, but the higher-energy local minima can be considered as defective states. Our analysis of this model gives some insights into CNT growth.

2.1 Full three-dimensional model

As discussed in Chapter I, various atomistic models have been developed for molecular simulation of CNT growth, using empirical, semi-empirical, and first principles methods. Typical empirical potentials used are the Brenner potential [20] for carbon-carbon interactions and the Morse potential for catalyst-carbon and substrate-carbon interactions. We use these potentials to model the continued growth of a CNT that has already nucleated. These potentials are based on a pair potential involving both a repulsive and an attractive part. The range of the potential is limited by a cutoff function f:

$$(2.1) \qquad f(r) = \begin{cases} 1 & \text{if } r < R_1 \\ \frac{1}{2}\left(1 + \cos(\pi(r - R_1)/(R_2 - R_1))\right) & \text{if } R_1 < r < R_2 \\ 0 & \text{if } R_2 < r. \end{cases}$$

The variable r represents the distance between atoms, and the parameters R_1 and R_2 define the interval where the function decreases from 1 to 0. The function is plotted in Figure 2.1 with $R_1 = 1.7$ Å and $R_2 = 2.0$ Å.
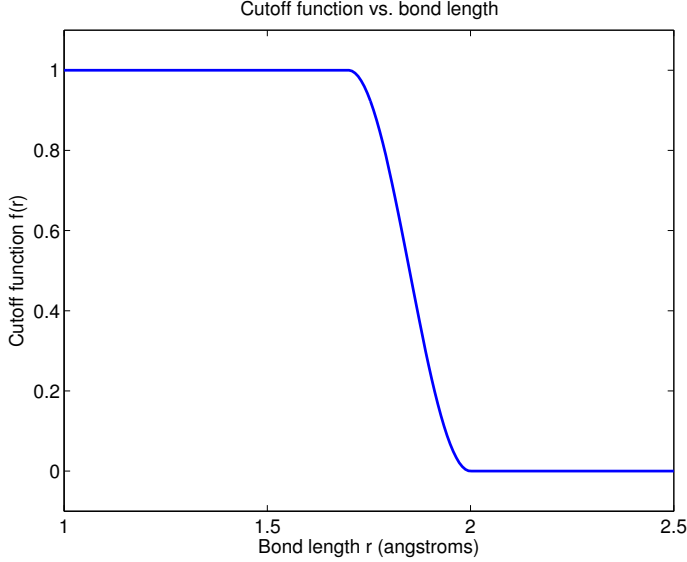
Figure 2.1: Plot of the cutoff function $f(r)$.

The repulsive and attractive potentials[1] are

$$(2.2) \qquad V_R(r) = f(r)\frac{D}{S-1}\exp\left(-\sqrt{2S}\beta(r - R_e)\right), \text{ and}$$

$$(2.3) \qquad V_A(r) = f(r)\frac{DS}{S-1}\exp\left(-\sqrt{2/S}\beta(r - R_e)\right).$$

R_e is the equilibrium bond length and D, S, and β are parameters that control the shape of the potential.

In a full model, one would need to include all the catalyst and substrate atoms. We assume that during continued growth of the CNT, the catalyst and substrate atoms are approximately static, and we do not simulate their motion. We further assume that we can replace the individual catalyst and substrate atoms with continua. This is similar to the approach of Schebarchov et al. in [72]. We take the catalyst to be a sphere with center at the origin and radius R_{cat}. The parameter values used for (metal) catalyst-carbon interactions are $D_{MC} = 1.0$ eV, $S_{MC} = 1.3$, $\beta_{MC} = 1.5$ Å^{-1},

---

[1]Here β appears as a parameter in the potential. Later in this chapter, we will use β for the inverse temperature.

$R_{e,MC} = 1.0$ Å, $R_{1,MC} = 2.0$ Å, $R_{2,MC} = 3.0$ Å. The potential for the catalyst-carbon interaction is:

$$(2.4) \qquad V_{MC} = \sum_i V_R(r_i - R_{\text{cat}}) - V_A(r_i - R_{\text{cat}}),$$

where r_i is the distance from the origin to the i-th carbon atom.

The substrate is modeled as a plane at $z = -R_{e,SC}$. It has a very weak interaction with the carbon atoms, so that the carbon atoms do not wet the substrate. The parameter values used for substrate-carbon interactions are $D_{SC} = 0.1$ eV, $S_{SC} = 1.3$, $\beta_{SC} = 1.5$ Å^{-1}, $R_{e,SC} = 1.0$ Å, $R_{1,SC} = 2.0$ Å, $R_{2,SC} = 3.0$ Å. The potential for the substrate-carbon interaction is:

$$(2.5) \qquad V_{SC} = \sum_i V_R(z_i + R_{e,SC}) - V_A(z_i + R_{e,SC}),$$

where z_i is the z-coordinate of the i-th carbon atom.

All of the carbon atoms are modeled, so we must sum over all pairs of carbon atoms to calculate the potential for the carbon-carbon interaction. In addition, the Brenner potential involves the bond order $\bar{B}$, which involves triples of carbon atoms. The bond order involves the parameters δ, a_0, c_0, and d_0. The parameter values used for carbon-carbon interactions are $D_C = 6.325$ eV, $S_C = 1.29$, $\beta_C = 1.5$ Å^{-1}, $R_{e,C} = 1.315$ Å, $R_{1,C} = 1.7$ Å, $R_{2,C} = 2.0$ Å, $\delta = 0.80469$, $a_0 = 0.011304$, $c_0 = 19.0$, and $d_0 = 2.5$. The potential for the carbon-carbon interaction is

$$(2.6) \qquad V_C = \sum_i \sum_{j>i} V_R(r_{ij}) - \bar{B}_{ij} V_A(r_{ij}),$$

where r_{ij} is the distance between the i-th and j-th carbon atoms. In Figure 2.2, this potential is plotted with and without cutoffs for several values of $\bar{B}_{ij}$, based on values arising in a lattice structure, where the bond order is the same for every bond.
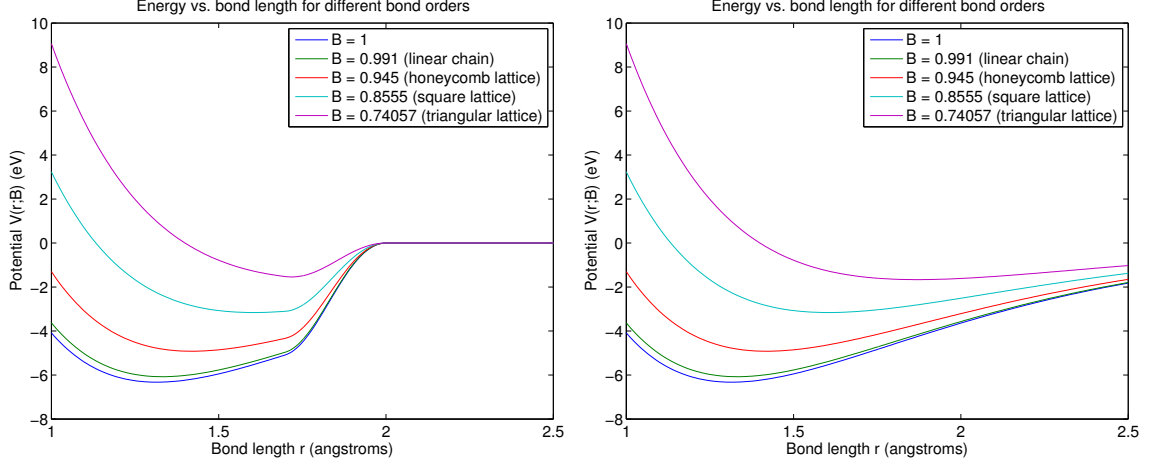
Figure 2.2: Plot of the pair potential $V_R(r) - BV_A(r)$. (*left*) With cutoff and (*right*) without cutoff. The values for B correspond to the bond orders in the specified lattice.

The bond order $\bar{B}_{ij} = \frac{1}{2}(B_{ij} + B_{ji})$, where

$$(2.7) \qquad B_{ij} = \left(1 + \sum_{k \notin \{i,j\}} G(\theta_{ijk}) f(r_{ik})\right)^{-\delta}.$$

Note that θ_{ijk} is the angle between the vector connecting the i-th and j-th carbon atoms and the vector connecting the i-th and k-th carbon atoms.

The angular function G is defined as

$$(2.8) \qquad G(\theta) = a_0 \left(1 + \frac{c_0^2}{d_0^2} - \frac{c_0^2}{d_0^2 + (1 + \cos \theta)^2}\right).$$

$G(\theta)$ takes its minimum value when $\theta = \pi$, which in turn gives a greater value for B_{ij} and a lesser value for V_C. The function G and the corresponding bond order B_{ij} are plotted in Figure 2.3.

The overall potential energy for the system is

$$(2.9) \qquad V = V_C + V_{MC} + V_{SC}.$$
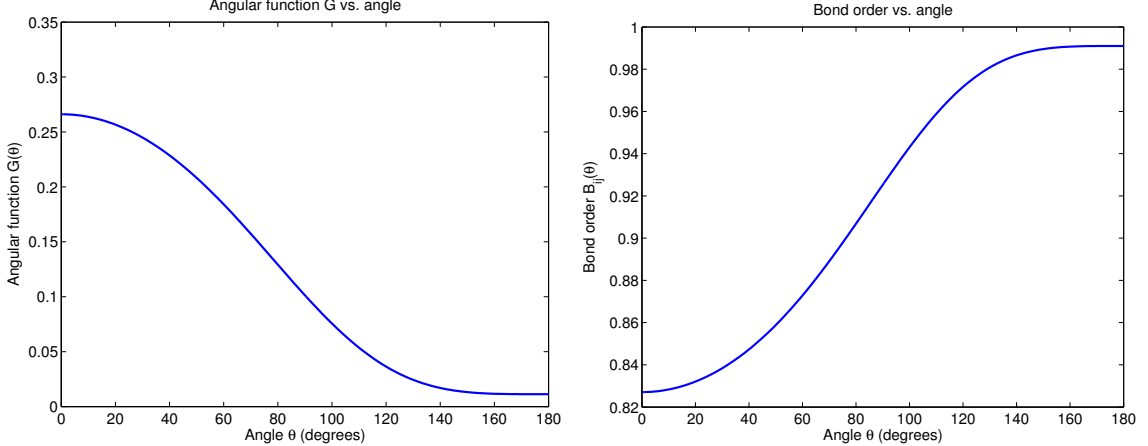
Figure 2.3: (*left*) Plot of the angular function $G(\theta)$. (*right*) Plot of the bond order B_{ij} when atom i is bonded to atoms j and k with angle θ.

We perform MD simulations of this model in three dimensions. We initialize the MD simulations with a defect-free armchair nanotube consisting of 90 atoms. Its radius is $R_{\text{tube}} = R_{\text{cat}} + R_{e,MC}$. We have considered both overdamped Langevin dynamics and Langevin dynamics with a time step of 0.5 fs.

The configuration of the system is given by $q \in \mathbb{R}^{3N}$, consisting of the x-, y-, and z-coordinates of all N atoms. The evolution equation for overdamped Langevin dynamics [48] is

$$(2.10) \qquad dq_t = -\nabla V(q_t)dt + \sqrt{\frac{2}{\beta}}dW_t,$$

where $\beta = (kT)^{-1}$ is the inverse temperature and $t \mapsto W_t$ is a standard $3N$-dimensional Wiener process. For the time discretization, we use the Euler-Maruyama scheme:

$$(2.11) \qquad q^{n+1} = q^n - \Delta t\nabla V(q^n) + \sqrt{\frac{2\Delta t}{\beta}}G^n,$$

where $(G^n)_{n\geq 0}$ are i.i.d. centered Gaussian random vectors in $\mathbb{R}^{3N}$ with identity co-

variance matrix:

$$(2.12) \qquad\qquad \mathbb{E}(G^n \otimes G^n) = \mathrm{Id}_{3N}.$$

In our simulations, we approximate the Gaussian distributed random vectors by a sum of 12 uniformly distributed random vectors, i.e. $G^n \approx \left(\sum_{i=1}^{12} \mu_i\right) - 6(1,1,1)^T$, where μ_i are independent random vectors with components uniformly distributed on the interval $(0,1)$. As can be seen in Figure 2.4, the probability distributions for each of the components is in close agreement with the standard normal distribution.
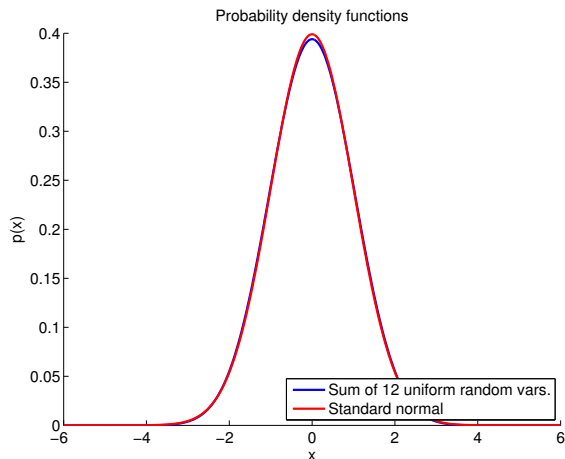
Figure 2.4: Plot of the standard normal, i.e. Gaussian, distribution and the approximation by a sum of uniformly distributed numbers.

The Langevin dynamics includes the momenta $p \in \mathbb{R}^{3N}$ and is based on the Hamiltonian

$$(2.13) \qquad\qquad H(q,p) = \frac{1}{2} p^T M^{-1} p + V(q),$$

where M is the mass matrix. The evolution equations are

$$(2.14) \qquad \begin{cases} dq_t = M^{-1} p_t dt \\[2mm] dp_t = -\nabla V(q_t) dt - \gamma(q_t) M^{-1} p_t dt + \sigma(q_t) dW_t \end{cases}$$

45

Again, $t \mapsto W_t$ is a standard $3N$-dimensional Wiener process. The coefficients γ and σ are $3N \times 3N$ real matrices, which we take to be proportional to the identity matrix. The parameter γ controls the strength of the frictional force and σ controls the strength of the random force. They are related through the fluctuation-dissipation relation:

$$(2.15) \qquad \sigma\sigma^T = \frac{2\gamma}{\beta}.$$

This process samples the canonical measure

$$(2.16) \qquad \mu(dq\,dp) = Z_\mu^{-1}\exp(-\beta H(q,p))dq\,dp,$$

where β is the inverse temperature and Z_μ is a normalization constant. The function $Z_\mu^{-1}\exp(-\beta H(q,p))$ is called the Boltzmann-Gibbs distribution.

The numerical scheme uses a splitting procedure for the Hamiltonian part and the thermostat part. We use the Brünger-Brooks-Karplus (BBK) integrator [23], which has an Explicit Euler–Verlet–Implict Euler splitting:

(2.17)
$$\begin{cases} p^{n+1/2} = p^n - \dfrac{\Delta t}{2}\nabla V(q^n) - \dfrac{\Delta t}{2}\gamma(q^n)M^{-1}p^n + \sqrt{\dfrac{\Delta t}{2}}\sigma(q^n)G^n, \\[2mm] q^{n+1} = q^n + \Delta t M^{-1}p^{n+1/2}, \\[2mm] p^{n+1} = p^{n+1/2} - \dfrac{\Delta t}{2}\nabla V(q^{n+1}) - \dfrac{\Delta t}{2}\gamma(q^{n+1})M^{-1}p^{n+1} + \sqrt{\dfrac{\Delta t}{2}}\sigma(q^{n+1})G^{n+1/2}. \end{cases}$$

$(G^0, G^{1/2}, G^1, G^{3/2}, \ldots)$ denote a sequence of i.i.d. Gaussian random vectors with zero mean and covariance Id.

We add one or more atoms to the system at regular time intervals at prescribed locations on the substrate surface in the proximity of the catalyst. Early on in the simulation, the addition locations line up well with vacancies in the bottom edge of the nanotube, and the new atoms incorporate into the hexagonal lattice of the sidewalls,

eventually pushing the tube upward. Later on, the new atoms do not line up well with the vacancies, and the new carbon atoms do not always incorporate into the hexagonal lattice of the sidewalls. See Figures 2.5 and 2.6 for snapshots from MD simulations at two different temperatures. We discover that there are many local minima of the potential corresponding to different bond arrangements. As a result, annealing is required for the tube to grow upward. This requires very long simulations to see even a small amount of CNT growth. The presence of many local minima makes it difficult to analyze the system by transition state theory, as this requires identification of all local minima and saddle points in the energy landscape. The complicated form of the potential, which involves many parameters, also makes analysis difficult. To allow more experimentation and analysis, we investigate a much simplified one-dimensional model that preserves some aspects of the full three-dimensional model.
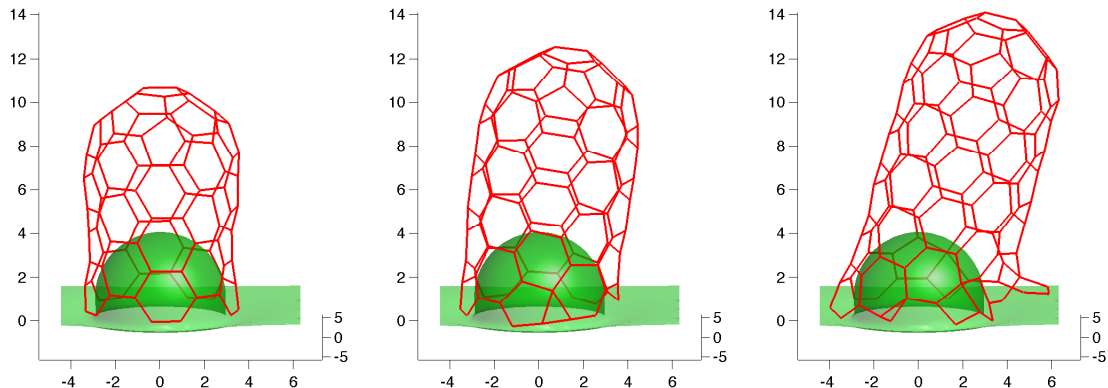
Figure 2.5: Results from MD simulations of the 3-D model at a low temperature. Carbon-carbon bonds are shown in red and a level set of the effective catalyst/substrate potential is shown in green. Initially, there are 90 atoms in the nanotube structure, and two new atoms are added after every 0.1 nanosecond. (*left*) After 0.1 nanosecond. (*center*) After 1 nanosecond. (*right*) After 2 nanoseconds.
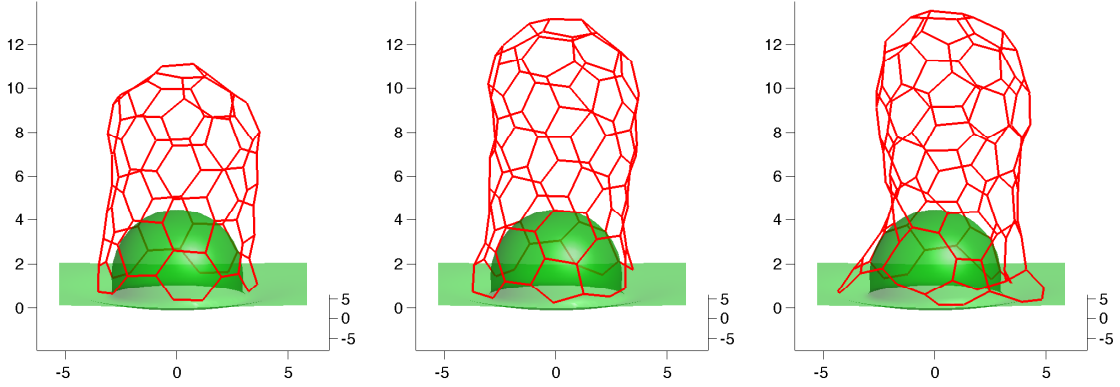
Figure 2.6: Results from MD simulations of the 3-D model at a high temperature. (*left*) After 0.1 nanosecond. (*center*) After 1 nanosecond. (*right*) After 2 nanoseconds.

2.2 Simplified one-dimensional model

In our one-dimensional model, a chain of atoms is connected by Hooke's law springs with spring constant k and equilibrium length r. There is also an external potential consisting of a barrier and a well, the height and width of which is controlled by the parameters a and b, respectively (see Figure 2.7). The configuration of the system is given by the coordinates $\{q_i\}_{i=1}^N$, which we assume to be ordered $q_1 < q_2 < \ldots < q_{N-1} < q_N$. The energy of the system is

$$(2.18) \qquad V(q_1, \ldots, q_N) = \sum_{i=1}^{N} -2ab \operatorname{sech}^2(bq_i) \tanh(bq_i) + \sum_{i=2}^{N} \frac{1}{2} k(q_i - q_{i-1} - r)^2.$$

If the external potential is not present (i.e. $a = 0$), then the system has a single energy minimum with translation invariance: a chain of atoms with all bonds at the equilibrium length r. The interaction between the external potential and bonds within the chain creates energy minima, including one with much lower energy than the others. These energy minima are separated by saddle points in the energy landscape.

We use this system to represent a growing carbon nanotube. The atoms left of the barrier represent carbon atoms that are on the substrate, the atom in the well
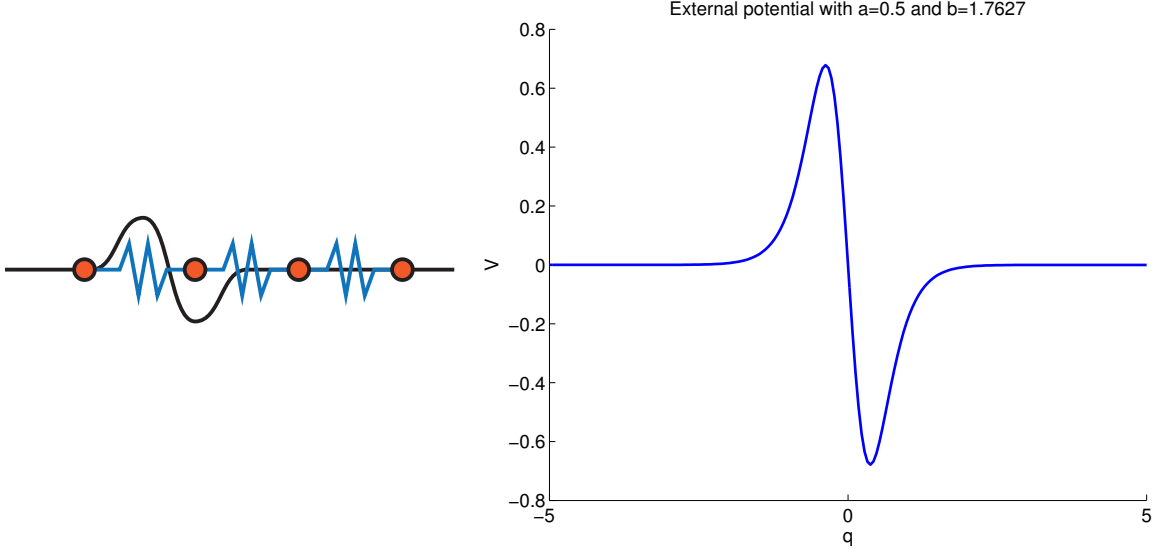
Figure 2.7: (*left*) Schematic of a chain of atoms connected by springs, interacting with an external potential. (*right*) External potential with $a = 0.5$ and $b = 1.7627$.

represents a carbon atom that is attached to the catalyst, and the atoms right of the well represent carbon atoms that have detached from the catalyst to form a carbon nanotube. Thus, there is a correspondence between fully extended chains in the one-dimensional model and defect-free configurations in the CNT growth model where all carbon atoms have incorporated into the sidewall of the nanotube. Likewise, there is a correspondence between configurations in the one-dimensional model that are not fully extended and configurations in the CNT growth model where some carbon atoms are on the substrate. See Figure 2.8.

The barrier in the external potential corresponds to the energetic cost for carbon atoms to rearrange their bonds and incorporate into the nanotube. This is similar to the barrier for carbon incorporation described in [90]. The well in the external potential is analogous to the bond between the carbon atom and the catalyst. An interesting question is whether a local change in energy from the barrier to the well can drive the growth of a large structure, since the entire structure needs to be perturbed to accommodate the newly incorporated atom. This can be studied by analysis and

CNT Growth

Defect-free

Defect-free   Defected

1-D Analogue

Fully extended

Fully extended   Not fully extended
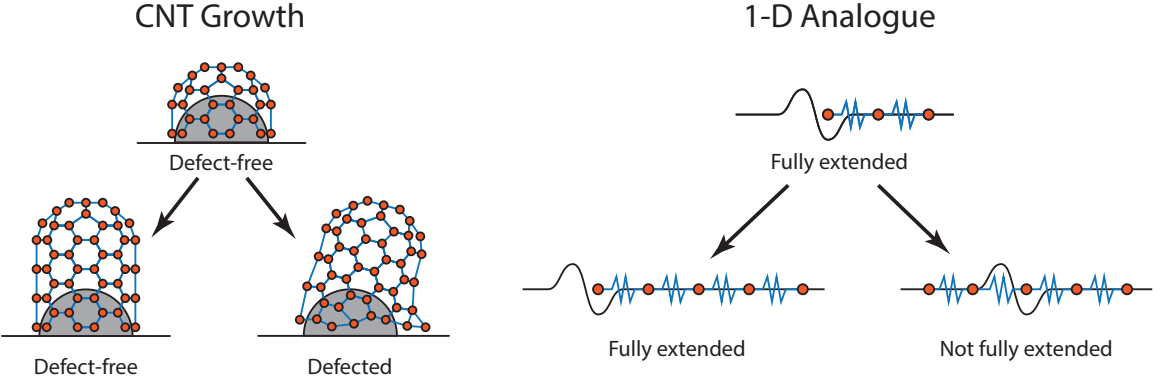
Figure 2.8: Schematic showing the analogy between the CNT growth model and the one-dimensional model. The arrows represent the growth of a defect-free (fully extended) configuration to either another defect-free (fully extended) configuration or a defected (not fully extended) configuration.

simulation of the one-dimensional model.

2.2.1 Fixed numbers of atoms

2.2.1.1 Energy landscape and thermodynamics

First we consider a chain with a fixed number of atoms. If we further suppose that all bonds in the chain have a fixed length, then the system only has one degree of freedom, which we can take to be q_1, the coordinate of the leftmost atom in the chain. We can think of this constraint as being enforced when $k \to \infty$ in (2.18). For a chain with three atoms, the potential and corresponding Boltzmann-Gibbs distribution[2] at $\beta = 10$ are shown in Figure 2.9. We see that there are three local minima, one of which has much lower energy than the other two. The probability of a system being in the lowest energy state is much larger than the probability of being in the other two minima. As the temperature is decreased, this lowest energy state becomes more and more probable.

For a chain of N atoms with a finite spring constant k, the energy depends on N

---

[2]A confining potential is necessary to make the Boltzmann-Gibbs distribution integrable. For instance, one can consider a quadratic increase in the potential outside of a large box around the origin.
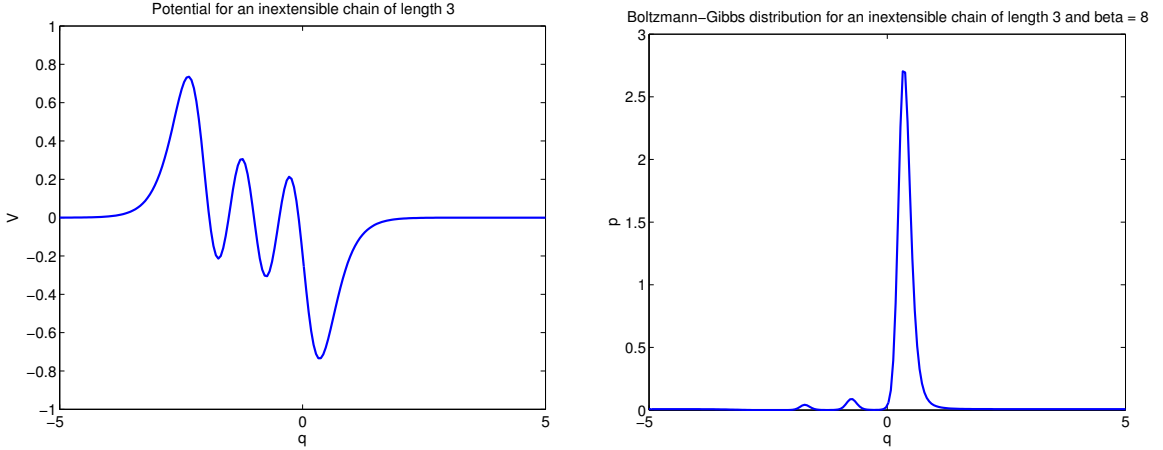
Figure 2.9: (*left*) Effective potential for a chain of three atoms with fixed bond lengths. (*right*) The Boltzmann-Gibbs distribution corresponding to this potential energy for $\beta = 8$.

variables. We can still plot these energies for chains with 2 or 3 atoms. In Figure 2.10, we plot isocontours of the energy for a two-atom chain with $k = 5$. We see that there are two local minima. Starting with the local minima and maxima of the $k = \infty$ energy, we can locate the local minima and saddle points of the $k = 5$ energy by numerically solving $\nabla V = 0$. In Figure 2.11, we plot the $V = -0.15$ isosurface of the energy for a chain of three atoms. We see that this surface consists of three connected components, which lie within three different basins of attraction. If we perform MD simulations of a system of length 3, we can see that the trajectories are usually in one of the potential basins, with some transitions between the basins. See the right of Figure 2.11. The configurations of the chain at the three local minima, which we call "states," are shown in Figure 2.12.

2.2.1.2   Transition rates

We can calculate the transition rates between the basins of attraction using transition state theory (TST). A good reference is [37]; a more mathematical perspective can be found in [80, 76]. In this theory, the transition between two locally stable
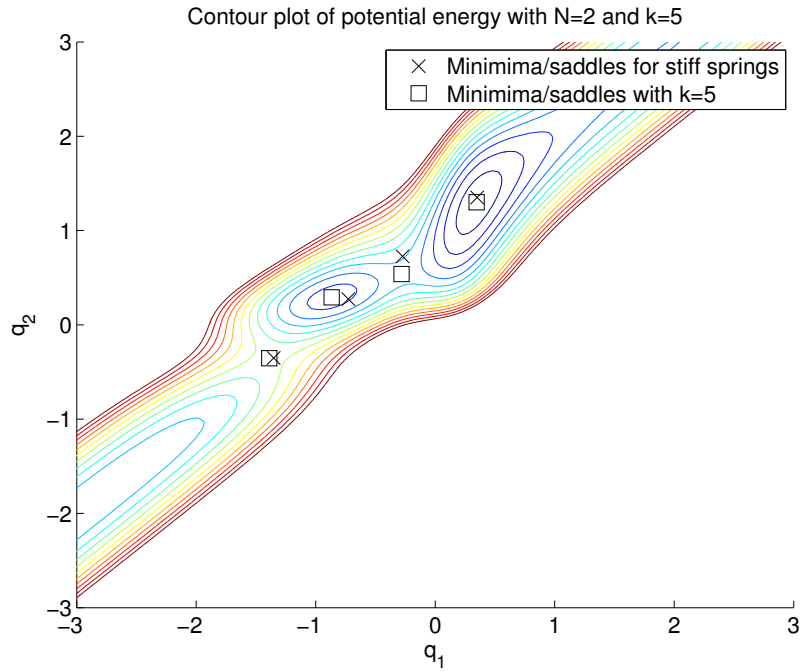
Figure 2.10: Potential for a chain with two atoms.
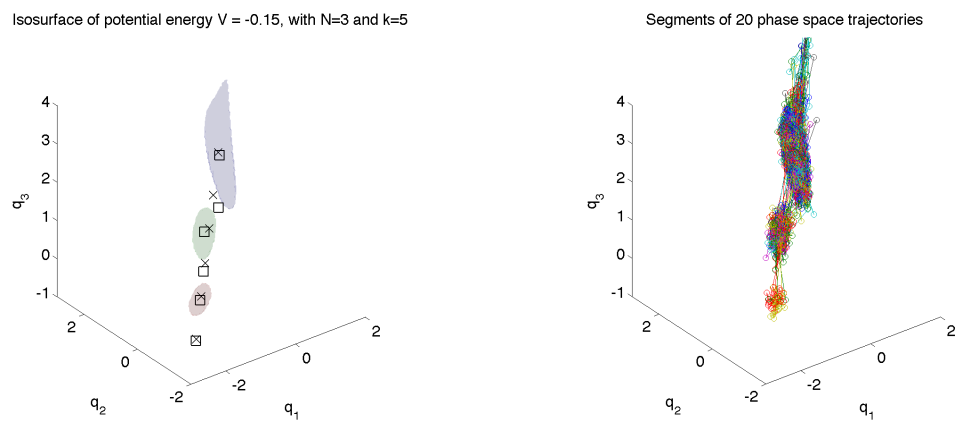
Figure 2.11: (*left*) Isosurfaces of the potential for a chain with three atoms. (*right*) Trajectories of several MD simulations of chains of three atoms.
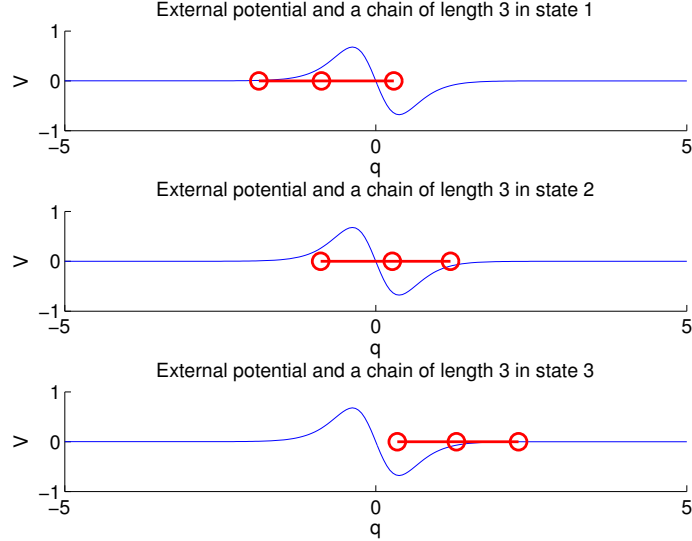
Figure 2.12: Chains corresponding to the local minima of the energy.

states, called the reactant state and the product state, is described by a reaction co-ordinate. The reaction coordinate $x(q)$ is defined in such a way that it is positive in the basin of attraction corresponding to the reactant state and negative in the basin corresponding to the product state. $x = 0$ defines the dividing surface between the reactant state and the product state. Points on the dividing surface correspond to transition states. TST is based on two assumptions:

1. Thermodynamic equilibrium holds for all degrees of freedom in the system.

2. Any orbit crossing the dividing surface will not recross it. This is valid when the energy of thermal fluctuations is much less than the the energy barrier height of transition events.

We define the function $\theta(x)$ to be 1 for $x > 0$ and 0 for $x < 0$. The TST rate is then [37]:

(2.19)
$$k_{\mathrm{TST}}^{+} = \frac{\langle \delta[x(0)]\dot{x}(0)\theta[\dot{x}(0)]\rangle}{\langle \theta(x)\rangle}.$$

This is the equilibrium average of the one-way flux at the transition state, normalized by the equilibrium population of the reactant state.

First, we calculate rates for a chain with inextensible springs. The other parameters are selected as $a = 0.5$, $b = 1.7627$, $r = 1$, and $\beta = 10, 12$, or 14. We locate the local maxima and minima for the potential, which depends on only a single variable. The local maxima divide $\mathbb{R}$ into intervals of attraction. We consider the three states pictured in Figure 2.11, and calculate the transition rates between them. The momentum part of (2.19) is $(2\pi\beta)^{-1/2}$, which comes from the integral of the Maxwell-Boltzmann distribution. The configuration part of the numerator is $\exp(-\beta V(q_s))$, where q_s is the position of the saddle point. The configuration part of the denominator is $\int_{q_1}^{q_2} \exp(-\beta V(q)) \, dq$, where q_1 and q_2 are the left and right endpoints of the interval, respectively. We can ignore the normalizing factor of the probability density since it cancels in (2.19). Thus, we have

$$(2.20) \qquad k_{\text{TST}}^+ = (2\pi\beta)^{-1/2} \frac{\exp(-\beta V(q_s))}{\int_{q_1}^{q_2} \exp(-\beta V(q)) \, dq}.$$

The TST rates for chains with inextensible bonds are shown in the $k = \infty$ column of Table 2.1 for $\beta = 10$, Table 2.2 for $\beta = 12$, and Table 2.3 for $\beta = 14$. Note that as β increases (i.e. temperature decreases) the transition rates decrease.

We can calculate transition rates when the spring constant is finite as well. We locate the minima and saddle points by numerically solving $\nabla V = 0$ using the locations of the minima and maxima from the $k = \infty$ case as an initial guess. We locate the basins of attraction by finding the connected components of the set $\{q \in \mathbb{R}^N : V(q) < -0.15\}$. These are not the full basins of attraction, but the probability density function $\exp(-\beta V(q))$ will be relatively small outside these regions. We then integrate $\exp(-\beta V(q))$ over each of these regions to determine the equilibrium population of each basin. We approximate the dividing surfaces between basins as

Rate	$k = \infty$, theory	$k = 5$, theory	$k = 5$, simulation	Ratio, simulation to theory
r_{12}	2.88×10^{-3}	3.10×10^{-3}	$1.90 \pm 0.05 \times 10^{-3}$	0.61 ± 0.02
r_{21}	1.08×10^{-3}	9.16×10^{-4}	$6.2 \pm 0.2 \times 10^{-4}$	0.68 ± 0.02
r_{23}	2.77×10^{-3}	3.25×10^{-3}	$2.37 \pm 0.03 \times 10^{-3}$	0.729 ± 0.009
r_{32}	3.22×10^{-5}	6.85×10^{-5}	$5.48 \pm 0.07 \times 10^{-5}$	0.80 ± 0.01

Table 2.1: Transition rates for a chain of three atoms, with inverse temperature $\beta = 10$.

Rate	$k = \infty$, theory	$k = 5$, theory	$k = 5$, simulation	Ratio, simulation to theory
r_{12}	1.03×10^{-3}	1.07×10^{-3}	$7.4 \pm 0.5 \times 10^{-4}$	0.69 ± 0.05
r_{21}	3.18×10^{-4}	2.72×10^{-4}	$1.9 \pm 0.1 \times 10^{-4}$	0.71 ± 0.04
r_{23}	9.88×10^{-4}	1.19×10^{-3}	$9.3 \pm 0.3 \times 10^{-4}$	0.78 ± 0.02
r_{32}	4.92×10^{-6}	1.30×10^{-5}	$1.05 \pm 0.05 \times 10^{-5}$	0.81 ± 0.04

Table 2.2: Transition rates for a chain of three atoms, with inverse temperature $\beta = 12$.

planes that pass through the saddle point. These planes are chosen to be normal to the eigenvector of the Hessian of the energy at the saddle point that corresponds to the negative eigenvalue. We numerically calculate the integral over a portion of this plane corresponding to the largest probability. If S denotes the dividing surface and Ω denotes the basin, then the rate is

$$(2.21) \qquad k_{\text{TST}}^+ = (2\pi\beta)^{-1/2} \frac{\int_S \exp(-\beta V(q)) \, dA}{\int_\Omega \exp(-\beta V(q)) \, dq}.$$

The rates calculated in this way for $k = 5$ are shown in Tables 2.1, 2.2, and 2.3. These tables also show transition rates calculated from an MD simulation with Langevin dynamics using the same parameter values. The ratios between the simulation values and the theoretical values are shown as well. Considering that transition state theory gives an upper bound on the transition rates, there is good agreement between the theory and the numerical simulations.

Rate	$k = \infty$, theory	$k = 5$, theory	$k = 5$, simulation	Ratio, simulation to theory
r_{12}	3.64×10^{-4}	3.77×10^{-4}	$3.2 \pm 0.9 \times 10^{-4}$	0.8 ± 0.2
r_{21}	9.36×10^{-5}	8.24×10^{-5}	$7 \pm 2 \times 10^{-5}$	0.8 ± 0.2
r_{23}	3.51×10^{-4}	4.41×10^{-4}	$3.5 \pm 0.4 \times 10^{-4}$	0.80 ± 0.08
r_{32}	7.45×10^{-7}	2.45×10^{-6}	$2.0 \pm 0.1 \times 10^{-6}$	0.81 ± 0.06

Table 2.3: Transition rates for a chain of three atoms, with inverse temperature $\beta = 14$.

For chains with more atoms, we can still locate the local minima and the saddle points. However, it becomes difficult to resolve the basins of attraction on a discretized grid. We can instead make a harmonic approximation of the potentials around the local minima and saddle points. With this approximation, the probability density function becomes a Gaussian function, which we integrate over N-dimensional space for the basins of attraction and $(N-1)$-dimensional space for the dividing surfaces. This requires calculating the eigenvalues and eigenvectors of the Hessian of the potential at these points. The eigenvalues at the saddle point q_s are denoted $\{\lambda_i^s\}$ with λ_N^s negative, all other eigenvalues positive. The eigenvalues at the minimum q_0 are denoted $\{\lambda_i^0\}$. The formula for the TST rate in this case is:

$$(2.22) \qquad k_{\text{TST}}^+ \approx (2\pi\beta)^{-1/2} \frac{\exp(-\beta V(q_s))(2\pi/\beta)^{(N-1)/2} \prod_{i=1}^{N-1}(\lambda_i^s)^{-1/2}}{\exp(-\beta V(q_0))(2\pi/\beta)^{N/2} \prod_{i=1}^{N}(\lambda_i^0)^{-1/2}}$$

$$(2.23) \qquad = (2\pi)^{-1} \exp(-\beta(V(q_s) - V(q_0))) \frac{\prod_{i=1}^{N}(\lambda_i^0)^{1/2}}{\prod_{i=1}^{N-1}(\lambda_i^s)^{1/2}}$$

The accuracy of this approximation improves at lower temperatures (greater β). This form for the rate also makes it clear that the transition rates depend on the inverse temperature β and the local properties of the potential at the minimum and the saddle point (i.e. the potential value and the eigenvalues of its Hessian). Using this approximation for chains with $k = 5$, $\beta = 10$, and $4 \leq N \leq 18$, we find that the transition rates do not depend on the length of the chain. This occurs

because the potential and its Hessian is the same at the corresponding minima and the corresponding saddle points, regardless of N. The forward rates are

$$(2.24) \qquad r_{12} = 0.3772 \exp(-0.5013\beta),$$

$$(2.25) \qquad r_{i,i+1} \approx 0.3238 \exp(-0.5556\beta) \text{ for } 2 \leq i \leq N - 2, \text{ and}$$

$$(2.26) \qquad r_{N-1,N} = 0.4086 \exp(-0.4896\beta).$$

The backward rates are

$$(2.27) \qquad r_{21} = 0.3241 \exp(-0.5839\beta),$$

$$(2.28) \qquad r_{i+1,i} \approx 0.3238 \exp(-0.5556\beta) \text{ for } 2 \leq i \leq N - 2, \text{ and}$$

$$(2.29) \qquad r_{N,N-1} = 0.3192 \exp(-0.8368\beta).$$

For $\beta = 10$, these values are $r_{12} = 2.5 \times 10^{-3}$, $r_{i,i+1} \approx 1.3 \times 10^{-3}$ for $2 \leq i \leq N-2$, and $r_{N-1,N} = 3.1 \times 10^{-3}$ for the forward rates, and $r_{21} = 9.4 \times 10^{-4}$, $r_{i+1,i} \approx 1.3 \times 10^{-3}$ for $2 \leq i \leq N - 2$, and $r_{N,N-1} = 7.4 \times 10^{-5}$ for the backward rates.

2.2.2 Growing chains

We perform non-equilibrium MD simulations of this model, in which new atoms are added one bond length away from the left end of an existing chain at a specified rate. We initialize with chains of 10 atoms, 9 of which are right of the barrier. Thus, one atom must move to the right of the barrier before the system is in its lowest energy state. This represents a CNT where one carbon atom has not yet incorporated into the nanotube sidewall.

To determine which state the system is in, we can calculate how many atoms in the chain are right of the barrier. In Figure 2.13, this quantity is plotted against time for 10 different MD simulations with overdamped Langevin dynamics. Normalized

histograms for 1000 MD simulations are shown in Figure 2.14. These give the empirical probability of different states at different times. We observe that, initially, it is very likely for the system to shift to the right to its lowest energy state, where all N atoms are right of the barrier. As more atoms are added, it becomes less and less likely for the system to be in its lowest energy, fully extended state. The decay in this probability is faster for fast addition rates and slower for slower addition rates, as can be seen in Figure 2.14.
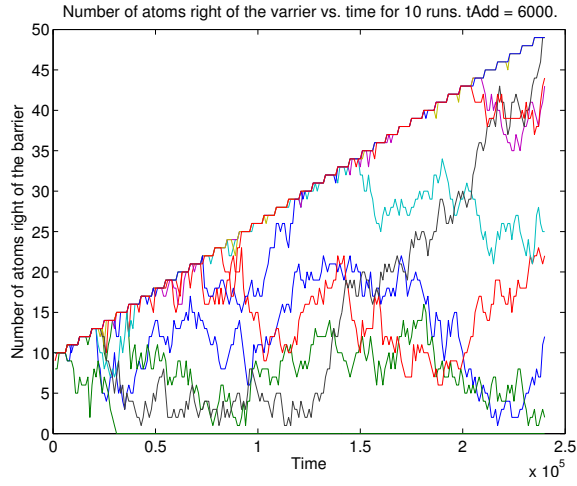
Figure 2.13: The number of atoms right of the barrier for 10 different MD simulations. The parameters are $a = 0.5$, $b = 1.7627$, $r = 1$, $k = 5$, and $\beta = 10$. New atoms are added every 6000 time units.

We can analyze these results using statistical mechanics and transition state theory. Between additions, the system behaves like a chain with a fixed number of atoms. Thus, we can use our analysis above to determine the different local energy minima of the system, the probability distribution of these states, and the transition rates between them. The transition rates can be used to create a continuous-time Markov chain model for our system. For a reference on Markov chains, see [63]. The state space for the system is $I = \{1, \ldots, N\}$. The generator matrix Q for the Markov chain
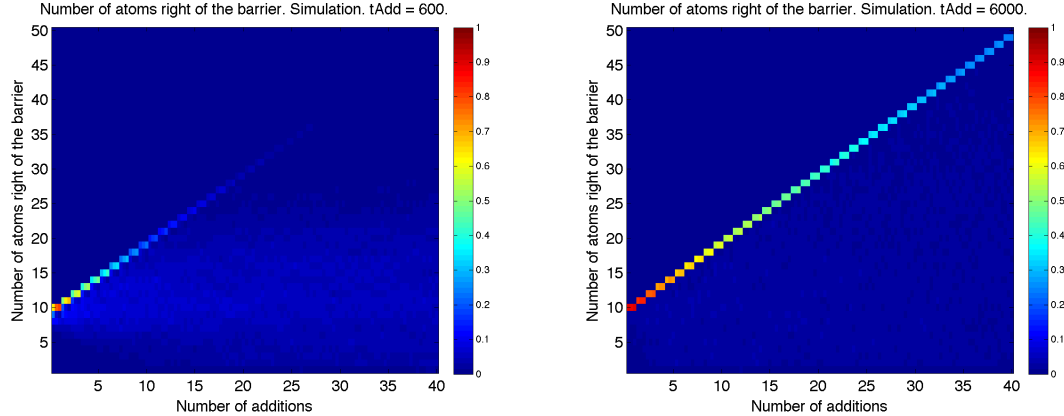
Figure 2.14: Normalized histograms of chain extension from 1000 MD simulations at different times, shown as a number of atom additions. The bright diagonal line corresponds to a peak in the probability at the lowest energy state. (*left*) Atom added every 600 time units. (*right*) Atom added every 6000 time units.

is constructed as follows. For $j \neq i$, the rate of going from state i to state j is

$$(2.30) \qquad\qquad q_{ij} = r_{ij}.$$

This defines the off-diagonal elements of Q. The rate of leaving state i is

$$(2.31) \qquad\qquad q_i := \sum_{j \neq i} q_{ij}.$$

The diagonal elements of Q are defined as $q_{ii} = -q_i$.

The transition matrix $P(t)$ is the solution of the forward equation:

$$(2.32) \qquad\qquad \frac{\mathrm{d}}{\mathrm{d}t} P(t) = P(t)Q, \quad P(0) = I.$$

The entries $p_{ij}(t)$ give the probability of transition from state i to state j in time t.

Now, define the vector-valued function $x(t)$ such that $x_i(t)$ is the probability that the system is in state i at time t. The initial probability distribution is $x(0) = x_0$.

The probability distribution x can be written in terms of the transition matrix as

$$(2.33) \qquad x(t)^T = x_0^T P(t).$$

We have

$$(2.34) \qquad \frac{\mathrm{d}}{\mathrm{d}t} x(t)^T = x_0^T \frac{\mathrm{d}}{\mathrm{d}t} P(t) = x_0^T P(t) Q = x(t)^T Q,$$

or

$$(2.35) \qquad \frac{\mathrm{d}}{\mathrm{d}t} x(t) = Q^T x(t).$$

Defining $A := Q^T$, we rewrite this equation, called the master equation, as

$$(2.36) \qquad \frac{\mathrm{d}}{\mathrm{d}t} x(t) = Ax(t), \quad x(0) = x_0.$$

We can calculate the matrix A using the TST transition rates. For a chain of length N with $k = 5$ and $\beta = 10$, the matrix A is the $N \times N$ matrix

$$(2.37) \qquad A_N = (1.3 \times 10^{-3}) \times \begin{bmatrix} -1.9 & 0.72 & & & & & & \\ 1.9 & -1.7 & 1 & & & & & \\ & 1 & -2 & 1 & & & & \\ & & \ddots & \ddots & \ddots & & & \\ & & & 1 & -2 & 1 & & \\ & & & & 1 & -3.4 & 0.057 \\ & & & & & 2.4 & -0.057 \end{bmatrix}.$$

If we begin with a system of N_0 atoms and add one atom at the end of each time interval of length t_{Add}, up to a total of N_{max} atoms, then we have a sequence of Markov

60

chain models. This is illustrated for $N_0 = 1$ and $N_{max} = 3$ in Figure 2.15. This sequence of models can be represented by a time-dependent system matrix $A(t) = A_{N_0 + \lfloor t/t_{Add} \rfloor}$, which is constant on time intervals of length t_{Add}. To model the system over a time interval $[0, N_{max} t_{Add}]$, a $N_{max} \times N_{max}$ matrix can be used, which is padded with zeros for transition rates to and from the inaccessible states.
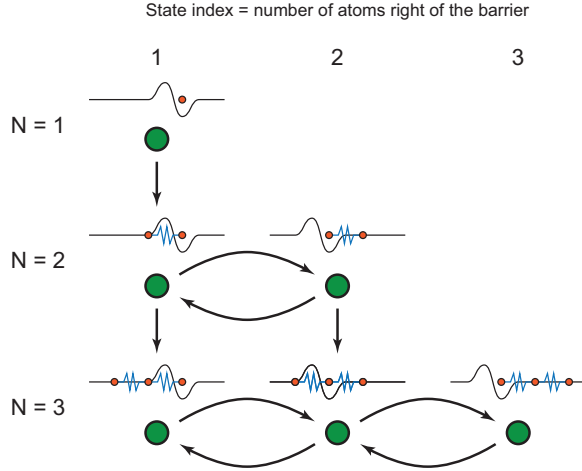
Figure 2.15: Illustration of a sequence of Markov models representing a growing chain. The system is initialized with a single atom and two atom additions are shown. The green circles represent the states, and the small diagrams represent the corresponding configurations. The vertical arrows represent atom additions, and the horizontal arrows represent transitions between states.

To compare with the empirical probabilities calculated from the simulations, we choose $N_0 = 10$, $x_i(0) = \delta_{i,9}$. We also multiply the matrix A_N above by a transmission coefficient of 0.7, chosen based on the ratio of the transition rates in the simulation to the theoretical transition rates for $\beta = 10$ in Table 2.1. We numerically calculate the solution of the master equation using the forward Euler method. The solutions are in good qualitative agreement with the growth simulations. Compare the solution of the master equation in Figure 2.16 to the empirical probability from the growth simulations in Figure 2.14.
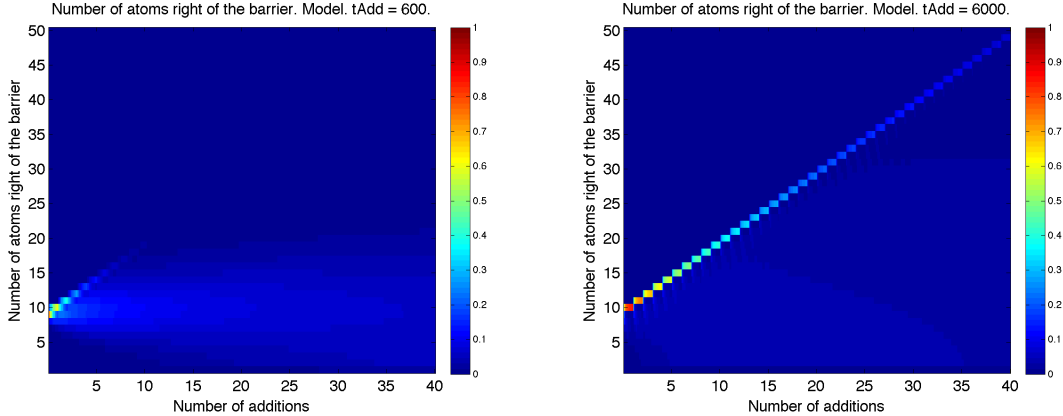
Figure 2.16: Probabilities of different chain lengths calculated with the master equation. The bright diagonal line corresponds to a peak in the probability at the lowest energy state. (*left*) Atom added every 600 time units. (*right*) Atom added every 6000 time units.

2.3 Analysis of the master equation

Let $A = S\Lambda S^{-1}$ be a diagonalization of the matrix A in the master equation (2.36). Then the solution of the master equation is

$$(2.38) \qquad x(t) = \exp(tA)x_0 = \sum_{j=1}^{N} [S^{-1}x_0]_j e^{\lambda_j t} s_j.$$

This solution can be used to determine the time required to evolve from a given initial condition to within a small tolerance of equilibrium. We sort the eigenvalues in decreasing order. There is always a single zero eigenvalue and the other eigenvalues are negative, so $\lambda_1 = 0$ and λ_2 is the negative eigenvalue with the smallest magnitude. Thus, we can write the solution as

$$(2.39) \qquad x(t) = \exp(tA)x_0 = [S^{-1}x_0]_1 s_1 + [S^{-1}x_0]_2 e^{\lambda_2 t} s_2 + \sum_{j=3}^{N} [S^{-1}x_0]_j e^{\lambda_j t} s_j.$$

The first term is the equilibrium solution. As $t \to \infty$, we have $x(t) \to [S^{-1}x_0]_1 s_1$. The deviation of the probabilities from their asymptotic value is then:

$$(2.40) \qquad x(t) - [S^{-1}x_0]_1 s_1 = [S^{-1}x_0]_2 e^{\lambda_2 t} s_2 + \sum_{j=3}^{N} [S^{-1}x_0]_j e^{\lambda_j t} s_j.$$

The first term will dominate the sum for large values of t. Thus, the eigenvalue λ_2 and the coefficient $[S^{-1}x_0]_2$ will determine when the solution is within a small tolerance of the equilibrium distribution.

The rate matrix can be made symmetric by a similarity transformation. If $D = \text{diag}(x_\infty^{1/2})$, then $B = D^{-1}AD$ is symmetric. It may sometimes be helpful to consider this form of the rate matrix, since the eigenvectors are then orthogonal.

2.3.1 Rate matrix calculated from the energy landscape

Using the master equation, we can calculate the probability that a growing chain is in its lowest energy state, both as a function of the addition rate and the number of additions, for different values of β. We initialize the master equation with 10-atom chains with all 10 atoms right of the barrier. For fast addition rates, the probability drops to zero very quickly as more atoms are added. For slow addition rates, the probability reaches its equilibrium value, which also decreases as more atoms are added, but much more slowly. See Figure 2.17. The different lines in each figure correspond to different numbers of additions. The greater the number of additions, the lower the probability of the lowest energy state, because the equilibrium probability of the lowest energy state decreases as the length of the chain increases. There is a region of addition rates where a transition occurs between these two behaviors. For high temperature (low β), this transition occurs for relatively fast addition rates (e.g. $r_{add} = 1 \times 10^{-3}$ when $\beta = 5$). For low temperatures (high β), this transition occurs at very slow addition rates (e.g. $r_{add} = 1 \times 10^{-7}$ when $\beta = 20$). This is because changing

the temperature decreases the fast transition rates in the system and also decreases the ratio of the slow transition rate to the fast transition rates.

At higher temperatures for the first few atom additions, there is a "sweet spot" for the addition rate where the probability of full rightward extension has a local maximum. This is caused by initializing with 10-atom chains, all having all 10 atoms right of the barrier. This initially biases the probability distribution toward states with most atoms right of the barrier. Initializing from the equilibrium distribution or from a very short chain would cause the probability of the lowest energy state to decrease monotonically with the addition rate.

The probability distribution of the states after 40 atom additions will depend on the addition rate. The distributions for four different rates at $\beta = 15$ are shown in Figure 2.18. For slow addition rates, the probability distribution is the equilibrium distribution, with the probability concentrated in state 41, the lowest energy state. For fast addition rates, the probability is concentrated in state 1, where there is only one atom right of the barrier. For intermediate rates, the probability is largest for state 2, but then decreases down to 0 for state 41.

These probability distributions can be used as initial conditions for the time evolution of the distribution after addition of a new atom. To get a lower bound for the transitional addition rate, the initial probability distribution $x_i(0)$, $i = 1, \ldots, N - 1$ is set to the equilibrium distribution for a chain of $N - 1$ atoms and $x_N(0) = 0$. The time required for $x_N(t)$ to reach 99.9% of its equilibrium value for the N-atom chain is then measured. The inverse of these times give the transitional addition rate. These are the circles plotted in the upper left of Figure 2.19. To get an upper bound on the transitional addition rate, the probability distribution is initialized to be $x_1(0) = 0$, $x_i(0) = c(N - 1 - i)$ for $2 \leq i \leq N - 1$, and $x_N(0) = 0$, where c is a normalization constant. Thus, there is a linear decrease in the probability from state 2 to state $N - 1$. This seems to be a decent approximation of the probability

64
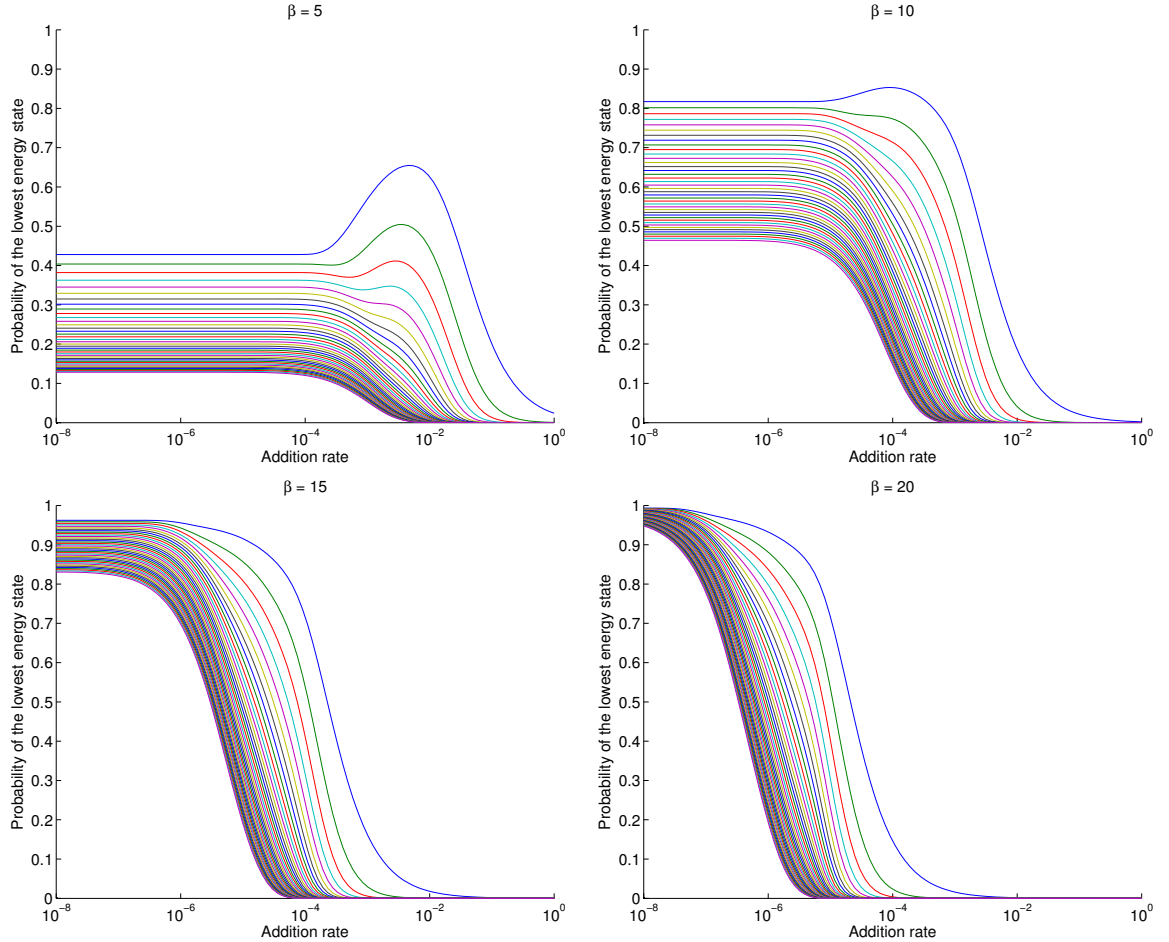
Figure 2.17: Probability of the lowest energy state for different addition rates, temperatures, and number of additions. Different curves correspond to different numbers of additions. Different figures are for different temperatures: (*from left to right, top to bottom*) $\beta = 5$, $\beta = 10$, $\beta = 15$, $\beta = 20$. Note that the x-axis (addition rate) has a logarithmic scaling.
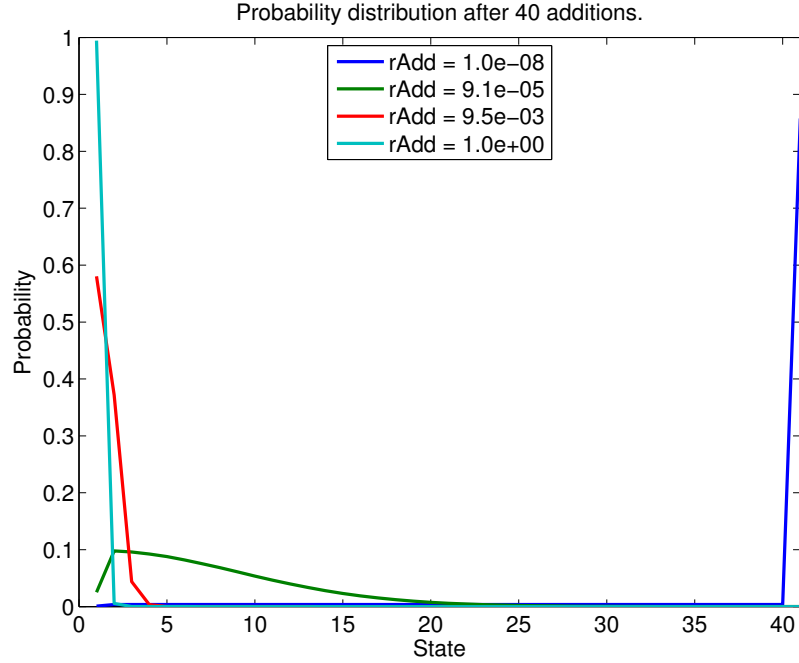
Figure 2.18: Probability distribution after 40 additions at different addition rates: $r_{add} = 1.0 \times 10^{-8}$, $r_{add} = 9.1 \times 10^{-5}$, $r_{add} = 9.5 \times 10^{-3}$, and $r_{add} = 1.0$.

distribution for the addition rates at the upper bound of the transition region. From this initialization, the time required for $P_N(t)$ to reach 0.1% of its equilibrium value is calculated. This seems to give a good upper bound on the addition rates in the transition region. These are the circles plotted in the lower right of the figure.

2.3.2 Approximate rate matrix with two parameters

Assume that there are only two different transition rates in the system. The transition rate from state N to state $N - 1$ is r_s, and all other transition rates are $r_f \gg r_s$. This is a good approximation for the rate matrix calculated from the energy landscape. For $k = 5$ and general β, we select $r_s = 0.3192 \exp(-0.8368\beta)$ and $r_f = 0.3238 \exp(-0.5556\beta)$. For $\beta = 10$, this is $r_s = 7.4 \times 10^{-5}$ and $r_f = 1.3 \times 10^{-3}$.
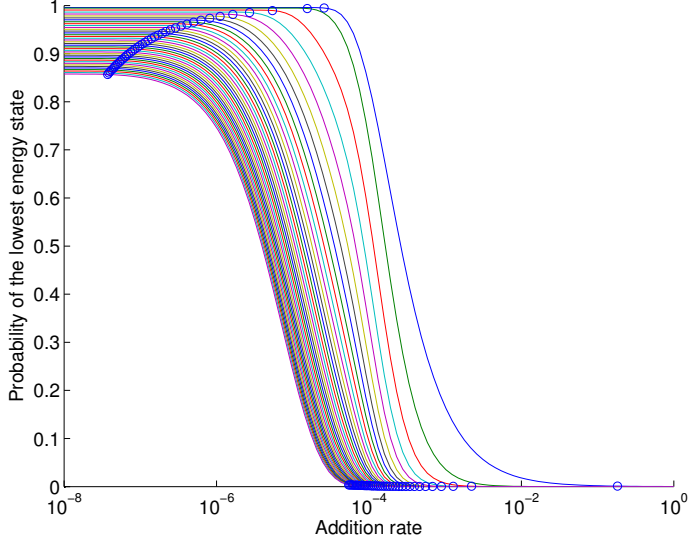
Figure 2.19: Probability of the lowest energy state for different addition rates and number of additions at $\beta = 15$. The blue circles are approximate bounds for the transition region.

The approximation of the $N \times N$ matrix A_N is

$$(2.41) \qquad A_N \approx (1.3 \times 10^{-3}) \times \begin{bmatrix} -1 & 1 & & & & & \\ 1 & -2 & 1 & & & & \\ & 1 & -2 & 1 & & & \\ & & \ddots & \ddots & \ddots & & \\ & & & 1 & -2 & 1 & \\ & & & & 1 & -2 & 0.057 \\ & & & & & 1 & -0.057 \end{bmatrix}.$$

Without loss of generality, we will consider $r_f = 1$ in our analysis. (If $r_f \neq 1$, rescale time.) Then, the approximate rate matrix can be written as

67

$$(2.42) \qquad A = \begin{bmatrix} -1 & 1 & & & & & \\ 1 & -2 & 1 & & & & \\ & 1 & -2 & 1 & & & \\ & & \ddots & \ddots & \ddots & & \\ & & & 1 & -2 & 1 & \\ & & & & 1 & -2 & r_s \\ & & & & & 1 & -r_s \end{bmatrix}$$

2.3.2.1   Equilibrium distribution

The normalized equilibrium distribution for this matrix is

$$(2.43) \qquad [x_\infty]_i = \begin{cases} \frac{r_s}{1+r_s(N-1)} & \text{for } i = 1, \ldots, N-1 \\[2ex] \frac{1}{1+r_s(N-1)} & \text{for } i = N. \end{cases}$$

This is also the eigenvector corresponding to the zero eigenvalue. Note that the ground state is r_s^{-1} times more likely than any other state. However, the probability of any state decays to zero like N^{-1} as $N \to \infty$.

2.3.2.2   Hitting times

We can calculate expected hitting times for this model using Markov chain theory. In general, if Q is the generator matrix for the Markov chain, then the expected hitting times k_i^A for the state A are the minimal non-negative solution to the system of linear equations [63]

$$(2.44) \qquad \begin{cases} k_i^A = 0 & \text{for } i \in A \\[2ex] -\sum_{j \in I} q_{ij} k_j^A = 1 & \text{for } i \notin A. \end{cases}$$

For the two-parameter rate matrix, the expected time it takes to reach state N from state j is $[(N^2 - N)/2 - (j^2 - j)/2]$, which is independent of r_s and has a maximum of $(N^2 - N)/2$, attained for state $j = 1$. The expected time it takes to reach state j from state N is $((N - j)^2 - (N - j))/2 + (N - j)r_s^{-1}$. If r_s is small, this is dominated by the $(N - j)r_s^{-1}$ term.

2.3.2.3 Eigenvalues and eigenvectors

The matrix A can be considered as a perturbation of a matrix A_0 that is very similar to the discrete Laplacian:

$$
(2.45) \qquad A =
\begin{bmatrix}
-1 & 1 & & & & & \\
1 & -2 & 1 & & & & \\
 & 1 & -2 & 1 & & & \\
 & & \ddots & \ddots & \ddots & & \\
 & & & 1 & -2 & 1 & \\
 & & & & 1 & -2 & 0 \\
 & & & & & 1 & 0
\end{bmatrix}
+ r_s
\begin{bmatrix}
 & & & & & & \\
 & & & & & & \\
 & & & & & & \\
 & & & & & & \\
 & & & & & & \\
 & & & & & 0 & 1 \\
 & & & & & 0 & -1
\end{bmatrix}
$$

One can use perturbation theory to approximate the eigenvalues of the system matrix. For a reference on the perturbation theory of unsymmetric eigenvalue problems, see [35, section 7.2]. Besides the zero eigenvalue, this matrix has the unperturbed eigenvalues, for $1 \leq i \leq N - 1$,

$$
(2.46) \qquad \lambda_i^0 = 2 \left[\cos\left(\pi \left(i - \frac{1}{2} \right) \Big/ \left(N - \frac{1}{2} \right) \right) - 1 \right].
$$

The unperturbed eigenvectors, for $1 \leq i \leq N - 1$, are

(2.47)

$$[x_i^0]_j = \begin{cases} \left(\frac{N}{2} - \frac{1}{4}\right)^{-1/2} \cos\left[\pi\left(j - \frac{1}{2}\right)\left(i - \frac{1}{2}\right)/\left(N - \frac{1}{2}\right)\right] & \text{for } 1 \leq j \leq N - 1 \\ \left(\frac{N}{2} - \frac{1}{4}\right)^{-1/2}(\lambda_i^0)^{-1}\cos\left[\pi\left(N - \frac{3}{2}\right)\left(i - \frac{1}{2}\right)/\left(N - \frac{1}{2}\right)\right] & \text{for } j = N \end{cases}$$

The perturbed eigenvalues are, for $1 \leq i \leq N - 1$:

(2.48) $$\lambda_i = \lambda_i^0 + \frac{\cos^2[\pi(N - \frac{3}{2})(i - \frac{1}{2})/(N - \frac{1}{2})]}{\left(\frac{N}{2} - \frac{1}{4}\right)\lambda_i^0}r_s + O(r_s^2).$$

The perturbed eigenvectors are, for $1 \leq i \leq N - 1$:

(2.49)

$$x_i = x_i^0 + \sum_{\substack{j=1 \\ j \neq i}}^{N-1} \frac{\cos[\pi(N - \frac{3}{2})(i - \frac{1}{2})/(N - \frac{1}{2})]\cos[\pi(N - \frac{3}{2})(j - \frac{1}{2})/(N - \frac{1}{2})]}{\left(\frac{N}{2} - \frac{1}{4}\right)\lambda_i^0(\lambda_i^0 - \lambda_j^0)}r_s x_j^0$$

$$+ O(r_s^2).$$

The unperturbed and linearized perturbed eigenvalues are shown in Figure 2.20 with $N = 20$ and $r_s = 1$. A large value of r_s is used only to show the trend for the perturbed eigenvalues; the linearization is only accurate for small values of r_s.

For a plot of the non-zero eigenvalue with the smallest magnitude, see Figure 2.21. The approximate expression above is plotted as a surface and the actual eigenvalues are plotted as blue circles. There are plots with linear scales and with logarithmic scales. When r_s is small, the approximation is quite good. When r_s is not too small, the actual eigenvalues have magnitude smaller than the approximations.

2.3.2.4   Initial value problem for the probabilities

Starting with initial conditions that are delta distributions for different states, we look at the evolution of the probability distribution as well as its first moment
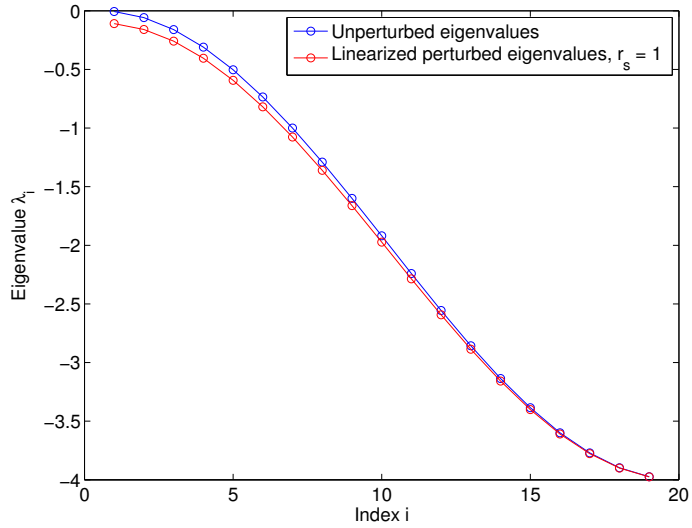
Figure 2.20: The unperturbed (blue) and linearized perturbed (red) eigenvalues with $N = 20$ and $r_s = 1$.
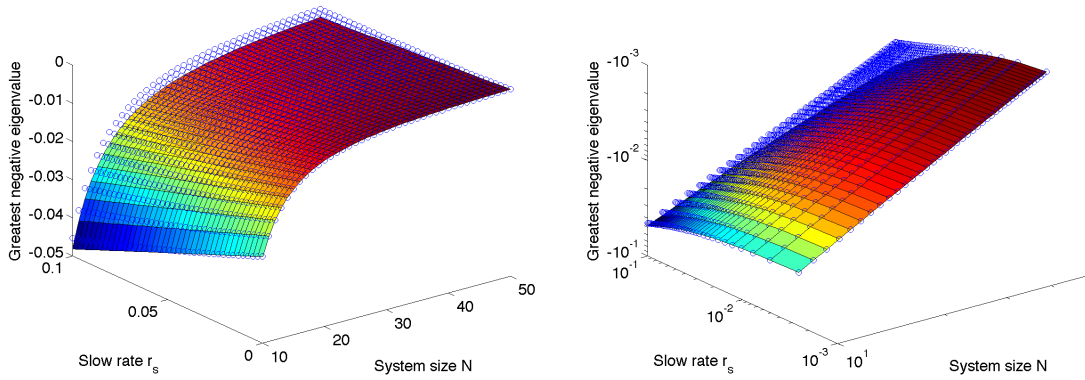
Figure 2.21: The non-zero eigenvalue with the smallest magnitude, plotted against system size and the value of r_s. (*left*) With linear axis scaling. (*right*) With logarithmic axis scaling.

(the average extension of the chain). These examples are for a chain of length 40, which has 40 states. The parameter values are $r_s = 1.0 \times 10^{-6}$ and $r_f = 1.0 \times 10^{-4}$. There are plots for initial conditions concentrated in states 1 (most atoms left of the barrier), 20 (half of the atoms on the left, half on the right), and 39 and 40 (most atoms right of the barrier).

The plots in Figure 2.22 show the probability of different states. The three circles on each plot show the last times that the probability of the lowest energy state reaches a probability 0.1%, 50%, and 99.9% between the initial value and the final value (or 100.1% if the probability overshoots the equilibrium value and then returns to it). These are meant to show a fast time scale, intermediate time scale, and slow time scale for the evolution of the distribution. The plots in Figure 2.23 show the average extension. The three circles are calculated in the same way using the average extension values. These time scales are plotted for all initial states in Figure 2.25. Notice that on this logarithmically-scaled plot, the slow time scales are relatively flat in both cases. The correlation of the initial conditions with the eigenmodes of the symmetrized system matrix are plotted in Figure 2.24. These determine the coefficients of the different eigenmodes in the evolution of the probability.

2.3.2.5 Growth efficiency

We define the growth efficiency as the ratio of the average rightward shift to the number of atoms added. These are plotted as functions of addition rate in Figure 2.26. Different curves on the same plot show the efficiency after different numbers of additions. For a fixed addition rate, as atoms are added, growth becomes less and less efficient. I have used the simplified rate matrix, where all transition rates are $r_f = 1 \times 10^{-4}$, except for the transition rate from state N to state $N - 1$, which has rate r_s. I show plots for different values of r_s. This parameter affects the maximum growth efficiency. It does not seem to have a large effect on the time scales of
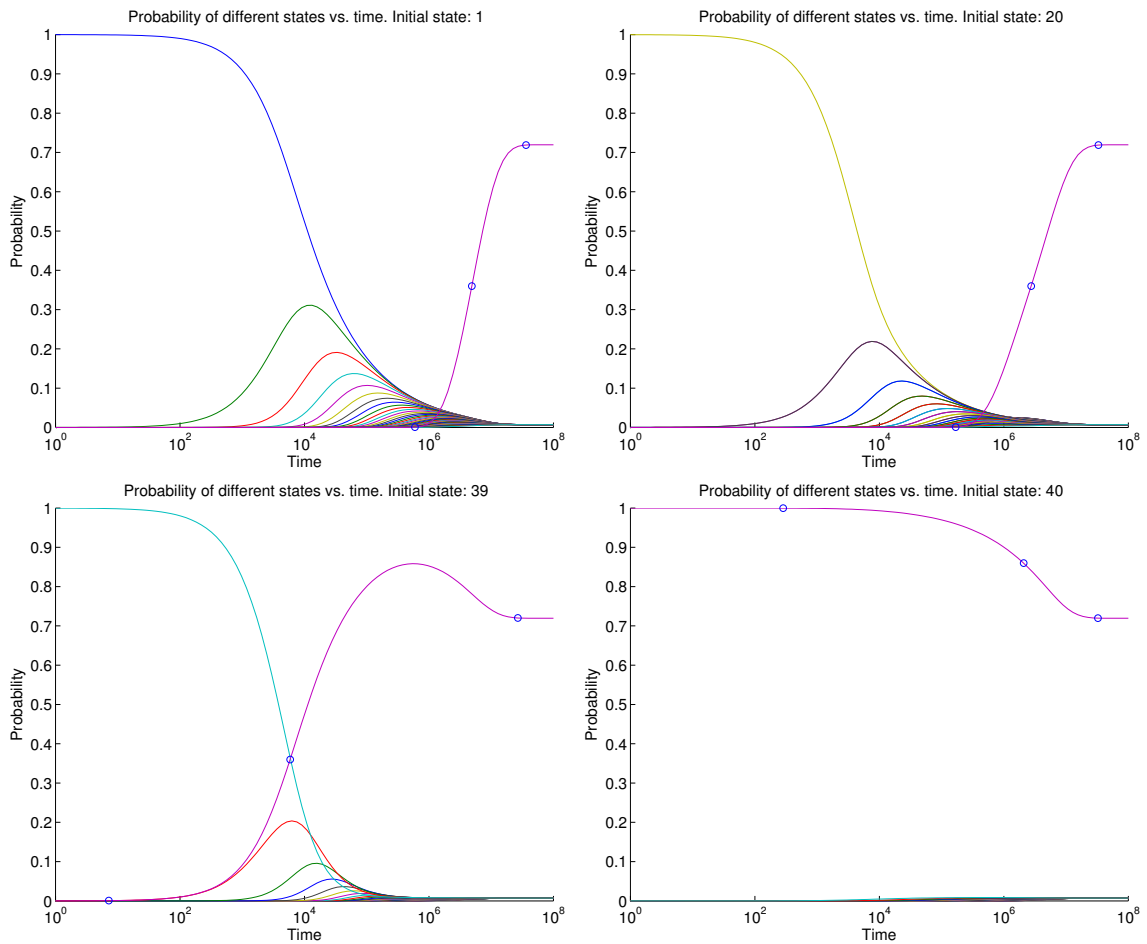
Figure 2.22: Evolution of the probability distribution starting from a single state. (*from left to right, top to bottom*) State 1, state 20, state 39, state 40.
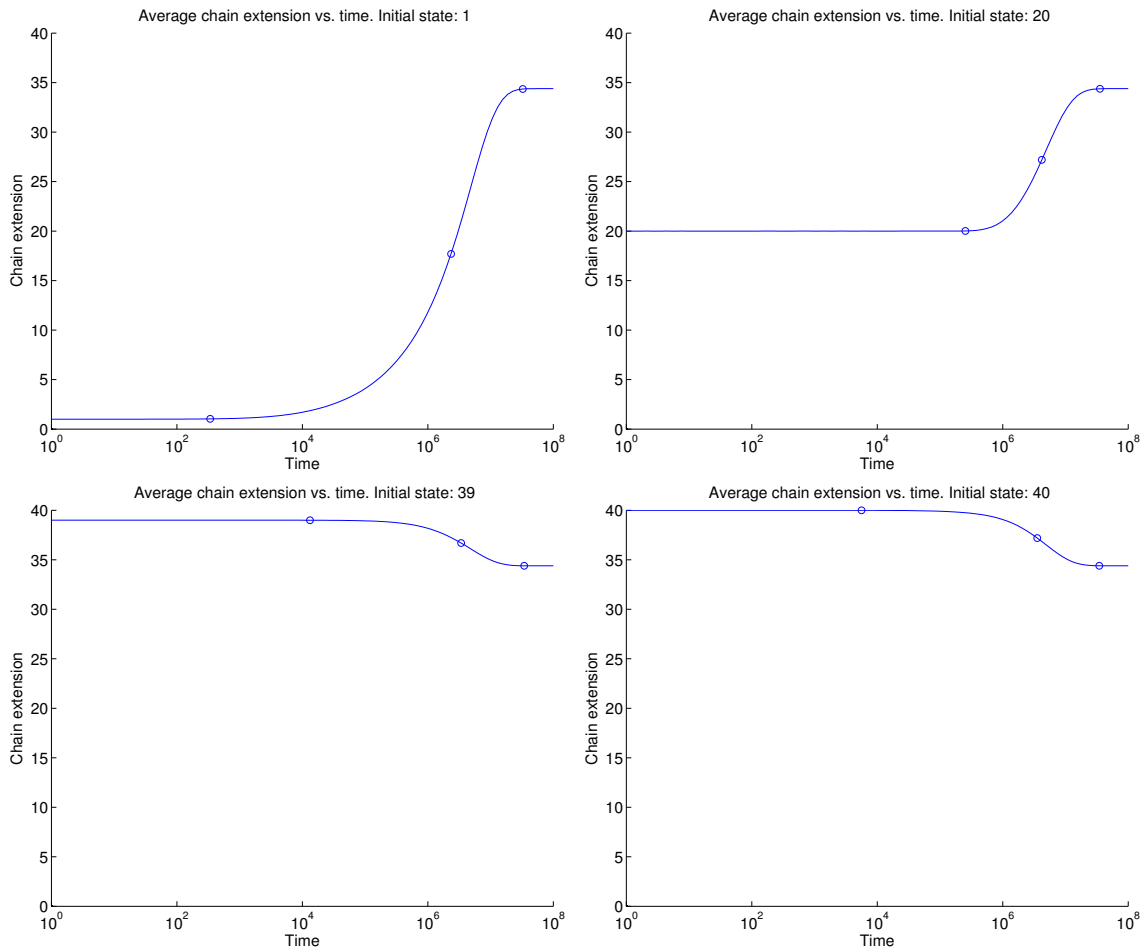
Figure 2.23: Evolution of the average extension starting from a single state. (*from left to right, top to bottom*) State 1, state 20, state 39, state 40.
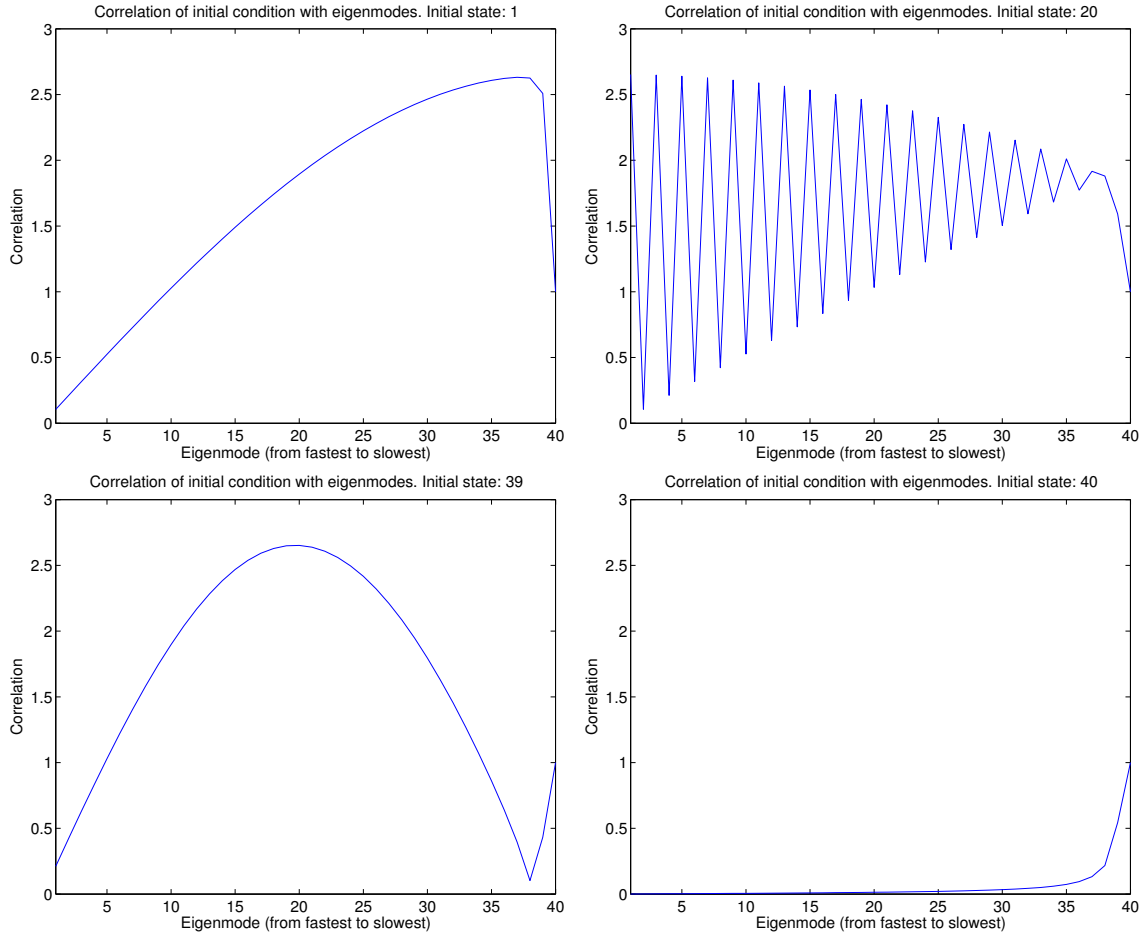
Figure 2.24: Correlation of the initial condition with the eigenmodes of the symmetrized system matrix. The eigenmodes are sorted from fastest (most negative) to slowest (least negative). (*from left to right, top to bottom*) State 1, state 20, state 39, state 40.
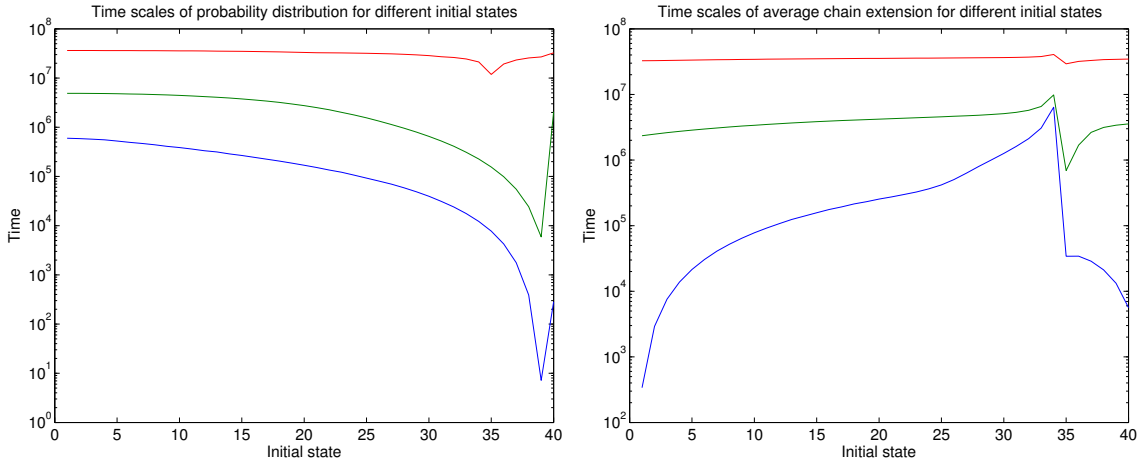
Figure 2.25: Time scales for (*left*) the probability of the lowest energy state and (*right*) the average chain extension, beginning from different states.

the problem, i.e. there is no addition rate at which the growth efficiency jumps up, regardless of the value of r_s.

2.3.2.6 Summary

If atoms are added slowly enough, the distribution of extensions for an ensemble of growing chains will become very close to the equilibrium distribution between additions. Suppose one wanted to grow fully extended 40-atom chains with at least 90% yield. Then there exists a maximum temperature for which the yield (i.e. equilibrium probability) exceeds this threshold. If one specifies a temperature at or below the maximum, there exists a maximum addition rate (i.e. a minimum growth time) for which the specified yield is achieved. The maximum addition rate to achieve this yield would be related to λ_2, the non-zero eigenvalue with the least magnitude, as this controls the rate of convergence to the equilibrium at large times. If one wanted longer chains with the same yield, the maximum allowable temperature would decrease, as would the maximum allowable addition rate. This is related to the decay in the equilibrium probability and the eigenvalue λ_2 as N increases.
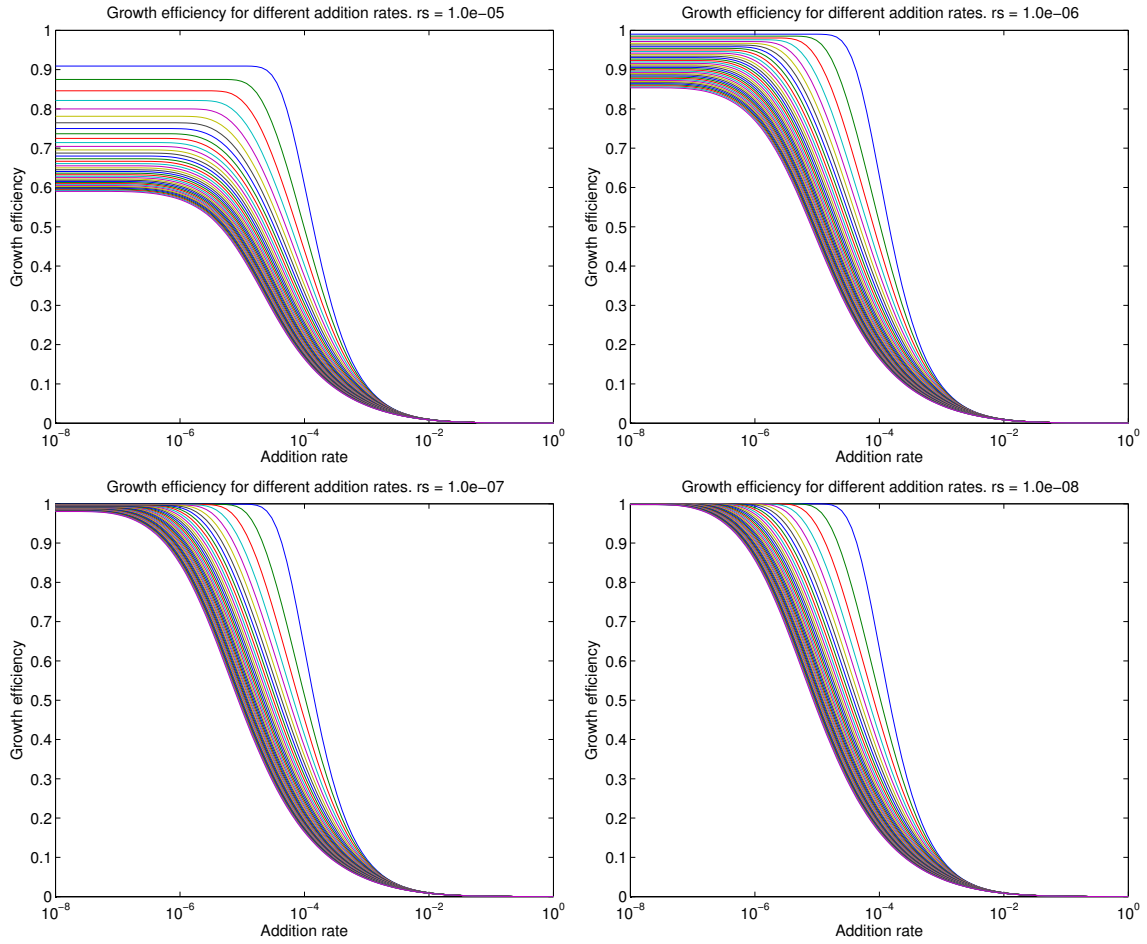
Figure 2.26: Growth efficiency when $r_f = 1 \times 10^{-4}$ and r_s has the following values: (*from left to right, top to bottom*) $r_s = 1.0 \times 10^{-5}$, $r_s = 1.0 \times 10^{-6}$, $r_s = 1.0 \times 10^{-7}$, and $r_s = 1.0 \times 10^{-8}$.

2.4 Conclusions

In this chapter, we have described an atomistic model for the catalytic growth of an individual nanotube. The substrate and catalyst are treated as static continua, and the carbon atoms are mobile. We used this model to simulate the continued growth of a nanotube structure, but found that the system gets stuck in local minima as atoms continue to be added. Instead of incorporating into the sidewall of the nanotube and pushing it up, the newly added atoms remain bonded to the substrate. To better understand the limitations of this model, we analyzed a simple one-dimensional model of a chain structure acted on by an external potential. The chain structure with internal bonding and no external potential has a single energy minimum with translation invariance. The interaction between the external potential (representing the catalyst) and bonds within the chain (representing the CNT) creates energy minima, including one with much lower energy than the others. These energy minima are separated by saddle points in the energy landscape.

The ground state has much higher equilibrium probability than the other states, although this probability decreases as the number of atoms increases. This occurs because we consider a system where the energy of the ground state differs from the energy of all other states by a constant. The situation might be different for a funneled landscape, where the non-optimal states have increasing energies as one moves away from the ground state in configuration space.

The probability of full extension will decrease as atoms are added at a fixed rate. For slow addition rates, this probability initially decays with the equilibrium probability distribution, but it will eventually decay much faster as the system size grows. Although the slow and fast transition rates within the system do not change significantly as the number of atoms increases, the spectrum of the matrix in the master equation does change, slowing the rate of convergence to the equilibrium distribution as the size of the system increases. As a result, the probability distribution will move

further and further from the equilibrium distribution, with the ground state having a relatively low probability.

Fully extended chains in the one-dimensional model correspond to defect-free nanotubes in the full atomistic model of CNT growth. These are the ground states of their respective systems.[3] The probability of the ground state represents the growth quality for the given system. The requirement of a slow addition rate for high quality growth in the one-dimensional model highlights the difficulty in the MD simulations of our model of CNT growth. In order to simulate in a reasonable amount of computer time, one must use a fast addition rate. Such an addition rate does not provide time for the system to sample the equilibrium distribution. As a result, as atoms are added, the system will have a low probability of being in the ground state, even if the system is initially in the ground state. Thus, there is a higher probability of carbon nanotubes with defected sidewalls than of nanotubes with defect-free sidewalls.

This analysis suggests that in order to grow CNTs with the highest probability of being defect-free, one should use a lower temperature and a slower carbon addition rate. However, for actual growth, there may be a lower bound for the growth temperature, as one must consider factors such as the decomposition of the feedstock and the phase of the catalyst particle. Also, there may be a practical lower bound on the addition rate as well, as one would like to grow nanotubes of length 100 μm or more in about 1 hour or less. Further work should be done to find growth conditions which optimize the growth quality of CNTs.

---

[3]This is known for the one-dimensional model and conjectured for the the full CNT growth model.

CHAPTER III

Modeling the chemically coupled growth of carbon nanotube microstructures[1]

3.1 Introduction

Beyond the properties of individual CNTs and the applications of bulk CNT powders [25], a new frontier of applications is potentially accessible by harnessing the properties of large numbers of CNTs in organized assemblies. In academic research, vertically aligned CNT "forests" have been incorporated into different material systems including thin films, interface layers, and structured 3D geometries such as micropillars or coatings on woven fibers. The individual CNT properties as well as the hierarchical morphology of CNT forests gives rise to novel and widely tunable mechanical behavior [41, 56], as well as electrical transport [84, 77] and thermal transport properties that can be related to the CNT alignment and contact behavior [17, 89]. Nevertheless, uniformity in the geometry, density, and diameter of the CNTs within the forest is needed to effectively engineer functional properties.

In several published reports as well as in our own previous work, it is apparent that typical CVD growth conditions for CNT forests create significant spatial

---

[1]Significant portions of this chapter are reproduced from [12] M. Bedewy*, B. Farmer*, and A. J. Hart. Synergetic chemical coupling controls the uniformity of carbon nanotube microstructure growth. *ACS Nano*, 8(6):5799–5812, 2014. *M. Bedewy and B. Farmer contributed equally.

non-uniformities. These include geometric non-uniformities (i.e., sloped heights) of macroscopic CNT forests [38, 36], as well as microscopic CNT pillars [81, 82, 43].

A typical CNT micropillar array from our work exemplifies these variations. Micropillars grown to high aspect ratios (30 minutes growth time, Figure 3.1a) strikingly curve outward along the periphery of the array. Micropillars with much lower aspect ratio (3 minutes growth time, Figure 3.1b, c, d) are shorter toward the edges and corner of the array, and the corner catalyst pattern feature does not yield a CNT forest. In addition, the micropillars near the corner of the array do not completely cover the catalyst pattern, and have crowned top surfaces. Moreover, we frequently observe that the growth of smaller diameter micropillars can be enhanced (i.e., made taller and more uniform) by the presence of larger diameter micropillars or adjacent non-patterned catalyst substrates placed in the CVD furnace to enhance growth.

These results imply that growth of CNTs is influenced by proximity effects of nearby CNTs and/or catalytically active surfaces that can influence the CVD environment. Recently, Parker et al. showed that placement of thin catalyst micropatterns adjacent to larger patterns influenced the smaller patterns to produce horizontally oriented CNT structures that bent away from the larger patterns [66]. Earlier, Borgstrom et al. demonstrated synergetic effects in Gallium Phosphide (GaP) nanowire growth, owing to both gas-phase and surface diffusion interactions influenced by the proximity and diameter of the individual nanowires [18].

For CNT growth by CVD, Bronikowski suggested that growth-promoting byproducts are generated during decomposition of the feedstock gas in areas of high catalyst concentration [22]. Jeong et al. proposed that the variation of local partial pressures of carbon-containing active gaseous precursors causes such catalyst proximity effects that lead to spatial variations in CNT forest height [43]. In addition, the curvature of the top surface of CNT micropillars has been attributed to the mechanical constraint of the tangled "crust" of the forest, coupled with spatial and temporal evolution of the
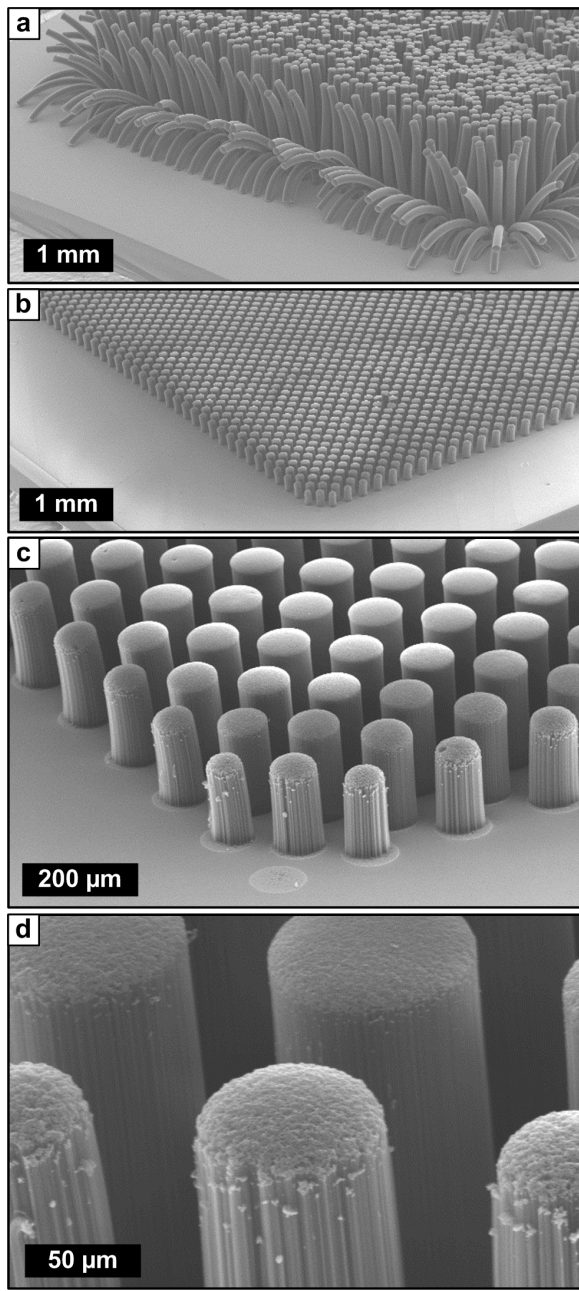
Figure 3.1: Non-uniformities in the geometry and dimensions of cylindrical CNT forest micropillars (100 μm diameter, 100 μm spacing in a square lattice). (a) Outward bending of peripheral micropillars in a large array, after growth time of 30 minutes. (b, c, d) Variations of height, diameter, and top surface geometry among CNT micropillars grown for only 3 minutes, under the same conditions as (a). Also note in (c) that the corner catalyst microfeature does not produce a CNT forest. This area has tangled CNTs which fail to "lift off" into a forest. The same is observed around the perimeters of the micropillars along the edge of the array.

CNT growth rate [36]. Nevertheless, there is not a quantitative understanding of how and why catalyst proximity influences CNT growth. Reaching such an understanding is difficult due to the multi-component nature of the CNT growth atmosphere, and the existence of multiple chemical species having varying potency for promoting and/or deactivating the growth process.

During a typical CVD process for CNT growth, the hydrocarbon feedstock gas and byproducts of its gas-phase reactions [57, 67, 68] catalytically decomposes at the surface of the catalyst nanoparticles producing active species that promote the CNT growth process. Literature abounds with studies aiming at determining the activity of different carbon-containing species [45]. For instance, acetylene [32], or alkynes in general [68], and polycyclic aromatic hydrocarbons (PAHs) [61] have all been identified as key active molecules in the CVD growth of CNTs. The efficiency of different hydrocarbon precursors is likely dependent on temperature, pressure, humidity, or the cooperative effects among multiple hydrocarbon precursors. It has also been proposed that polyaromatic intermediate fragments first form on the surface of the support layer in the vicinity of the catalyst before getting incorporated into the growing CNT [54]. These complex mechanisms are not fully understood, but they strongly suggest that chemical coupling is a fundamental aspect of CNT growth, and the cooperation of multiple chemical species with one another, the substrate, and the catalyst, influence the growth rate and perfection of CNTs.

Therefore, to enable the manufacturing of uniform CNT forests and microstructures, we believe that a mathematical model is needed to describe the chemical process that involves local reactions at the nanoscale catalyst sites, and their diffusion-induced coupling among the growing patterned structures at the microscale. Process uniformity is also a paramount issue in semiconductor manufacturing, and further analogies can be drawn for example to thickness variations in chemical-mechanical polishing [75], or the local variations of plasma etch rates [1]. In these cases, mathematical

models of the coupling phenomenon have facilitated design of patterns and process conditions to improve uniformity.

We present a hierarchical framework for modeling chemically coupled CNT growth, wherein a growth model for an individual CNT is modified to account for diffusion-induced spatial variations of growth behavior among arrays of CNT micropillars in proximity. We first model the spatial distribution of active species, which are generated at catalyst sites and diffuse to the surroundings. Owing to the autocatalytic nature of growth [46, 16], the activation energy of CNT growth is inversely related to the concentration of these active species, leading to a spatial correlation between concentration of active species and the modulation of CNT growth rates. Through simulations and experiments, we predict spatial variations according to pattern size and spacing, and we use these results to elucidate the successive stages of CNT micropillar lift-off in arrays. We demonstrate that this model can be used to design the CNT micropillar spacing and/or size in an array in order to enhance uniformity, in spite of collective chemical effects.

3.2 Methodologies

3.2.1 Mathematical modeling

We developed a mathematical model of the synergetic growth of CNTs on a planar substrate. This model calculates the spatial distribution of active species that are locally produced at the catalyst surface, and then diffuse to the surroundings (Figure 3.2a). Our approach is justified based on the knowledge that thermal and catalytic reactions involving the feedstock gas ethylene (C_2H_4) mixed with H_2 and He, produce a variety of hydrocarbon species [57], many of which contribute to the CNT growth process. It is most likely that a combination of gases, in addition to short-lived radicals, contribute to CNT growth. The reaction kinetics certainly de-

pend on the temperature and pressure, and the catalyst nanoparticle composition, size, and shape.

To maintain generality, we collectively identify this combination of CNT growth precursors as "active species", without specifying a specific hydrocarbon molecule or radical. The spatially varying concentration of these active species is utilized as a quantitative measure of chemical coupling, as it modulates the CNT growth rate by shifting the apparent activation energy of CNT growth. The diffusion of these active species over the CNT growth substrate results in a time-varying spatial distribution of concentration (Figure 3.2b), which supplements the nominal concentration of feedstock provided by the CVD system. The net concentration of active species, in combination with the other growth conditions, determines the CNT growth rate locally at each time step, enabling time-resolved simulations of the height evolution of the patterned CNT forest.

To model the chemical coupling between growing CNT micropillars we combine a model of gas diffusion to a widely accepted model of CNT growth from a catalyst particle, which was developed by Puretzky et al. [69]. Moreover, our synergetic growth framework (Figure 3.2c) is, in principle, compatible with any model of CNT growth that has a quantitative formulation of activation energy. Puretzky et al. model CNT growth as a sequence of physical and chemical steps: the chemisorption and catalytic decomposition of feedstock gas, the dissolution and diffusion of carbon on the nanoparticle surface, and finally, the precipitation of carbon atoms into a growing CNT at the CNT-catalyst interface (Figure 3.2a). We model the spread of the chemical byproducts using a gas diffusion equation, and hence calculate the time-evolving spatial distribution of their concentration. Each micron-scale catalyst area acts as a time-varying source of these active species, the kinetics of which is coupled to growth deactivation kinetics.

Recent research on CNT growth, especially for single-walled CNTs, has revealed
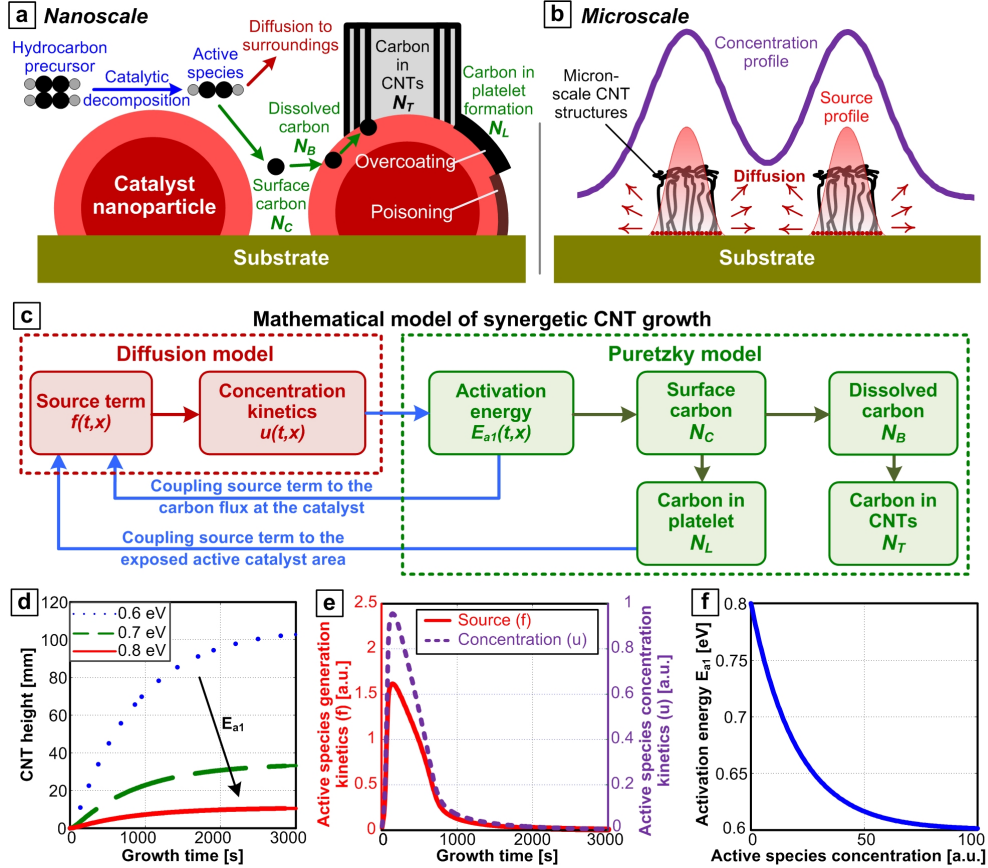
Figure 3.2: Model of synergetic CNT growth from the nanoscale to the microscale: (a) Schematic of the physical and chemical steps that lead to individual CNT growth from a catalyst nanoparticle on a substrate (adapted from Puretzky et al. [69]). (b) Schematic showing the diffusion-driven profile of active species, which is generated from the byproducts of the CNT growth reaction at the catalyst. (c) Block diagram of the chemically coupled synergetic CNT growth model, with feedback between the nominal CNT growth process and the diffusion of catalyst-generated active species. (d) Time evolution of height for a 10 nm diameter CNT with different activation energies E_{a1}, without chemical coupling. (e) Kinetics of the source term and the ensuing concentration increase on the catalyst region, according to Equations (3.9)-(3.12). The spatial step size is $\Delta x = 0.004$ mm and the time step is $\Delta t = 7.5$ s. (f) The dependence of activation energy (E_{a1}) on the concentration of active species (u).

more detailed mechanisms including the dynamic restructuring of nanoparticles during growth [58], and correlating the nucleation of CNT walls to both the phase [85] and lattice steps on the catalyst nanoparticle surface [40]. Moreover, the influence of chirality on both screw-dislocation-driven rotation of CNTs [28] and growth rate [70] was recently studied. Nevertheless, the Puretzky model is still generally applicable to growth of multi-walled CNTs by carbon diffusion and precipitation, and reflects a general chemical process that is applicable to CNT growth without regard to diameter or chirality.

In our framework, the Puretzky model is first used to calculate the growth rate of an individual CNT. In this model, growth occurs from a metal catalyst nanoparticle (Figure 3.2a), which is surrounded by carbon-containing gas feedstock as well as the products of thermal decomposition of the feedstock. These hydrocarbons catalytically decompose on the catalyst surface to atomic carbon and/or bonded carbon. The surface carbon then dissolves into a molten/disordered layer of the catalyst and precipitates, forming the growing CNT. In addition, some products of gas pyrolysis directly contribute to the formation of a carbonaceous platelet layer on the catalyst surface. Eventually, this platelet completely covers the catalyst nanoparticle causing complete cessation of growth. The surface carbon can also incorporate into the carbonaceous layer, and the carbonaceous layer can dissolve into the molten layer.

The number of carbon atoms on the surface of the catalyst is denoted N_C; the number of carbon atoms in a poisoned layer (N_{L2}) or carbonaceous layer (N_{L1}) is collectively denoted as N_L; the number of carbon atoms in a disordered layer of the catalyst is denoted as N_B; and the number of carbon atoms in a growing nanotube is denoted as N_T. In the model used here, Puretzky et al. neglect the catalyst deactivation by poisoning, described as N_{L2} [69], and we also choose to consider that the only growth deactivation mechanism is catalyst overcoating with a carbonaceous layer N_{L1} (denoted here as N_L).

The carbon kinetics is given by a system of ordinary differential equations (ODEs):

$$(3.1) \qquad \frac{dN_C}{dt} = \tilde{F}_{c1} n \left(1 - \frac{N_L}{\alpha S_0 n_m} \right) - (k_{sb} + k_{cl}) N_C$$

$$(3.2) \qquad \frac{dN_L}{dt} = \tilde{F}_{c2} n_p \left(1 - \frac{N_L}{\alpha S_0 n_m} \right) + k_{cl} N_C - k_{d1} N_L$$

$$(3.3) \qquad \frac{dN_B}{dt} = k_{sb} N_C - k_t N_B + k_{d1} N_{L1}$$

$$(3.4) \qquad \frac{dN_T}{dt} = k_t N_B$$

$$(3.5) \qquad N_C(0) = N_L(0) = N_B(0) = N_T(0) = 0$$

Here, n is the concentration of feedstock molecules,

n_p is the concentration of gas phase pyrolysis products,

α is the number of monolayers coating the catalyst,

n_m is the surface density of a monolayer of carbon atoms,

S_0 is the surface area of the catalyst,

k_{sb} is the rate constant of dissolution of carbon atoms,

k_{cl} is the rate constant of formation of the carbonaceous layer,

k_{d1} is the dissolution rate constant of the poisoning carbonaceous layer, and

k_t is the rate constant of precipitation of carbon atoms into the nanotube.

The fluxes in Equation (3.1) and Equation (3.2) are given by:

$$(3.6) \qquad \tilde{F}_{c1} = \frac{F_{c1}}{n} \qquad\qquad\qquad \tilde{F}_{c2} = \frac{F_{c2}}{n_p}$$

$$(3.7) \qquad F_{c1} = F_{b1} p_1 \exp \left(-\frac{E_{a1}}{k_B T} \right) \qquad\qquad F_{c2} = F_{b2} p_2 \exp \left(-\frac{E_{a2}}{k_B T} \right)$$

$$(3.8) \qquad F_{b1} = \frac{1}{4} S_0 n \left(\frac{k_B T}{2\pi m} \right)^{1/2} \qquad\qquad F_{b2} = \frac{1}{4} S_0 n \left(\frac{k_B T}{2\pi M} \right)^{1/2}$$

Here, p_1 and p_2 are pre-exponential factors. k_B is Boltzmann's constant and T is the gas temperature. E_{a1} and E_{a2} are the activation barriers for catalytic decomposition and dissolution of the feedstock hydrocarbon, respectively. The masses of the feed-

stock molecule and the main pyrolysis product are denoted m and M, respectively. Values for n, n_p, S_0, T, m, and M were set to match the growth parameters of our experiments. The values selected for the other constants have been previously shown to agree with our experimental results [69, 34]. This system of ODEs is solved using Matlab's ode23s function.

As an example output of the uncoupled CNT growth model, the time evolution of CNT height and growth rate for a 10 nm diameter CNT grown at 1000 K from acetylene (C_2H_2) is shown in Figure 3.2d. The predicted growth rate (CNT height kinetics) reaches its maximum value very quickly, after a brief incubation period, and then gradually decays to zero. Lower activation energy leads to faster growth rate and greater terminal height (CNT length) as shown in Figure 3.3.

Now, to compute the rate of production of active species (source term kinetics shown in Figure 3.2b) on the catalyst surface, we couple it to the kinetics of surface carbon (N_C), which changes with time owing to the evolution of the overcoating layer (N_L). We model the source term f as being proportional to $\tilde{F}_{c1}n\left(1 - \frac{N_L}{\alpha S_0 n_m}\right)$, i.e. the positive term of the rate of change in surface carbon $\frac{dN_C}{dt}$ in (3.1). This source term is now dependent on the available exposed catalytic surface area (i.e. it represents the activity of the catalyst nanoparticle), which describes the kinetics of the generation of active species at the catalyst.

Therefore, the rate of active species generation is calculated for each CNT micropillar separately depending on position on the substrate (x, y) and time t by

$$
(3.9) \qquad f(x, y, t) = \sum_i k_2 F_{c1,i}(t)\left(1 - \frac{N_{L,i}(t)}{\alpha S_0 n_m}\right)\chi_i(x, y)
$$

Here, χ_i represents the indicator function of the i-th catalyst region, i.e. a function with the value one for coordinates in this catalyst region and zero elsewhere. The index i in $F_{c1,i}$ and $N_{L,i}$ specifies that these quantities are associated with the i-th
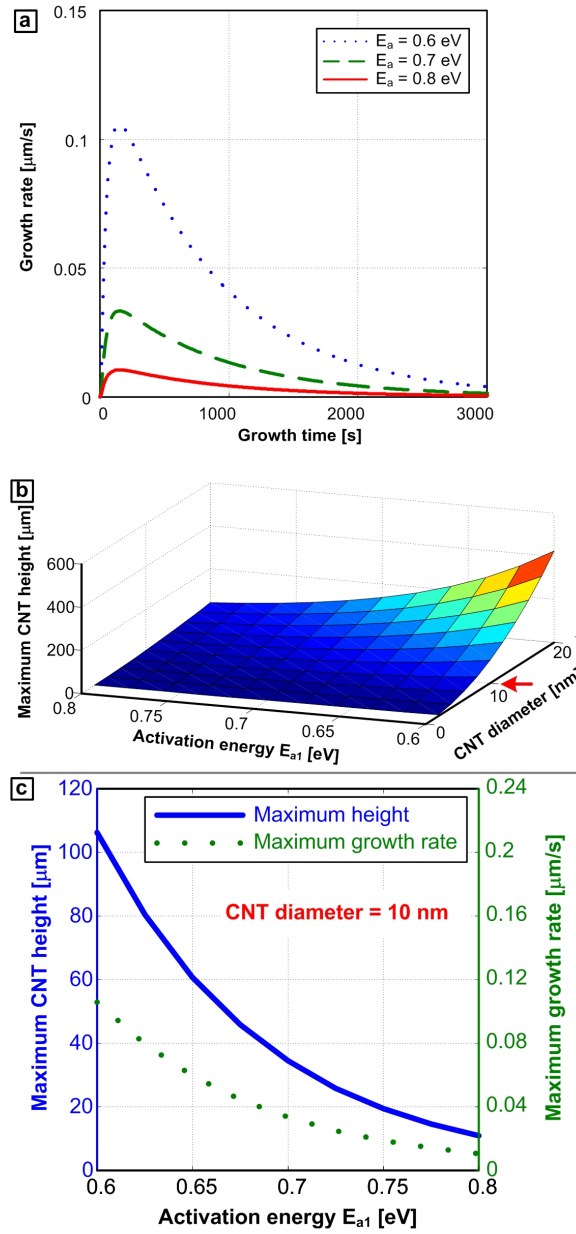
Figure 3.3: (a) The time evolution of growth rate of a 10 nm diameter CNT growing at different activation energies (E_{a1}). (b) Effect of both the CNT diameter and the activation energy (E_{a1}) on the maximum CNT height at self-termination. (c) Effect of activation energy on the maximum CNT height and the maximum growth rate.

catalyst region. The constant k_2 is a scaling factor that is determined empirically by comparing simulations to experimental results. The time-dependent evolution of the source is shown in Figure 3.2e, where the source kinetics at a single micropillar in a catalyst pattern decays to zero at growth termination. This source term is nonzero only at the catalyst regions and is zero elsewhere on the substrate.

Two more important assumptions are made. First, we assume that the distribution of the generated species over each microscale catalyst region is uniform, neglecting the synergetic growth effects among nanoscale catalyst particles within each region. Second, we assume that that the concentration of the active species equals zero at the edge of the simulation space. In reality, the concentration on the boundary is non-zero due to the bulk concentration of precursor in the CVD system. In order to minimize the effect of this boundary condition on our simulation results, we use a domain size of 1×1 mm that is 10-fold larger than the maximum spacing between micro-scale catalyst features in our study (100 μm).

After the active species is produced at a catalyst region, it diffuses through the surrounding area. The concentration of the active species u is given by the diffusion equation, which is a partial differential equation that involves the source term f and the diffusion coefficient D,

(3.10)
$$\frac{\partial}{\partial t} u(x,t) = D \nabla^2 u(x,t) + f(x,t)$$

(3.11)
$$u(x,0) = 0$$

(3.12)
$$u(x,t) = 0 \text{ on the boundary.}$$

We solve the diffusion equation numerically by discretizing the spatial domain into a regular square lattice with step size Δx, and discretizing time into equal time steps Δt. The function u is approximated by the grid function $U_{ij}^n \approx u(i\Delta x, j\Delta x, n\Delta t)$. The Laplacian is discretized with a five-point stencil $\nabla^2_{\Delta x}$, and the equation is evolved

91

using a semi-implicit scheme:

$$(3.13) \qquad U_{ij}^{n+1} = U_{ij}^{n} + (\Delta t)(D\nabla^2_{\Delta x}U_{ij}^{n+1} + f_{ij}^{n}), \text{ or}$$

$$(3.14) \qquad (I - (\Delta t)D\nabla^2_{\Delta x})U_{ij}^{n+1} = U_{ij}^{n} + (\Delta t)f_{ij}^{n}.$$

The system is solved with the conjugate gradient method. At each time step, the source term f is calculated from the concentration N_L, which is found by solving (3.1)-(3.5) on the time interval $[t, t+\Delta t]$ with Matlab's ode23s solver. The step size Δx is chosen small enough that each catalyst region is several grid points wide. We select a time step that balances accuracy and computation time. Moreover, there are no hard constraints on the time step Δt, because the implicit time-stepping scheme is unconditionally stable and the concentration u does not involve any fast dynamics.

The kinetics of the active species concentration is shown to closely follow the source kinetics for the same CNT micropillar (Figure 3.2e). This occurs because the diffusion of the gas is relatively fast in comparison to the time-scale of CNT micropillar growth.

A final important detail of our model is the coupling of active species concentration to the activation energy, which modulates the CNT growth kinetics according to the local concentration of active species. As the concentration of the active species increases, the growth rate of the CNTs also increases, i.e. the activation energy E_{a1} in the Puretzky model decreases. Hence, our model is based on modulating this activation energy E_{a1} by mathematically coupling it to the average concentration $\bar{u}$ of active gaseous species on each catalyst region:

$$(3.15) \qquad \bar{u}_i(t) = \frac{\int u(x,t)\chi_i(x) \, dx}{\int \chi_i(x) \, dx}$$

$$(3.16) \qquad E_{a1,i}(t) = E_{min} - (E_{max} - E_{min})\exp(k_1\bar{u}_i(t)).$$

92

Here, χ_i represents the indicator function of the i-th catalyst region. When the active species concentration is zero, $E_{a1} = E_{max}$; when the concentration is large, E_{a1} approaches the asymptote E_{min}. The constants E_{min}, E_{max} are chosen based on values from the work by Puretzky et al. [69, 34], while the constant k_1 is chosen as the value for which the relative heights of CNTs in the simulations are consistent with those obtained in our experiments. Figure 3.2f shows a plot of the dependence of E_{a1} on u when $E_{max} = 0.8$, $E_{min} = 0.6$, and $k = 0.05$. Equation (3.16) captures the three main features of such dependence. The first feature is the inverse relation between concentration and activation energy. The second feature is having a maximum for activation energy at zero concentration, i.e. in the absence of catalytically produced active species diffusing from the surroundings. In this case, this value of maximum activation energy results from only the active species produced by thermal decomposition of the hydrocarbon feedstock and those that are locally generated at the catalyst location (with no contribution from surroundings). These are dependent on CVD conditions including the precursor chemistry, temperature, and residence time, and are independent on the catalyst microscale pattern. The third feature is the presence of a minimum bound for the activation energy that cannot be surpassed no matter how high the concentration of the active species gets. This is mathematically described as an asymptote of the exponential function. This phenomenological relationship is also consistent with the experimental observations obtained for the dependence of growth rate of nanowires on the spacing, in which experimental results of growth rates exhibited a maximum at small spacing and decayed to an asymptotic minimum [18].

Last, note that the height of the CNT forest is adopted as a quantitative measure of the efficiency of the CVD process. We assume that all CNTs within a forest (micropillar) are identical and are mechanically coupled, and therefore collectively grow at the same rate [13]. As a result, the model only predicts the straight vertical

growth of each micropillar. The spatial variations of CNT growth rate within each micropillar and the resulting deformation during growth (e.g. Figure 3.1a) are topics of ongoing research in our group, and modeling coupled mechanochemical effects is beyond the scope of the present work.

3.2.2 Experimental

Catalyst patterning: Micron-scale patterning of the catalyst film was achieved by photolithography on a (100) silicon wafer with a 300 nm thermally grown SiO_2 layer. After spin-coating the photoresist (SPR220), a patterned mask was used during contact exposure of UV light (Karl Suss MA/BA-6) at 30 mJ/s for 6 seconds. After development of the patterned photoresist, the supported catalyst (1 nm Fe on 10 nm Al_2O_3) was deposited by sputtering (Lab 18 by Kurt J. Lesker). The wafer was diced manually by a diamond-tip scribe. The remaining photoresist was then lifted off the wafer by placing samples in an ultrasonic bath of acetone, before loading the catalyst-coated Si chips into the tube furnace.

CNT growth and characterization: CNTs were grown in a custom-built hot-wall tube furnace, with a rapid sample insertion mechanism. First, the substrate was annealed to induce catalyst film dewetting and nanoparticle formation in a reducing atmosphere of hydrogen and helium (400 sccm H_2 / 100 sccm He) at 775 °C (10 minutes ramp time and 10 minutes temperature hold). After the annealing step, the substrate was retracted from the reactor and held in an adjacent cold chamber, while introducing the feedstock gas, ethylene (C_2H_4), changing the gas mixture to the growth atmosphere (100 sccm C_2H_4 / 400 sccm He / 100 sccm H_2) at the same temperature. After 7 minutes, during which the gases and the humidity inside the tube furnace stabilize, the substrate was returned to inside the reactor. CNTs were characterized by scanning electron microscopy (SEM), using a Philips XL30FEG.

3.3 Results

The comprehensive growth model described above provides a framework to simulate the influence of chemical coupling on CNT growth, and can be correlated with experimental results, which in turn inform the model and enable validation of improved growth conditions. In the subsections that follow, we show that the chemically coupled model predicts spatial non-uniformities in CNT growth rate among micropillar arrays (Figure 3.5 and Figure 3.6). We also show that the "digital" change in CNT growth from tangled horizontal mat to vertically aligned forest can be explained based on a threshold concentration of active species (Figure 3.6 and Figure 3.7). Moreover, we exploit the insights gained by our simulation and experimental results to design more uniform individual CNT micropillars (Figure 3.8), as well as more uniform micropillar arrays (Figure 3.9).

3.3.1 Diffusion-driven concentration profiles

First, we use the model to visualize and understand how the diffusion of the active species (gas) depends on the CVD conditions and the pattern design. The diffusion coefficient (D) in Equation 10 depends on temperature, pressure and the gases according to an empirical relation [39]:

$$(3.17) \qquad D = (2.6280 \times 10^{-3}) \frac{\sqrt{\frac{T^3(M_1+M_2)}{2M_1M_2}}}{p\sigma_{12}^2}$$

$$(3.18) \qquad \sigma_{12} = \frac{1}{2}(\sigma_1 + \sigma_2),$$

where M_i is the molecular weight of species i in grams per mole, T is the temperature in Kelvin, p is the pressure in atmospheres, and σ_i is the molecular diameter of species i in Å. For example, the diffusion coefficient of C_2H_4 in He at 1 atm was calculated to be 1 cm^2/s at 600 K and 2 cm^2/s at 1000 K. We first show the effect of process

temperature on gas diffusion and the resulting spatial distribution of active species concentration. Concentration profiles are plotted in Figure 3.4 after 750 seconds of growth at two different temperatures of 600 and 1000 K, which correspond to the values of diffusion coefficient of 1 and 2 cm^2/s, respectively. As shown in this figure, the maximum concentration occurs at the center micropillar in a hexagonal array, because at this location the maximum number of micropillars contributes to the overall concentration of active species. Higher pressures and lower temperatures significantly reduce gas diffusion to the surroundings, resulting in a much higher local concentration of active species. Also, for patterns with larger spacing (δ), the local maxima in the concentration profile are sharper, in contrast to the smooth concentration profiles observed for closely packed catalyst microfeatures.

3.3.2 Predicting spatially varying CNT growth kinetics

Now, we show that the spatial distribution of active species governs the growth kinetics of CNT micropillars in arrays, predicting the observed dependence of CNT growth rate and terminal height. A 3D plot of the normalized terminal height of an exemplary CNT micropillar array (Figure 3.5a) shows that the array has a domed shape with taller micropillars toward the center and shorter micropillars at the edges. Without chemical coupling, all pillars in the array would be predicted to grow to the same height. In Figure 3.5b the height kinetics of the central micropillar and the corner micropillar are shown, revealing that the final height of the corner micropillar is about 60% of the final height of the central micropillar. This height difference is present because the spatial variation of active species modulates the activation energy (Figure 3.5c) for the CNT growth process, by the formulation discussed previously.

The kinetics of the active species generation at the central micropillar are shown in Figure 3.5d, and the kinetics of active species concentration are shown in Figure 3.5e. After a rapid increase, the production rate decreases almost linearly and then decays
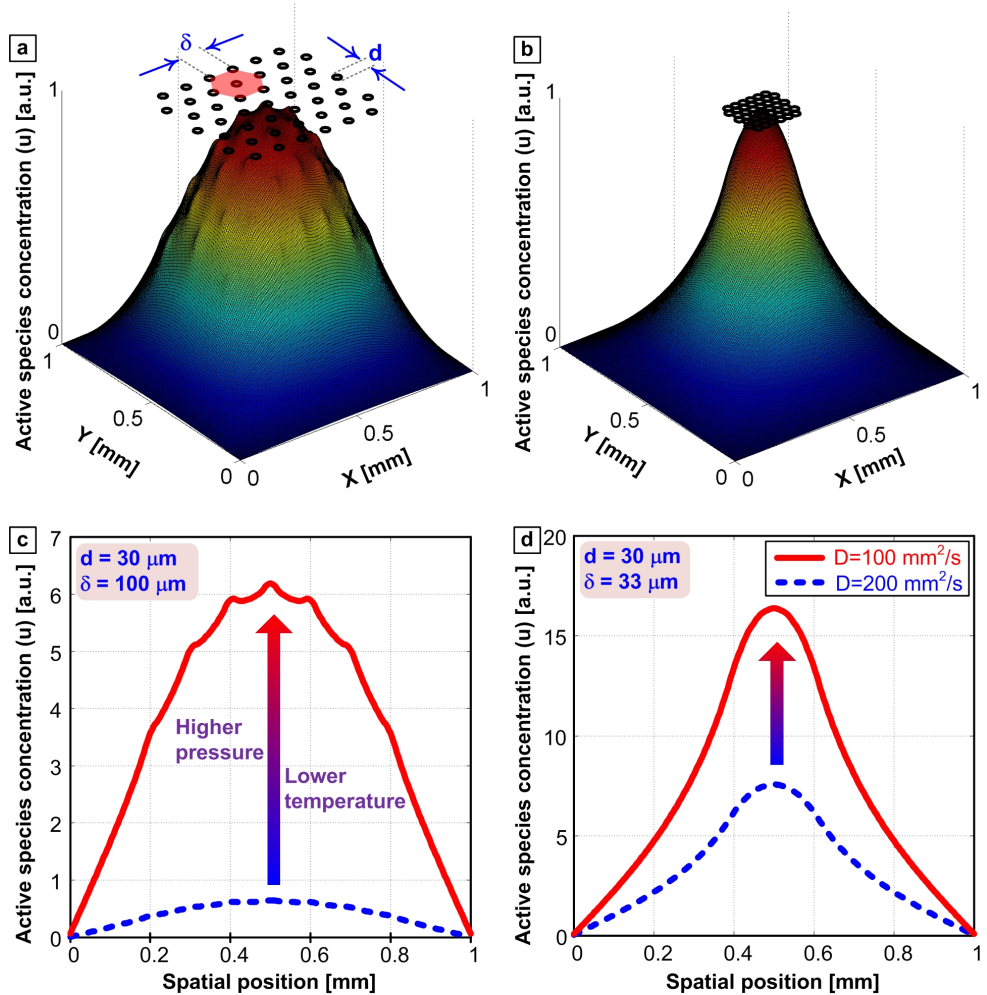
Figure 3.4: Influence of model parameters on the spatial distribution of active species generated within and around a CNT growth pattern. (a,b) 3D surface plot of concentration profile of active species generated at micron-scale catalyst patches ($d = 30 \ \mu$m) that are arranged in a hexagonal array with different spacing (δ) of 100 μm and 33 μm, respectively (diffusion coefficient $D = 100$ mm^2/s). (c,d) The 2D spatial distribution of active species concentration (u) for the same two catalyst arrays, plotted after 750 s of growth for two different temperatures of 600 and 1000 K, which correspond to diffusion coefficients of 100 mm^2/s and 200 mm^2/s, respectively. The spatial step size is $\Delta x = 0.004$ mm and the time step is $\Delta t = 7.5$ s.
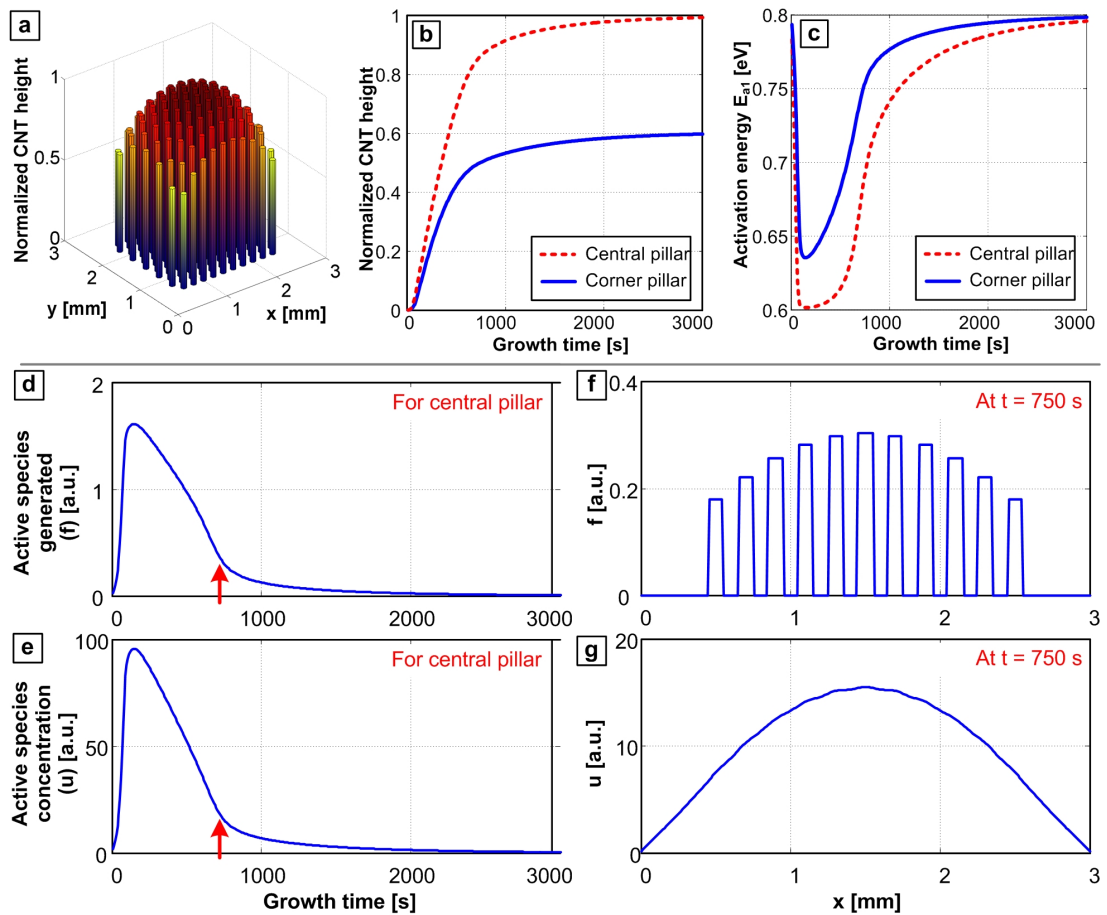
Figure 3.5: Simulation results for a hexagonal array of CNT micropillars $d = 100$ μm and $\delta = 200$ μm center-to-center spacing. The spatial step size is $\Delta x = 0.012$ mm and the time step is $\Delta t = 7.5$ s. (a) 3D plot of the spatial distribution of normalized micropillar heights. (b) Height kinetics for the central micropillar and a corner micropillar. (c) Time evolution of activation energy (E_{a1}). (d, e) Time evolution of the active species generation (source term) and the ensuing concentration for the same central micropillar. (f, g) Spatial distribution of the active species generation term (source term) and the concentration distribution after 750 seconds of growth (at $y = 1.5$ mm).

exponentially to zero. The spatial profiles of the active species generation and the ensuing concentration at t = 750 s are shown in Figure 3.5f, g. The growth rate is typically lower at the edge of the pattern because the higher activation energy there causes carbon to decompose at a lower rate and therefore the active species are produced at a lower rate (Figure 3.5g). Shallow peaks in active species concentration are observed at the catalyst site locations, where the gas is consumed by CNT growth. The maximum concentration occurs at the center of the array, and the concentration decays to zero at the endpoints, representing the boundary of the simulation space.

We now compare simulations to experiments to understand the synergetic growth effects within an array of CNT micropillars. SEM images (Figure 3.6a-c) show that the height and uniformity of 30 μm diameter CNT micropillars decreases as the spacing between the catalyst microfeatures increases. Specifically, for small spacing (center-to-center distance of 33 μm), all CNT micropillars in the array grow vertically upward. In the case of large spacing (100 μm), none of the catalyst features produce a sufficient density of CNTs to lift off and grow vertically. For the array with medium spacing (60 μm), only the CNT micropillars towards the center of the array grow vertically, while features towards the edges/corners of the array do not grow vertically. This consistent observation can be explained by the spatial variation of concentration-modulated growth that gives rise to the height variation shown in Figure 3.5. However, to this point, the model does not explain the abrupt transition between features that do not grow vertically, and those that produce vertical CNT forests.

3.3.3 Predicting a chemical threshold for CNT forest growth

The catalyst microfeatures that do not grow vertically aligned CNTs exhibit a lower density of tangled CNTs (inset in Figure 3.6c). Previous work, using X-ray scattering to profile the density of CNTs within a forest grown to termination, showed that a threshold CNT density is needed to create and maintain the vertically aligned
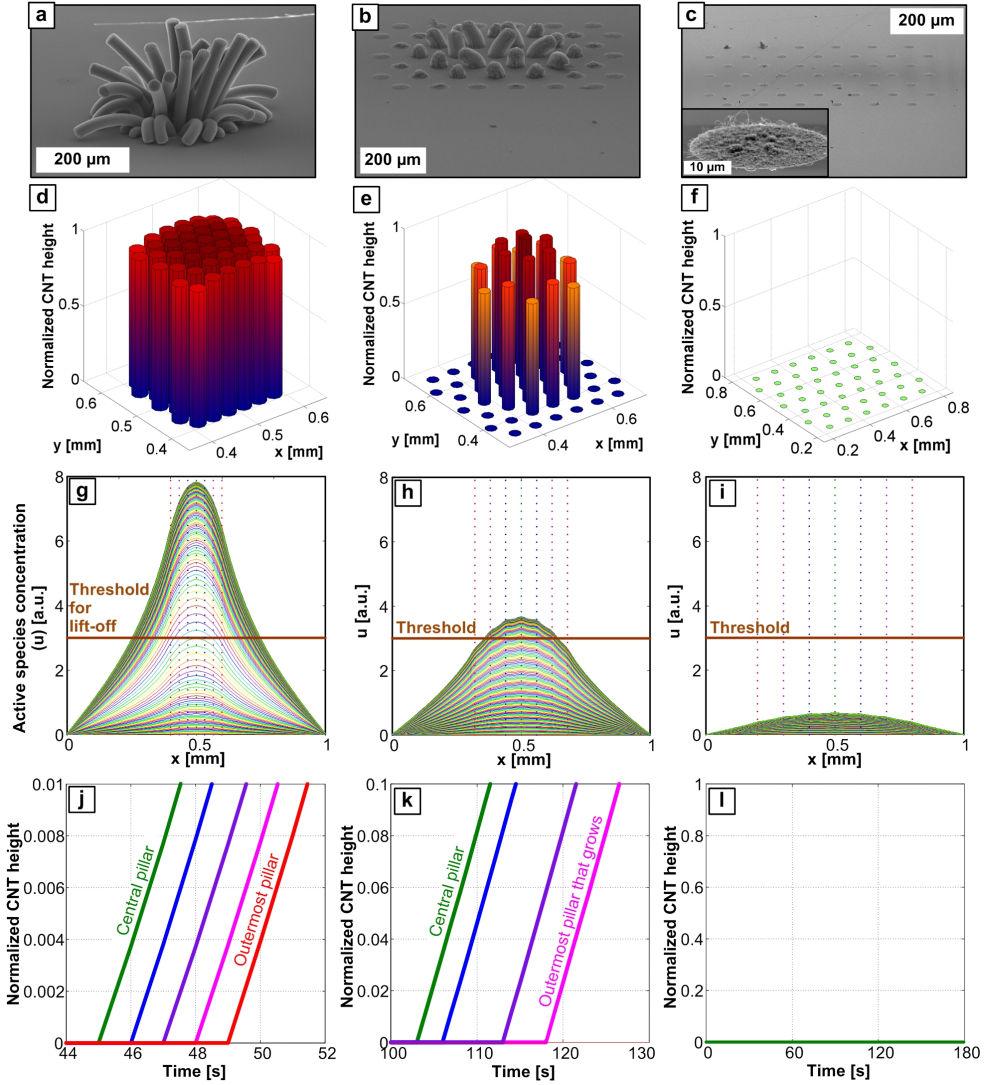
Figure 3.6: Effect of micropillar spacing in arrays on lift-off and growth. SEM images of CNT micropillar arrays having center-to-center pillar spacing of 33 μm, 60 μm, and 100 μm are shown in (a, b, c), respectively. The inset to (c) shows a tangled mat of CNTs in cases when the micropillars do not lift off into a forest. Simulation results showing relative heights for these different CNT spacings are plotted in (d, e, f). The spatial step size is $\Delta x = 0.004$ mm and the time step is $\Delta t = 1.0$ s. Time evolution of the spatial distribution of active species concentration for different spacings is plotted in (g, h, i), identifying the threshold for lift-off. A plot of the initial CNT forest height kinetics for each spacing is plotted in (j, k, l), showing the delayed onset of lift-off for outer micropillars compared to central micropillar. The position of the threshold relative to the active species concentration indicates whether or not the CNT micropillar has lifted off into a forest; specifically, the model of the array in (a) predicts accurately that all the CNT pillars lift off, and the model of (c) predicts that the active species never crosses the threshold due to the larger spacing and reduced chemical coupling.

100

forest structure [16, 15]. This threshold density was also predicted by finite element modeling of the CNT crowding mechanics [14]. Therefore, we hypothesize that the time varying (increasing) concentration of active species that results from diffusion across the substrate drives the kinetics of CNT density increase and eventual forest lift-off. We explain the transition between tangled and vertical CNTs (Figure 3.6d-f) by a threshold concentration of active species (Figure 3.6g-i) that is necessary to cause the CNT density to surpass the threshold for self-organization into the vertically aligned forest morphology. Although some CNTs can start growing into a randomly oriented mat as soon as the hydrocarbon feedstock is introduced into the reactor (see inset in Figure 3.6i), vertical growth of the forest is delayed until the threshold concentration is reached, as shown in Figure 3.6j-l. The value of this threshold was chosen to match the experimentally obtained micropillar height distribution, and it would in principle depend on the overall area of the catalyst microfeatures and CVD conditions.

Close-up electron micrographs of the CNT micropillar array with medium spacing (Figure 3.7a) shows that the geometry of each micropillar is non-uniform as well, i.e. the top surface of the micropillar can be curved and the pillar has a varying cross-sectional area from top to bottom. This non-uniformity, which is a typical indication of low-density CNT micropillars, can be attributed to density profiles across the height of each micropillar [16, 14, 65]. Although these density variations are not captured by our mathematical model, the introduction of the chemical threshold, shown in Figure 3.6g, h, i, adequately predicts the transition from horizontal randomly oriented growth of CNT mats to the vertical self-supported aligned growth of CNT forest morphology.

We can also infer the successive stages of vertical micropillar growth by examining micropillars at varying stages of growth based on their spatial position in the array. Figure 3.7b shows a schematic of the successive stages that are needed for
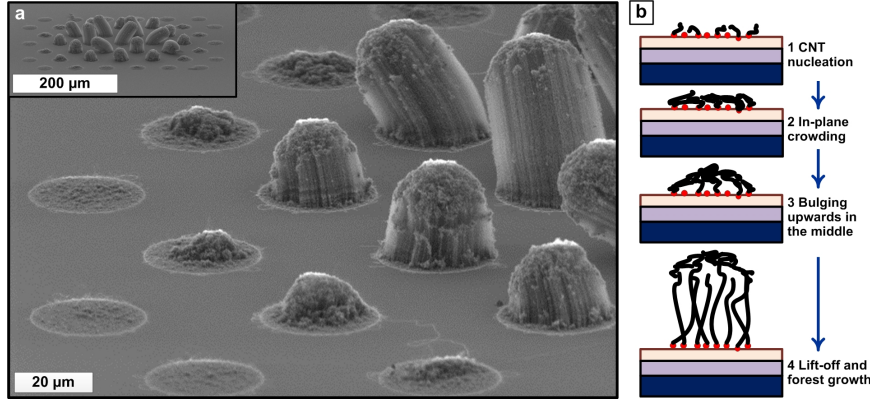
Figure 3.7: Analysis of the CNT growth gradient at the edge of a micropillar array, and identification of successive stages of micropillar lift-off due to collective chemical and mechanical effects. (a) SEM of the medium spacing array (with 60 μm spacing), showing that micropillars are at different stages of lift-off depending on their position in the array. (b) Schematic showing the progression of stages leading to CNT micropillar lift-off.

CNT micropillar lift-off. First, CNT nucleation starts as soon as the hydrocarbon gas feedstock is introduced to the reactor, yet at this stage CNTs grow in random orientations, forming a tangled 2D mat. This crowding stage proceeds until the density of growing CNTs reaches a threshold value, which has been previously identified to be about 109 CNTs/cm^2 for CNTs grown by the same CVD recipe [16, 14]. This threshold density represents the density at which the total upward force overcomes the van der Waals attraction forces pulling the CNTs to the substrate.

Although our mathematical model considers that the rate of active species generation is constant across each micron-sized catalyst area (Figure 3.2b), there are likely local rate variations due to the chemical coupling between individual catalyst nanoparticles within the catalyst area. Hence, we expect that the CNT activation kinetics is fastest towards the middle of the catalyst area for each micropillar. As a result, the threshold density is reached in the middle of the micropillar area first, and lift-off starts to develop from the center of the micropillar, until eventually, the whole micropillar lifts off. This delay between the lift-off of the middle portion of the mi-

cropillar and the lift-off of the whole micropillar results in a dome-shaped top surface. For instance, a more curved top is an indication of slow kinetics of CNT activation as the active species propagates through the micropillar. Our model does not describe the curvature of the top-surface of the pillar, because the height kinetics is assumed to be similar for all CNTs within each micropillar. Nevertheless, the explanation above, which can be mathematically modeled in the future, provides insights into the kinetics of CNT self-organization that are necessary to establish vertical growth.

3.3.4 Design of uniform CNT micropillars

The capability to predict CNT growth patterns can also enable engineering of process conditions and pattern geometries to achieve improved uniformity. One way to achieve geometric uniformity for individual catalyst microfeatures that typically don't grow into tall, straight micropillars, is to add a border of CNTs around the feature. Figure 3.8 shows the effect of having a surrounding border of CNTs around a 30×30 μm square micropillar. For a small spacing of 100 μm between the central micropillar and the border, the resulting central micropillar is straighter than in the case of the larger spacing (300 μm). Also, geometry of the top surface of the micropillar is more uniform and square in the case of the smaller spacing, compared to a more curved top in the case of the larger spacing. This is attributed to the faster kinetics of CNT activation that result from the higher concentration of active species in the case of smaller spacing (Figure 3.8b), owing to the external supply (from the border) of active species to the otherwise isolated micropillar. This finding is consistent with a recent study, in which an outer surrounding border was shown to improve the straightness and alignment of CNT microstructures grown for microelectromechanical systems (MEMS) applications [59].

Additionally, applying the insights from our simulations and experiments, CNT micropillar uniformity can be engineered by designing the array patterns. Tailoring

103
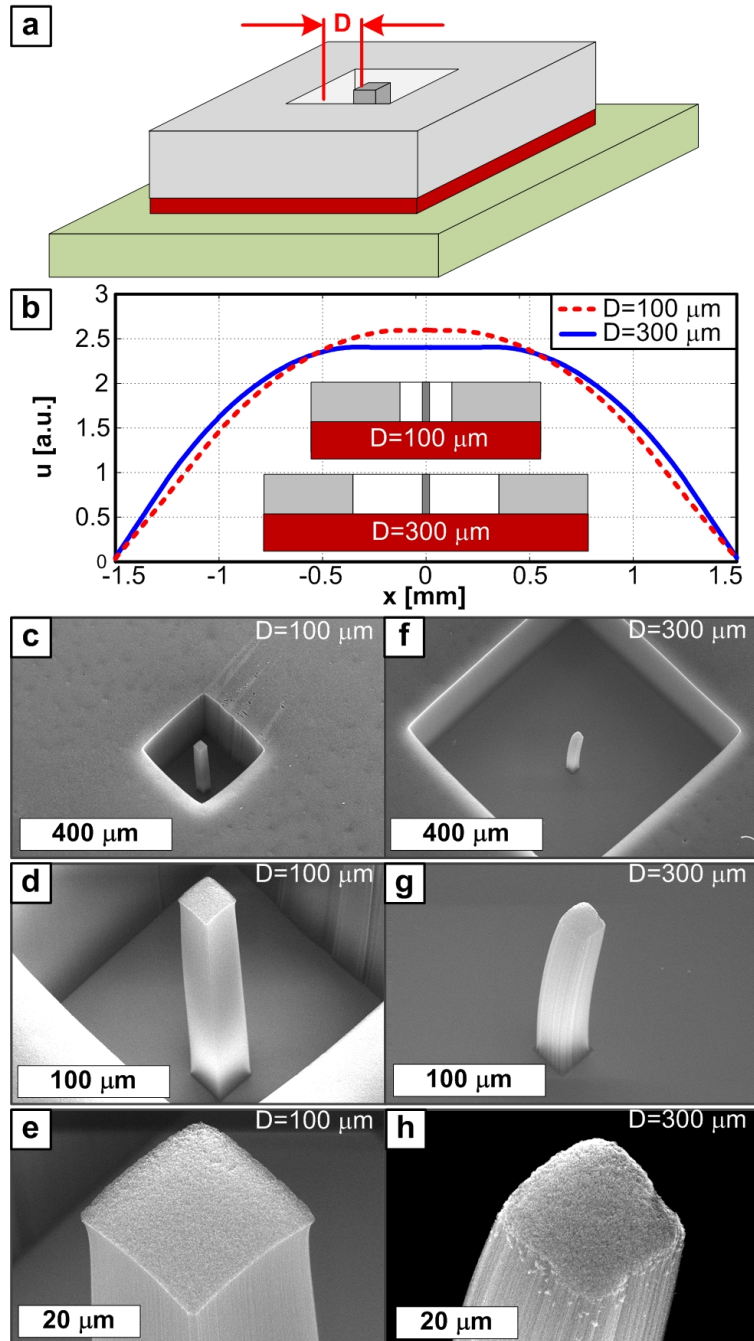
Figure 3.8: Realization of isolated straight CNT micropillars (30×30 μm) using a border feature to augment the active species concentration. (a) Schematic of design. Note that D denotes the spacing between the pillar and border, not the diffusion coefficient. (b) Concentration profile of active species showing two cases with different spacing D (100 and 300 μm). The spatial step size is $\Delta x = 0.012$ mm and the time step is $\Delta t = 7.5$ s. SEM images at different magnifications for the 100 μm spacing (c-e) and the 300 μm spacing (f-h).

the spacing between micropillars and/or the size of individual micropillars results in a more uniform distribution of active species concentration, which in turn improves the uniformity of CNT micropillar height. Figure 3.9 shows strategies that can greatly enhance the height uniformity. The first strategy (Figure 3.9b, e) features a spatially varying spacing, where the distance between micropillars is largest in the middle of the array and smallest at the periphery of the array. This strategy is helpful for those applications that require similar diameter micropillars without the requirement that the positions of micropillars are equally spaced. The second strategy (Figure 3.9c, f) relies on changing the cross-sectional dimensions (area) of the micropillars across the array, wherein pillars towards the center of the pattern are smallest and micropillars towards the periphery of the pattern are largest. This strategy is suitable for applications in which the position, or the center-line, of each micropillar is pre-specified by the device design, such as in the case of growing CNT micropillars to connect circuits having multiple layers. In both strategies, the concentration profile becomes more uniform, as compared to the case of a uniformly spaced same-sized micropillar array.

For the second strategy the total catalyst area is increased, which results in an increase in the magnitude of the produced active species and is, therefore, likely to be accompanied by an increase in CNT activation rate and density. Simulation results show that the ratio between the shortest (outermost) micropillar and the tallest (central) micropillar has increased from 86% in the case of uniformly spaced same-sized micropillars to 92% by applying the first strategy (varying the spacing only) and to 93% by applying the second strategy (varying the micropillar size only). Hence, employing a combination of similar strategies in pattern design will both homogenize the typically nonuniform concentration profile of active species, and boost the density activation kinetics of CNT micropillars.

105
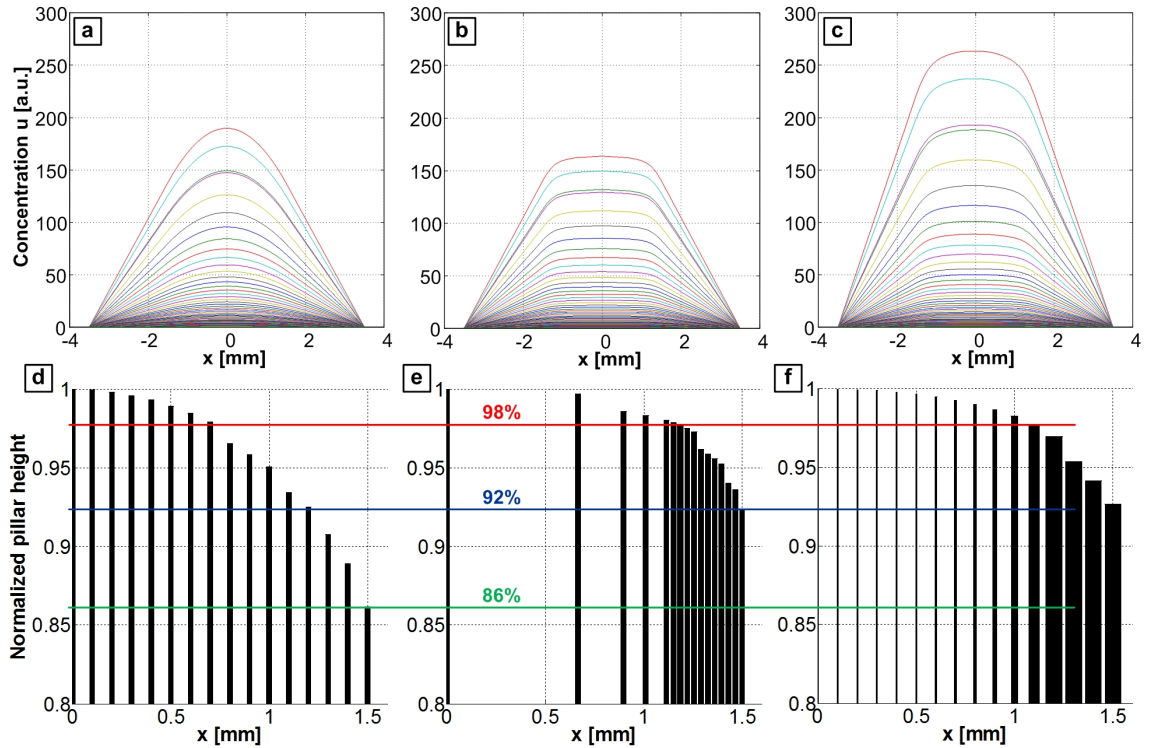
Figure 3.9: Predicted design of CNT micropillar arrays to achieve increased height uniformity in the presence of chemical coupling. Evolution of the spatial distribution of active species concentration is shown for (a) uniformly spaced (60 μm spacing) micropillars having the same width (30 μm), (b) non-uniformly spaced micropillars having the same width (30 μm), and (c) uniformly spaced micropillars having varying widths. Relative height distribution for only right-side half of the micropillar array for (a), (b), and (c) are shown in (d), (e), and (f) respectively. The spatial step size is $\Delta x = 0.004$ mm and the time step is $\Delta t = 7.5$ s.

3.4 Discussion

Prior work in the literature has shown that CNT growth can be limited by gas diffusion of precursor [94, 95]. Our framework considers the dynamics of gas diffusion of hydrocarbon species generated at the catalyst sites, which results in a time-evolving concentration profile. Although we consider that the rate-limiting process in CNT growth is gas diffusion, we formulate the effect of the ensuing concentration profile on the catalytic decomposition of hydrocarbons at the catalyst. Our modeling framework consolidates into a single metric the various gaseous species that modulate the reaction activation energy of hydrocarbon dissociation on the surface of catalyst nanoparticles (E_{a1}). Previous work has shown that CNT growth could be limited by the diffusion of carbon atoms into/on the catalyst nanoparticle [86], which would require coupling the activation energy for dissolution (part of the equation for the rate k_{sb}) to concentration, but this effect is ignored in the present work.

The concentration of an individual hydrocarbon precursor should not change the activation energy for chemical decomposition on the catalyst surface (E_{a1}). However, there is a preponderance of evidence that a family of hydrocarbon gases and radicals contribute to CNT growth by thermal CVD, and these have varying potency in promoting CNT growth. As the concentration and distribution of these precursors change due to thermal and catalytic decomposition of the input feedstock, the collective activation barrier for chemical decomposition is shifted in the vicinity of the catalyst surface. Our model collectively approximates this effect by modulating the value of E_{a1} based on the concentration of generated active species (u).

Further research is required to enable a mathematical description of the relative proportions of each of these species, and designed experiments are needed to investigate their isolated, as well as cooperative, effects on modulating growth, as well as on activating CNT growth during the nucleation stage. In addition, the effects of other additives such as oxygen [92], hydrogen [92], water vapor [38], and carbon diox-

ide [53, 60] on mediating CVD growth of CNTs, should be taken into consideration. Other gaseous species have an opposite effect on growth, and some species might play either an activating or deactivating role depending on their partial pressure, total pressure, temperature, and/or gas composition in the reactor. These "harmful" effects on growth should also be modeled, in order to describe the growth process more accurately. This activation/deactivation competition is not solely controlled by the byproducts of local catalytic reaction or even gas-phase reaction in the vicinity of the catalyst particle, but are also affected by the desorption of various species from the reactor wall [52].

Despite such complexities and the assumptions of this study, we can make important quantitative insights regarding the influence of process parameters, such as temperature and pressure, on synergetic CNT growth. For instance, CNT growth at lower temperature and higher pressure increases the influence of chemical coupling, because sharper chemical gradients result from lower diffusion coefficients (Figure 3.4). On the other hand, high temperature growth in low-pressure conditions should reduce synergetic growth effects due to the high diffusion coefficient and mean free path. Temperature variation would also affect the reaction kinetics, and that pressure variation would also influence the gas residence time, which is known to influence CNT growth independently of synergetic effects. Therefore, the mathematical framework for modeling chemical feedback on CNT growth will enable exploration of improved uniformity in future work.

3.5   Conclusions

We enable prediction and control of non-uniformities in as-grown CNT micropillars by developing a holistic mathematical model that couples isolated CNT growth with diffusion of reactive species across the substrate. This model replicates experimental findings where the overall height and uniformity of CNT micropillars is

influenced only by the spacing between catalyst microfeatures on the substrate. Combining experiments and simulations reveals that a threshold concentration of active species is needed for lift-off of CNT micropillars and corroborates analysis of the successive stages of CNT micropillar growth. Our findings also enable the design and fabrication of uniform micropillar arrays, which are essential for the scaled manufacturing of commercial CNT-based devices with enhanced electrical, thermal, and mass transport properties. An example of utility is presented via designs predicting a more uniform distribution of micropillar heights, or designed height gradients. In the future, this approach could also serve as a basis for optimization algorithms for pattern design considering both chemical reaction models and synergetic coupling effects, with relevance to CNTs as well as other nanostructures by CVD reactions.

CHAPTER IV

Conclusion

4.1   Summary of findings

In this dissertation, we defined an atomistic model for the growth of individual CNTs. We found that simulations of the model exhibit partial growth of a CNT, but the system gets stuck in local energy minima that made it difficult for the nanotube to grow upward. Long annealing times should allow for the system to reach a global energy minimum and continue growing, but this is very computationally demanding. Instead, we considered an atomistic model of a simpler system that could provide some insights into CNT growth. In this system, which has a global energy minima and many local energy minima with identical higher energy, the probability of the globally minimal configuration is increased by lowering the temperature. In non-equilibrium, the probability of this state can be increased by slowing the addition rate. This suggests higher quality CNTs can be grown at lower temperatures and slower addition rates. Since MD simulations of CNT growth require fast addition rates in order to complete in a reasonable amount of time, this also explains why these simulations get stuck in local minima that are not the ground state.

We also coupled a kinetic model of CNT growth with a model of active species concentration to describe the growth of arrays of CNT pillars. This incorporates spatial effects into the growth model, whereas the kinetic model only includes temporal

effects. The active species concentration is greater where the density of the catalyst patches is higher at the center of the pattern, which leads to faster growth rates for the pillars in the center of the array. A threshold on the active species concentration is used to determine when pillars lift off from the substrate. Simulations of this model show qualitative agreement with experiments. The model could inform the design of catalyst patterns which yield pillars with uniform heights. The catalyst patches would be spaced more widely at the center of the array, and more closely together at the edge of the array. Alternatively, a uniform spacing could be used with smaller patches at the center and larger patches at the edge.

4.2 Future research

The development, simulation, and analysis of the models described in this dissertation open up many directions for future research.

4.2.1 Atomistic modeling

For the 1-dimensional model, one could simulate the dynamics by a Monte Carlo method and compare its efficiency with molecular dynamics. This could inform the simulation method for the 3-dimensional model. Reconsidering the 3-dimensional model (or a 2-dimensional analogue) would be interesting because the formation and healing of defects could be studied. It would be very interesting to characterize the transition rates for these processes and study them in a non-equilibrium system, as was done for the 1-dimensional model.

Applied mechanical forces could be included in an atomistic model of CNT growth, in any dimension. This can be accomplished by selecting a collection of atoms at the tip of the atomic chain or nanotube on which the force is exerted and addding a linear term to the potential for these atoms. This term should be chosen so that the negative gradient points in the direction of the applied force. The magnitude and direction of

this force can be varied and the resulting growth studied. If the local energy minima and saddle points can be located, then one can calculate the transition rates and evolve the probabilities of the different configurations. If this is not possible, one can simulate multiple trajectories by molecular dynamics and calculate the probabilities empirically. In particular, it would be interesting to study the effect of the magnitude and direction of the applied force on the probability of the ground state and the rate of convergence to the equilibrium probability distribution.

4.2.2   Chemical coupling

The chemical coupling model could include gas transport in 3 dimensions, including advection and the effect of the CNT pillars on diffusion. Multiple chemical species and coupled reactions could be included, which could accelerate or decelerate CNT growth. The chemical coupling model could be extended to describe the mechanical and chemical coupling within the pillar, which would lead to pillar bending. The chemical coupling model could be used to optimize uniformity of the heights in the pillars. This could be done with optimization techniques rather than trial and error. For instance, one could devise an objective function which achieves a minimum for uniform pillar heights. The variation of the energy could be calculated with respect to perturbations in the characteristic function of the catalyst pattern. This variation could be employed in a gradient descent technique for the energy.

It would be beneficial to identify the active species. This could be done by comparing experiments to simulations of multiple models corresponding to the hypothesized active species, and determining which active species provide the best fit for the data. Based on the chemistry, once could then relate the rate of production of the active species relative to the feedstock decomposition, which we treated as a free parameter.

Atomistic modeling could provide insights into the chemical coupling model. For example, the chirality-dependent growth rate could be incorporated into the kinetic

equations. Also, the relationship between the active species concentration and the activation energy for feedstock decomposition could be studied via an atomistic model instead of an *ad hoc* way as in our model.

BIBLIOGRAPHY

BIBLIOGRAPHY

[1] K. O. Abrokwah, P. R. Chidambaram, and D. S. Boning. Pattern based prediction for plasma etch. *Semiconductor Manufacturing, IEEE Transactions on*, 20(2):77–86, May 2007.

[2] H. Amara, C. Bichara, and F. Ducastelle. Formation of carbon nanostructures on nickel surfaces: A tight-binding grand canonical Monte Carlo study. *Phys. Rev. B*, 73:113404, Mar 2006.

[3] H. Amara, C. Bichara, and F. Ducastelle. A tight-binding grand canonical Monte Carlo study of the catalytic growth of carbon nanotubes. *Journal of Nanoscience and Nanotechnology*, 8(11):6099–6104, 2008.

[4] H. Amara, C. Bichara, and F. Ducastelle. Understanding the nucleation mechanisms of carbon nanotubes in catalytic chemical vapor deposition. *Phys. Rev. Lett.*, 100:056105, Feb 2008.

[5] A. N. Andriotis and M. Menon. Self-consistent tight-binding molecular-dynamics method for cluster studies. *Phys. Rev. B*, 59:15942–15949, Jun 1999.

[6] A. N. Andriotis, M. Menon, and G. Froudakis. Catalytic action of Ni atoms in the formation of carbon nanotubes: A molecular dynamics study. *Phys. Rev. Lett.*, 85:3193–3196, Oct 2000.

[7] V. I. Artyukhov, Y. Liu, and B. I. Yakobson. Equilibrium at the edge and atomistic mechanisms of graphene growth. *Proceedings of the National Academy of Sciences*, 109(38):15136–15140, 2012.

[8] V. I. Artyukhov, E. S. Penev, and B. I. Yakobson. Why nanotubes grow chiral. *Nat. Commun.*, 5, Sep 2014.

[9] R. T. K. Baker. Catalytic growth of carbon filaments. *Carbon*, 27(3):315–323, 1989.

[10] P. B. Balbuena, J. Zhao, S. Huang, Y. Wang, N. Sakulchaicharoen, and D. E. Resasco. Role of the catalyst in the growth of single-wall carbon nanotubes. *Journal of Nanoscience and Nanotechnology*, 6(5):1247–1258, 2006.

[11] M. Bedewy. *Collective mechanochemical growth of carbon nanotubes*. PhD thesis, University of Michigan, Ann Arbor, 2014.

[12] M. Bedewy, B. Farmer, and A. J. Hart. Synergetic chemical coupling controls the uniformity of carbon nanotube microstructure growth. *ACS Nano*, 8(6):5799–5812, 2014.

[13] M. Bedewy and A. J. Hart. Mechanical coupling limits the density and quality of self-organized carbon nanotube growth. *Nanoscale*, 5:2928–2937, 2013.

[14] M. Bedewy, E. R. Meshot, H. Guo, E. A. Verploegen, W. Lu, and A. J. Hart. Collective mechanism for the evolution and self-termination of vertically aligned carbon nanotube growth. *The Journal of Physical Chemistry C*, 113(48):20576–20582, 2009.

[15] M. Bedewy, E. R. Meshot, and A. J. Hart. Diameter-dependent kinetics of activation and deactivation in carbon nanotube population growth. *Carbon*, 50(14):5106–5116, 2012.

[16] M. Bedewy, E. R. Meshot, M. J. Reinker, and A. J. Hart. Population growth dynamics of carbon nanotubes. *ACS Nano*, 5(11):8974–8989, 2011.

[17] S. Berber, Y.-K. Kwon, and D. Tománek. Unusually high thermal conductivity of carbon nanotubes. *Phys. Rev. Lett.*, 84:4613–4616, May 2000.

[18] M. T. Borgström, G. Immink, B. Ketelaars, R. Algra, and E. P. A. M. Bakkers. Synergetic nanowire growth. *Nature Nanotechnology*, 2:541–544, 2007.

[19] C. J. Brabec, A. Maiti, C. Roland, and J. Bernholc. Growth of carbon nanotubes: a molecular dynamics study. *Chemical Physics Letters*, 236(1–2):150–155, 1995.

[20] D. W. Brenner. Empirical potential for hydrocarbons for use in simulating the chemical vapor deposition of diamond films. *Phys. Rev. B*, 42:9458–9471, Nov 1990.

[21] D. W. Brenner, O. A Shenderova, J. A. Harrison, S. J. Stuart, B. Ni, and S. B. Sinnott. A second-generation reactive empirical bond order (REBO) potential energy expression for hydrocarbons. *Journal of Physics: Condensed Matter*, 14(4):783, 2002.

[22] M. J. Bronikowski. CVD growth of carbon nanotube bundle arrays. *Carbon*, 44(13):2822–2832, 2006.

[23] A. Brünger, C. L. Brooks III, and M. Karplus. Stochastic boundary conditions for molecular dynamics simulations of ST2 water. *Chemical Physics Letters*, 105(5):495 – 500, 1984.

[24] J.-C. Charlier, A. De Vita, X. Blase, and R. Car. Microscopic growth mechanisms for carbon nanotubes. *Science*, 275(5300):647–649, 1997.

[25] M. F. L. De Volder, S. H. Tawfick, R. H. Baughman, and A. J. Hart. Carbon nanotubes: Present and future commercial applications. *Science*, 339(6119):535–539, 2013.

[26] M. Diarra, H. Amara, F. Ducastelle, and C. Bichara. Carbon solubility in nickel nanoparticles: A grand canonical Monte Carlo study. *Physica Status Solidi (b)*, 249(12):2629–2634, 2012.

[27] F. Ding, K. Bolton, and A. Rosén. Nucleation and growth of single-walled carbon nanotubes: A molecular dynamics study. *The Journal of Physical Chemistry B*, 108(45):17369–17377, 2004.

[28] F. Ding, A. R. Harutyunyan, and B. I. Yakobson. Dislocation theory of chirality-controlled nanotube growth. *Proceedings of the National Academy of Sciences*, 106(8):2506–2509, 2009.

[29] F. Ding, P. Larsson, J. A. Larsson, R. Ahuja, H. Duan, A. Rosén, and K. Bolton. The importance of strong carbon-metal adhesion for catalytic nucleation of single-walled carbon nanotubes. *Nano Letters*, 8(2):463–468, 2008.

[30] M. S. Dresselhaus, G. Dresselhaus, and Ph. Avouris. *Carbon Nanotubes: Synthesis, Structure, Properties, and Applications*. Topics in applied physics. Springer, 2001.

[31] J. A. Elliott, Y. Shibuta, H. Amara, C. Bichara, and E. C. Neyts. Atomistic modelling of CVD synthesis of carbon nanotubes and graphene. *Nanoscale*, 5:6662–6676, 2013.

[32] G. Eres, A. A. Kinkhabwala, H. Cui, D. B. Geohegan, A. A. Puretzky, and D. H. Lowndes. Molecular beam-controlled nucleation and growth of vertically aligned single-wall carbon nanotube arrays. *The Journal of Physical Chemistry B*, 109(35):16684–16694, 2005.

[33] J. Gavillet, A. Loiseau, C. Journet, F. Willaime, F. Ducastelle, and J.-C. Charlier. Root-growth mechanism for single-wall carbon nanotubes. *Phys. Rev. Lett.*, 87:275504, Dec 2001.

[34] D. B. Geohegan, A. A. Puretzky, J. J. Jackson, C. M. Rouleau, G. Eres, and K. L. More. Flux-dependent growth kinetics and diameter selectivity in single-wall carbon nanotube arrays. *ACS Nano*, 5(10):8311–8321, 2011.

[35] G. H. Golub and C. F. Van Loan. *Matrix Computations*. Johns Hopkins Studies in the Mathematical Sciences. Johns Hopkins University Press, 2012.

[36] J.-H. Han, R. A. Graff, B. Welch, C. P. Marsh, R. Franks, and M. S. Strano. A mechanochemical model of growth termination in vertical carbon nanotube forests. *ACS Nano*, 2(1):53–60, 2008.

[37] P. Hänggi, P. Talkner, and M. Borkovec. Reaction-rate theory: fifty years after Kramers. *Rev. Mod. Phys.*, 62:251–341, Apr 1990.

[38] K. Hata, D. N. Futaba, K. Mizuno, T. Namai, M. Yumura, and S. Iijima. Water-assisted highly efficient synthesis of impurity-free single-walled carbon nanotubes. *Science*, 306(5700):1362–1364, 2004.

[39] J. O. Hirschfelder, C. F. Curtiss, and R. B. Bird. *Molecular theory of gases and liquids*. Structure of matter series. Wiley, 1964.

[40] S. Hofmann, R. Sharma, C. Ducati, G. Du, C. Mattevi, C. Cepek, M. Cantoro, S. Pisana, A. Parvez, F. Cervantes-Sodi, A. C. Ferrari, R. Dunin-Borkowski, S. Lizzit, L. Petaccia, A. Goldoni, and J. Robertson. In situ observations of catalyst dynamics during surface-bound carbon nanotube nucleation. *Nano Letters*, 7(3):602–608, 2007.

[41] S. B. Hutchens, L. J. Hall, and J. R. Greer. In situ mechanical testing reveals periodic buckle nucleation and propagation in carbon nanotube bundles. *Advanced Functional Materials*, 20(14):2338–2346, 2010.

[42] S. Irle, Y. Ohta, Y. Okamoto, A. J. Page, Y. Wang, and K. Morokuma. Milestones in molecular dynamics simulations of single-walled carbon nanotube formation: A brief critical review. *Nano Research*, 2(10):755–767, 2009.

[43] G.-H. Jeong, N. Olofsson, L. K. L. Falk, and E. E. B. Campbell. Effect of catalyst pattern geometry on the growth of vertically aligned carbon nanotube arrays. *Carbon*, 47(3):696–704, 2009.

[44] K. Jiang, C. Feng, K. Liu, and S. Fan. A vapor-liquid-solid model for chemical vapor deposition growth of carbon nanotubes. *Journal of Nanoscience and Nanotechnology*, 7(4-1):1494–1504, 2007-04-01T00:00:00.

[45] H. Kimura, J. Goto, S. Yasuda, S. Sakurai, M. Yumura, D. N. Futaba, and K. Hata. Unexpectedly high yield carbon nanotube synthesis from low-activity carbon feedstocks at high concentrations. *ACS Nano*, 7(4):3150–3157, 2013.

[46] N. Latorre, E. Romeo, F. Cazaña, T. Ubieto, C. Royo, J. I. Villacampa, and A. Monzón. Carbon nanotube growth by catalytic chemical vapor deposition: A phenomenological kinetic model. *The Journal of Physical Chemistry C*, 114(11):4773–4782, 2010.

[47] Y. H. Lee, S. G. Kim, and D. Tománek. Catalytic growth of single-wall carbon nanotubes: An *ab initio* study. *Phys. Rev. Lett.*, 78:2393–2396, Mar 1997.

[48] T. Lelièvre, G. Stoltz, and M. Rousset. *Free Energy Computations: A Mathematical Perspective*. Imperial College Press, 2010.

[49] H.-B. Li, A. J. Page, S. Irle, and K. Morokuma. Single-walled carbon nanotube growth from chiral carbon nanorings: Prediction of chirality and diameter influence on growth rates. *Journal of the American Chemical Society*, 134(38):15887–15896, 2012.

[50] B. Liu, J. Liu, X. Tu, J. Zhang, M. Zheng, and C. Zhou. Chirality-dependent vapor-phase epitaxial growth and termination of single-wall carbon nanotubes. *Nano Letters*, 13(9):4416–4421, 2013.

[51] J. Liu, C. Wang, X. Tu, B. Liu, L. Chen, M. Zheng, and C. Zhou. Chirality-controlled synthesis of single-wall carbon nanotubes using vapour-phase epitaxy. *Nat. Commun.*, 3:1199, 2012.

[52] K. Liu, P. Liu, K. Jiang, and S. Fan. Effect of carbon deposits on the reactor wall during the growth of multi-walled carbon nanotube arrays. *Carbon*, 45(12):2379–2387, 2007.

[53] A. Magrez, J. W. Seo, V. L. Kuznetsov, and L. Forró. Evidence of an equimolar C2H2–CO2 reaction in the synthesis of carbon nanotubes. *Angewandte Chemie International Edition*, 46(3):441–444, 2007.

[54] A. Magrez, R. Smajda, J. W. Seo, E. Horváth, P. R. Ribič, J. C. Andresen, D. Acquaviva, A. Olariu, G. Laurenczy, and L. Forró. Striking influence of the catalyst support and its acid-base properties: New insight into the growth mechanism of carbon nanotubes. *ACS Nano*, 5(5):3428–3437, 2011.

[55] A. Maiti, C. J. Brabec, C. M. Roland, and J. Bernholc. Growth energetics of carbon nanotubes. *Phys. Rev. Lett.*, 73:2468–2471, Oct 1994.

[56] M. R. Maschmann, G. J. Ehlert, S. J. Park, D. Mollenhauer, B. Maruyama, A. J. Hart, and J. W. Baur. Visualizing strain evolution and coordinated buckling within CNT arrays by in situ digital image correlation. *Advanced Functional Materials*, 22(22):4686–4695, 2012.

[57] E. R. Meshot, D. L. Plata, S. Tawfick, Y. Zhang, E. A. Verploegen, and A. J. Hart. Engineering vertically aligned carbon nanotube growth by decoupled thermal treatment of precursor and catalyst. *ACS Nano*, 3(9):2477–2486, 2009.

[58] M. Moseler, F. Cervantes-Sodi, S. Hofmann, G. Csányi, and A. C. Ferrari. Dynamic catalyst restructuring during carbon nanotube growth. *ACS Nano*, 4(12):7587–7595, 2010.

[59] K. Moulton, N. B. Morrill, A. M. Konneker, B. D. Jensen, R. R. Vanfleet, D. D. Allred, and R. C. Davis. Effect of iron catalyst thickness on vertically aligned carbon nanotube forest straightness for CNT-MEMS. *Journal of Micromechanics and Microengineering*, 22(5):055004, 2012.

[60] A. G. Nasibulin, D. P. Brown, P. Queipo, D. Gonzalez, H. Jiang, and E. I. Kauppinen. An essential role of CO2 and H2O during single-walled CNT synthesis from carbon monoxide. *Chemical Physics Letters*, 417(1–3):179–184, 2006.

[61] G. D. Nessim, M. Seita, D. L. Plata, K. P. O'Brien, A. J. Hart, E. R. Meshot, C. M. Reddy, P. M. Gschwend, and C. V. Thompson. Precursor gas chemistry

determines the crystallinity of carbon nanotubes synthesized at low temperature. *Carbon*, 49(3):804–810, 2011.

[62] E. C. Neyts, Y. Shibuta, A. C. T. van Duin, and A. Bogaerts. Catalyzed growth of carbon nanotube with definable chirality by hybrid molecular dynamics–force biased Monte Carlo simulations. *ACS Nano*, 4(11):6665–6672, 2010.

[63] J. R. Norris. *Markov chains.* Cambridge series in statistical and probabilistic mathematics. Cambridge University Press, 1997.

[64] A. J. Page, Y. Ohta, S. Irle, and K. Morokuma. Mechanisms of single-walled carbon nanotube nucleation, growth, and healing determined using QM/MD methods. *Accounts of Chemical Research*, 43(10):1375–1385, 2010.

[65] S. J. Park, A. J. Schmidt, M. Bedewy, and A. J. Hart. Measurement of carbon nanotube microstructure relative density by optical attenuation and observation of size-dependent variations. *Phys. Chem. Chem. Phys.*, 15:11511–11519, 2013.

[66] J. M. Parker and H.-S. P. Wong. Synergetic carbon nanotube growth. *Carbon*, 62:61–68, 2013.

[67] D. L. Plata, A. J. Hart, C. M. Reddy, and P. M. Gschwend. Early evaluation of potential environmental impacts of carbon nanotube synthesis by chemical vapor deposition. *Environmental Science & Technology*, 43(21):8367–8373, 2009.

[68] D. L. Plata, E. R. Meshot, C. M. Reddy, A. J. Hart, and P. M. Gschwend. Multiple alkynes react with ethylene to enhance carbon nanotube synthesis, suggesting a polymerization-like formation mechanism. *ACS Nano*, 4(12):7185–7192, 2010.

[69] A. A. Puretzky, D. B. Geohegan, S. Jesse, I. N. Ivanov, and G. Eres. In situ measurements and modeling of carbon nanotube array growth kinetics during chemical vapor deposition. *Applied Physics A: Materials Science & Processing*, 81:223–240, 2005.

[70] R. Rao, D. Liptak, T. Cherukuri, B. I. Yakobson, and B. Maruyama. In situ evidence for chirality-dependent growth rates of individual carbon nanotubes. *Nature Materials*, 11:213–216, 2012.

[71] J.-Y. Raty, F. Gygi, and G. Galli. Growth of carbon nanotubes on metal nanoparticles: A microscopic mechanism from *ab initio* molecular dynamics simulations. *Phys. Rev. Lett.*, 95:096103, Aug 2005.

[72] D. Schebarchov, S. C. Hendy, E. Ertekin, and J. C. Grossman. Interplay of wetting and elasticity in the nucleation of carbon nanotubes. *Phys. Rev. Lett.*, 107:185503, Oct 2011.

[73] Y. Shibuta and S. Maruyama. Molecular dynamics simulation of formation process of single-walled carbon nanotubes by CCVD method. *Chemical Physics Letters*, 382(3–4):381–386, 2003.

[74] Y. Shibuta and S. Maruyama. A molecular dynamics study of the effect of a substrate on catalytic metal clusters in nucleation process of single-walled carbon nanotubes. *Chemical Physics Letters*, 437(4–6):218–223, 2007.

[75] B. E. Stine, D. O. Ouma, R. R. Divecha, D. S. Boning, J. E. Chung, D. L. Hetherington, C. R. Harwoo, O. S. Nakagawa, and S.-Y. Oh. Rapid characterization and modeling of pattern-dependent variation in chemical-mechanical polishing. *Semiconductor Manufacturing, IEEE Transactions on*, 11(1):129–140, Feb 1998.

[76] F. A. Tal and E. Vanden-Eijnden. Transition state theory and dynamical corrections in ergodic systems. *Nonlinearity*, 19(2):501, 2006.

[77] S. Tawfick, K. O'Brien, and A. J. Hart. Flexible high-conductivity carbon-nanotube interconnects made by rolling and printing. *Small*, 5(21):2467–2473, 2009.

[78] A. Thess, R. Lee, P. Nikolaev, H. Dai, P. Petit, J. Robert, C. Xu, Y. H. Lee, S. G. Kim, A. G. Rinzler, D. T. Colbert, G. E. Scuseria, D. Tománek, J. E. Fischer, and R. E. Smalley. Crystalline ropes of metallic carbon nanotubes. *Science*, 273(5274):483–487, 1996.

[79] G. G. Tibbetts. Why are carbon filaments tubular? *Journal of Crystal Growth*, 66(3):632–638, 1984.

[80] E. Vanden-Eijnden and F. A. Tal. Transition state theory: Variational formulation, dynamical corrections, and error estimates. *The Journal of Chemical Physics*, 123(18), 2005.

[81] P. Vinten, J. Bond, P. Marshall, J. Lefebvre, and P. Finnie. Origin of periodic rippling during chemical vapor deposition growth of carbon nanotube forests. *Carbon*, 49(15):4972–4981, 2011.

[82] M. F. L. De Volder, D. O. Vidaud, E. R. Meshot, S. Tawfick, and A. J. Hart. Self-similar organization of arrays of individual carbon nanotubes and carbon nanotube micropillars. *Microelectronic Engineering*, 87(5–8):1233–1238, 2010. The 35th International Conference on Micro- and Nano-Engineering (MNE).

[83] R. S. Wagner and W. C. Ellis. Vapor-liquid-solid mechanism of single crystal growth. *Applied Physics Letters*, 4(5):89–90, 1964.

[84] B. Q. Wei, R. Vajtai, and P. M. Ajayan. Reliability and current carrying capacity of carbon nanotubes. *Applied Physics Letters*, 79(8):1172–1174, 2001.

[85] C. T. Wirth, B. C. Bayer, A. D. Gamalski, S. Esconjauregui, R. S. Weatherup, C. Ducati, C. Baehtz, J. Robertson, and S. Hofmann. The phase of iron catalyst nanoparticles during carbon nanotube growth. *Chemistry of Materials*, 24(24):4633–4640, 2012.

[86] C. T. Wirth, C. Zhang, G. Zhong, S. Hofmann, and J. Robertson. Diffusion- and reaction-limited growth of carbon nanotube forests. *ACS Nano*, 3(11):3560–3566, 2009.

[87] Y. Yamaguchi and S. Maruyama. A molecular dynamics simulation of the fullerene formation process. *Chemical Physics Letters*, 286(3–4):336–342, 1998.

[88] Y. Yamaguchi and S. Maruyama. A molecular dynamics study on the formation of metallofullerene. *The European Physical Journal D - Atomic, Molecular, Optical and Plasma Physics*, 9(1):385–388, 1999.

[89] G. Yuan, A. M. Marconnet, X. Rong, S. Maruyama, and K. E. Goodson. Heat capacity, thermal conductivity, and interface resistance extraction for single-walled carbon nanotube films using frequency-domain thermoreflectance. *Components, Packaging and Manufacturing Technology, IEEE Transactions on*, 3(9):1524–1532, Sept 2013.

[90] Q. Yuan, H. Hu, and F. Ding. Threshold barrier of carbon nanotube growth. *Phys. Rev. Lett.*, 107:156101, Oct 2011.

[91] Q. Yuan, Z. Xu, B. I. Yakobson, and F. Ding. Efficient defect healing in catalytic carbon nanotube growth. *Phys. Rev. Lett.*, 108:245505, Jun 2012.

[92] G. Zhang, D. Mann, L. Zhang, A. Javey, Y. Li, E. Yenilmez, Q. Wang, J. P. McVittie, Y. Nishi, J. Gibbons, and H. Dai. Ultra-high-yield growth of vertical single-walled carbon nanotubes: Hidden roles of hydrogen and oxygen. *Proceedings of the National Academy of Sciences of the United States of America*, 102(45):16141–16145, 2005.

[93] J. Zhao, A. Martinez-Limia, and P. B. Balbuena. Understanding catalysed growth of single-wall carbon nanotubes. *Nanotechnology*, 16(7):S575, 2005.

[94] G. Zhong, T. Iwasaki, J. Robertson, and H. Kawarada. Growth kinetics of 0.5 cm vertically aligned single-walled carbon nanotubes. *The Journal of Physical Chemistry B*, 111(8):1907–1910, 2007.

[95] L. Zhu, D. W. Hess, and C.-P. Wong. Monitoring carbon nanotube growth by formation of nanotube stacks and investigation of the diffusion-controlled kinetics. *The Journal of Physical Chemistry B*, 110(11):5445–5449, 2006.